FACULDADE DE ENGENHARIA DA UNIVERSIDADE DO PORTO

Development of a Test Rig for Digital Twin Applications: Wear Evaluation Using Vibration Analysis

Ricardo Varo Leal Salústio



Mestrado em Engenharia Mecânica

Supervisor: Prof. Dr. Pedro José da Silva Carvalho Pereira de Sousa

INEGI Supervisor: Eng. Alexandre Brás dos Santos

September 30, 2026

© Ricardo Salústio, 2026

Development of a Test Rig for Digital Twin Applications: Wear Evaluation Using Vibration Analysis

Ricardo Varo Leal Salústio

Mestrado em Engenharia Mecânica

Approved in oral examination by the committee:

President: Prof. Dr. Mário Vaz
Examiner: Prof. Dr. Hernâni Lopes
Member: Prof. Dr. Pedro Sousa

September 30, 2026

Resumo

A manutenção preditiva e as arquiteturas de Gémeo Digital dependem de dados de degradação que, em serviço, são dispendiosos de obter: o desgaste desenvolve-se ao longo de meses, as condições de funcionamento não podem ser manipuladas e o estado real de um órgão muitas vezes não é inspecionável sem paragem. A presente dissertação desenvolve um demonstrador compacto e de baixo custo, no qual o desgaste de um par de engrenagens de dentado reto possa ser induzido em condições controladas e acompanhado por via vibratória, bem como a respetiva cadeia de aquisição e processamento de sinal, baseada em reamostragem angular, média síncrona no tempo e em indicadores de condição nos domínios do tempo e da frequência.

A aplicação de carga não foi possível com o conjunto motor–travão disponível, pelo que a campanha experimental foi orientada para a caracterização da cadeia de medição e do comportamento do demonstrador, não sendo expectável, na ausência de carga, o desenvolvimento de desgaste mensurável no par de engrenagens. A cadeia de medição foi, avaliada: apesar do caminho de transmissão em polímero, a frequência de engrenamento é resolvida com harmónicos até à sexta ordem e a velocidade do veio medida concorda com o valor cinemático com um erro de 0,4 %. Duas anomalias no funcionamento, a passagem de partículas pelo engrenamento e a iniciação por fadiga da fenda no acoplamento, foram detetados pelo pico de aceleração máximo e pela curtose do sinal bruto, e localizados pela comparação entre os dois acelerómetros. O demonstrador demonstra assim algumas limitações da utilização de suportes poliméricos impressos em 3D para suporte de veios de transmissão e da utilização de travões de fricção acionados por mola como elementos de carga contínua.

Palavras-chave: monitorização de condição • desgaste de engrenagens • análise de vibrações • indicadores de condição • bancada de ensaios

Abstract

Predictive maintenance and Digital Twin frameworks depend on degradation data that is expensive to obtain in service: wear develops over months, operating conditions cannot be manipulated, and the true condition of a component often cannot be inspected without downtime. This dissertation develops a compact, low-cost demonstrator in which the wear of a spur gear pair can be induced under controlled conditions and followed through vibration, together with the corresponding acquisition and signal processing chain, based on angular resampling, time synchronous averaging (TSA) and condition indicators in the time and frequency domains.

The application of load was not possible with the available motor–brake assembly, so the experimental campaign was directed towards the characterisation of the measurement chain and of the demonstrator's behaviour, since no measurable wear of the gear pair is to be expected in the absence of load. The measurement chain was evaluated: despite the polymer transmission path, the meshing frequency is resolved with harmonics up to the sixth order, and the measured shaft speed agrees with the kinematic value with an error of 0.4 %. Two anomalous events, the passage of debris through the mesh and the fatigue initiation of the crack in the motor coupling, were detected by the maximum peak acceleration and the raw kurtosis, and localised by the comparison between the two accelerometers. The demonstrator therefore highlights the limitations of 3D-printed polymer supports for transmission shafts and of spring-applied friction brakes as continuous loading elements.

Keywords: condition monitoring • gear wear • vibration analysis • condition indicators • test rig

The United Nations Sustainable Development Goals

The United Nations Sustainable Development Goalss (SDGs) provide a global framework for achieving a better and more sustainable future for all. It includes 17 goals to address the world's most pressing challenges, including poverty, inequality, climate change, environmental degradation, peace, and justice. This dissertation, which focuses on the development of a test rig and of vibration-based indicators for the wear monitoring of gear transmissions, contributes to targets related to industrial modernization, responsible use of resources, and technical education.

SDG 9 Build resilient infrastructure, promote inclusive and sustainable industrialization and foster innovation.

SDG 12 Ensure sustainable consumption and production patterns.

SDG 4 Ensure inclusive and equitable quality education and promote lifelong learning opportunities for all.

SDG	Target	Contribution	Performance Indicators and Metrics
9	9.4	Vibration-based condition monitoring modernizes existing industrial drivetrains, allowing maintenance to be decided from the measured state of the machine and keeping transmissions operating near their design efficiency.	Reduction of unplanned downtime; number of transmissions covered by condition monitoring.
12	12.5	Replacing components on condition rather than on schedule extends the service life extracted from each one and prevents the secondary damage of an unanticipated failure, so fewer serviceable parts are discarded.	Fraction of useful life consumed at replacement; serviceable components spared per avoided failure.
4	4.4	The demonstrator is portable and low-powered, which makes it usable as a platform for teaching condition monitoring and for demonstrating it to industrial partners.	Training sessions and demonstrations supported by the rig; students and trainees involved in its use.

Agradecimentos

Existe um provérbio africano que diz que "Para educar uma criança é preciso uma aldeia". O trabalho aqui apresentado não teria sido possível de realizar sem muito trabalho individual, mas também sem a ajuda de uma grande quantidade de pessoas que me acompanharam antes, durante e certamente depois deste período, às quais quero deixar um especial agradecimento

Em primeiro lugar ao Prof. Pedro Sousa, ao Eng. Alexandre Santos e a toda a gente na UMAI, por me acompanharem e acolherem com paciência todas as minhas dúvidas nesta jornada e pelo ambiente de colaboração e camaradagem que me proporcionaram durante estes meses.

Agradeço depois à minha família, por desde cedo serem uma base inabalável para o meu crescimento em todos os campos da vida, alimentarem a minha procura pelo conhecimento e por serem uma representação daquilo que de facto é uma casa. Deixo também um agradecimento às minhas segundas famílias em Esgueira, a minha "terrinha": o Clã 25 Aristides de Sousa Mendes e os "Machos em Mirandela", que não sendo família de sangue foram origem de muitas memórias e ensinamentos durante estes 5 anos e durante toda a minha vida.

Tive também muita gente que me apoiou nesta minha "casa fora de casa" que é a Faculdade de Engenharia da Universidade do Porto. Agradeço à Tuna de Engenharia da Universidade do Porto que, pela Praxe, Música e Amizade, me ajudou a viver de uma maneira de qualquer outra forma inalcançável a boémia de ser estudante. Deixo também uma enorme palavra de apreço aos Patos, que me proporcionaram as melhores memórias destes anos e com quem ganhei na verdade o orgulho de pertencer a esta casa.

Por fim deixo um agradecimento à Beatriz Rebelo, a minha namorada, por ser um apoio verdadeiramente incondicional, por acreditar em mim em todos os momentos e pela ajuda a levantar a cabeça mesmo nos dias mais difíceis.

A toda esta minha aldeia. Um enorme e sincero obrigado.

Ricardo Salústio

Declaração de Honra

Declaro que a presente dissertação é de minha autoria e não foi previamente apresentada e avaliada nesta ou em outra instituição. As referências a outros autores (afirmações, ideias, pensamentos), assim como a utilização de trabalhos publicados respeitam escrupulosamente as regras da atribuição, e encontram-se devidamente indicadas no texto e nas referências bibliográficas, de acordo corn as normas de referenciação. Tenho consciência de que a prática de plágio ou de autoplágio constituem ilícitos académicos, conforme estabelecido no Código de Ética da U.Porto.

Declaro, ainda, que utilizei ferramentas de Inteligência Artificial para a realização de parte(s) da presente dissertação, e essa utilização e os seus resultados estão devidamente assinalados e foram objeto de cuidada verificação para deteção de erros, imprecisões, atribuições infundadas ou outras formas de enviesamento de conteúdos e argumentos, bem como de determinação de autoria.

Ricardo Varo Leal Salústio



"O sucesso tem uma estranha capaciadde de esconder o erro."

Gaius Salustius Crispus

Contents

1 Introduction **1**
- 1.1 Motivation . . . 1
- 1.2 Objectives . . . 2
- 1.3 Structure of the Dissertation . . . 3

2 Literature Review **4**
- 2.1 Wear . . . 4
  - 2.1.1 Definition and terminology . . . 4
  - 2.1.2 Case Studies in the Literature . . . 5
  - 2.1.3 Selected Configuration . . . 8
  - 2.1.4 Wear in the Context of Gears . . . 8
- 2.2 Effect of Wear on Gear Dynamics. . . . 10
  - 2.2.1 Healthy Gear Vibration Signature . . . 10
  - 2.2.2 Uniform Wear . . . 12
  - 2.2.3 Localized Wear . . . 13
  - 2.2.4 Shaft Related Wear . . . 14
  - 2.2.5 Bearings . . . 15
  - 2.2.6 Pulleys . . . 17
- 2.3 Dynamic Models of Gear Systems . . . 17
  - 2.3.1 The Wear Dynamics Feedback Loop . . . 17
  - 2.3.2 Tribological Wear Modelling (Archard's Law) . . . 19
  - 2.3.3 Tooth Crack Propagation . . . 20
- 2.4 Condition Indicators . . . 22
  - 2.4.1 Time-Domain Indicators . . . 23
  - 2.4.2 Frequency-Domain Indicators . . . 25
  - 2.4.3 Time–Frequency Domain Indicators . . . 27
- 2.5 Machine Learning Applications . . . 29
  - 2.5.1 Learning from Extracted Features . . . 29
  - 2.5.2 Learning from the Signal . . . 29
  - 2.5.3 Limitations and Relation to the Present Work . . . 30

3 Demonstrator Design **31**
- 3.1 Design Requirements . . . 31
- 3.2 Driving unit . . . 32
- 3.3 Loading elements . . . 33
  - 3.3.1 Gear Pump System . . . 33
  - 3.3.2 Eddy Current Brakes . . . 35
  - 3.3.3 Friction Brakes . . . 37

3.3.4 Selection . . . 39
3.4 Gear Pair . . . 40
3.5 Drive train . . . 41
3.5.1 Reduction stages . . . 41
3.5.2 Shafts . . . 42
3.6 Structural components . . . 52
3.6.1 Rig Frame: Aluminium Profiles . . . 52
3.6.2 Rotational Support: Rolling Element Bearings . . . 52
3.6.3 Custom Interfaces: 3D Printed Supports . . . 52
3.7 Completed Design . . . 54

4 Computational Implementation **55**
4.1 Wear evaluation . . . 55
4.2 Instrumentation . . . 55
4.3 Data flow and signal processing . . . 57
4.3.1 Signal Treatment . . . 57
4.3.2 CIs Calculation . . . 59

5 Demonstrator Assembly **60**
5.1 Test Rig Limitations . . . 60
5.2 Modifications . . . 61
5.3 Modified Test Rig Behaviour . . . 62

6 Results and Discussion **64**
6.1 Experimental Conditions . . . 64
6.2 Campaign Overview and Outcome . . . 68
6.3 Condition of the Gear Pair . . . 69
6.4 Events Observed During the Campaign . . . 71
6.4.1 Noise emission and impulsive events . . . 71
6.4.2 Failure of the motor coupling . . . 72
6.5 CIs over the Campaign . . . 72
6.5.1 Indicators computed on the raw signal . . . 76
6.5.2 Indicators computed on the TSA signal . . . 78
6.5.3 Frequency-domain indicators . . . 81

7 Conclusions and Future Work **83**
7.1 The Demonstrator . . . 83
7.2 Wear Evaluation . . . 84
7.3 Distance to a DT . . . 85
7.4 Future Work . . . 86

References **88**

List of Figures

2.1 Various severities of gear tooth surface wear, similar to as depicted in ISO-108251-1.[21] . . . 11
2.2 Frequency spectrum of a synthesized healthy gear meshing signal. . . . 12
2.3 Typical spectrum changes due to uniform wear. . . . 13
2.4 Frequency spectrum of a localized gear fault, characterized by wide, high-amplitude, unsymmetrical sideband families around the meshing harmonics. . . . 14
2.5 Synthesized raw and envelope spectra of a rolling element bearing with an outer race defect. . . . 16
2.6 Examples of dynamic models developed for spur gear system analysis. . . . 18
2.7 Diagram of the feedback loop used in spur gear lumped-parameter dynamic models. 19

3.1 Hydraulic circuit of the loading element. The gear pump absorbs the braking torque T_{brake}, and the load is set by the adjustable throttle, across which the pressure drop ΔP is measured. . . . 34
3.2 Sketch of rotor-stator interaction in an ECB. [50] . . . 36
3.3 Magnetic flux field in the ECB assembly, simulated in FEMM. . . . 38
3.4 Typical wear pattern in friction disc surface's [53]. . . . 39
3.5 Layout of the demonstrator and operating conditions along the power train. . . . 41
3.6 Forces acting on the driving pulley. . . . 43
3.7 Shaft geometry (relief grooves not represented) with the applied loads and the corresponding bending moment diagram. . . . 45
3.8 Influence coefficient δ_{ii} along the shaft. . . . 49
3.9 Discretisation of the shaft into 36 equal segments of $\Delta x = 2$ mm. . . . 50
3.10 Additively manufactured supports used in the demonstrator. . . . 53
3.11 3D assembly of the demonstrator, designed in Solidworks. . . . 54

4.1 Demonstrator tachometer. . . . 56
4.2 Sensor placement on the demonstrator and the data acquisition chain. . . . 57
4.3 Diagram of the Signal Treatment stage of the program. . . . 58
4.4 Diagram of the CI Computation stage of the program. . . . 59

5.1 Assembled demonstrator at INEGI's facilities. . . . 60
5.2 Simplified 3D model of the modified test rig, excluding the structural base, the motor and the first reduction stage. . . . 62

6.1 Test rig layout used for data acquisition. . . . 64
6.2 Segment of the tachometer signal (Voltage) at 3000 rpm. . . . 65
6.3 Number of samples per revolution in the preliminary tests. . . . 66

6.4 Amplitude spectrum of the raw signal acquired at 3000 rpm, with the shaft rotational frequency and the meshing harmonics indicated. 67
6.5 Condition of the gear pair at the first and last inspections of the campaign. 70
6.6 Tooth tips of the output gear at the start and at the end of the campaign. 71
6.7 Raw acceleration signal of a record acquired during the first test session, showing the isolated spikes coincident with the audible clicking. 73
6.8 Coating particles in the test rig at the end of testing. 74
6.9 Coupling between the motor and shaft I after the failure. 74
6.10 Raw vibration data from the record preceding the coupling failure. 75
6.11 RMS of the raw, TSA and difference signals over the whole campaign. 76
6.12 Maximum peak acceleration of the raw signal over the whole campaign. 77
6.13 Kurtosis of the raw, TSA and difference signals over the whole campaign. 77
6.14 FM4 over the whole campaign. 78
6.15 ER across the whole campaign. 79
6.16 ER over the final test day, with the RMS of the difference signal $d(n)$ and of the regular meshing signal $y_{reg}(n)$ from which it is computed. 80
6.17 Kurtosis of the envelope obtained at the selected demodulation band, over the whole campaign. 81
6.18 ALR against the first record of the campaign. 82

List of Tables

2.1 Nomenclature of gear failure modes (adapted from ISO 10825-1:2022). [21] . . . 9
2.2 Boundary values of housing vibration true peak acceleration for two acceleration ratings (adapted from ISO 20816-9). [41] . . . 24
2.3 Overview of the CIs considered. . . . 28

3.1 Operating characteristics of the BLDC motor. . . . 33
3.2 Required pressure differential for target torque range ($T_{min} = 0.25$ Nm, $T_{max} = 1.5$ Nm, $\eta_0 = 0.8$) . . . 35
3.3 Geometric and physical parameters of the ECB prototype. . . . 37
3.4 Definition of the magnetostatic finite element model and material properties assigned to each region (FEMM 4.2 [52]). . . . 37
3.5 M.1703.2221 rated operating characteristics. . . . 40
3.6 Main characteristics of the gears considered for the demonstrator. [54], [55], [56], [57] . . . 40
3.7 Characterization of reduction stages. . . . 42
3.8 Design data and modelling assumptions. . . . 43
3.9 Marin modifying factors at the groove of shoulder B. . . . 47
3.10 Stations contributing to the first critical speed, grouped by diameter. . . . 51

6.1 Verification of the measured shaft speed against the theoretical value, for the speeds tested in the preliminary runs. . . . 65
6.2 Operating conditions adopted for the monitoring campaign. . . . 68
6.3 Schedule of the experimental campaign. . . . 68

List of Acronyms

AC Alternating Current

ALR Averaged Logarithmic Ratio

AR Acceleration Rating

BLDC Brushless Direct Current

BPFI Ball Pass Frequency of the Inner race

BPFO Ball Pass Frequency of the Outer race

BSF Ball Spin Frequency

CI Condition Indicator

DC Direct Current

DT Digital Twin

ECB Eddy Current Brake

ER Energy Ratio

FFT Fast Fourier Transform

FTF Fundamental Train Frequency

GMF Gear Mesh Frequency

GTE Geometric Transmission Error

HTD High Torque Drive

INEGI Instituto de Ciência e Inovação em Engenharia Mecânica e Engenharia Industrial

ISO International Organization for Standardization

JIS Japanese Industrial Standards

LSTM Long Short-Term Memory

NdFeB Neodymium Iron Boron

PdM Predictive Maintenance

PETG Polyethylene Terephthalate Glycol

PLA Polylactic Acid

ResNet Residual Network

RMS Root Mean Square

RUL Remaining Useful Life

SBR Sideband Ratio

SDG Sustainable Development Goals

SK Spectral Kurtosis

STFT Short-Time Fourier Transform

STM ST Microelectronics

TSA Time Synchronous Average

Chapter 1

Introduction

1.1 Motivation

With the start of Industry 4.0, the industrial landscape has become a connected and automated ecosystem where data is the main driver for operational efficiency. In this context, the economic impact of equipment downtime remains one of the most relevant issues for modern production lines, since stoppages are accompanied by lost revenue, wasted labour and possible secondary damage to connected machinery. In heavily automated industries, a single day of downtime can cost hundreds of thousands of dollars [1], and inadequate maintenance strategies are estimated to reduce the usable production capacity of a plant by 5 to 20 % [2].

Historically, industrial maintenance has relied on "scheduled" or preventive models, which are time-based: components are replaced or fixed at predetermined intervals regardless of their actual physical state [3]. While this is usually superior to a purely reactive "run-to-failure" approach, it brings fundamental inefficiencies, namely the premature disposal of healthy parts and the failure to prevent breakdowns caused by unforeseen operating conditions [1, 4]. Industry 4.0 promotes instead predictive maintenance (PdM), in which real-time data is used to determine the actual state of a system so that interventions occur only when necessary [5, 6].

Applying this to mechanical systems presents a physical challenge: the difficulty of measuring wear without stopping production. Internal components are often inaccessible, and measuring subtle signs of degradation might require disassembly, which causes the very downtime that maintenance is intended to prevent [7]. Digital Twin (DT) technology fills this gap by pairing the physical asset with a virtual model of it, kept synchronized by real-time sensor data [2, 8]. Because the model is continuously corrected by measurements taken on the running machine, it can be interrogated for quantities that are not directly observable, such as the local material loss on a contacting surface, and used to estimate the remaining useful life of a component while the system is in operation. Reviews of industrial implementations report reductions in unplanned downtime in the order of 15 to 30 % when this type of framework replaces purely time-based planning [8].

Gear transmissions are a particularly relevant target: they are present in a large number of industrial drivetrains, they are enclosed and therefore difficult to inspect, and their degradation is

progressive rather than instantaneous. A physics-based gear model whose wear parameters are updated from vibration measurements has been shown to track and extrapolate wear progression with useful accuracy, but only after being established and validated on a laboratory gear rig [9]. This is the practical obstacle. Validating a predictive methodology requires degradation data, and degradation data is expensive: in a real installation, wear develops over months or years, operating conditions cannot be freely manipulated, and running a component to failure on purpose is not usually an acceptable option. A scaled demonstrator compresses that timescale, gives full control over speed and load, and allows the true condition of the component to be inspected at any point, providing the experimental ground truth against which any monitoring indicator has to be judged.

The present work follows that reasoning by keeping the scale of the demonstrator small, relying on low-power components and on construction solutions seldom seen in comparable test rigs, such as extruded aluminium profiles and 3D-printed polymer parts. This makes a test article cheap enough to be disposable, brings the rig into a size and power range that can be operated safely and continuously on a bench. It also introduces its own questions, the vibratory behaviour of a printed polymer part is not the same as of a machined metal one and the demonstrator must be able to accelerate wear enough to observe a complete degradation history in a matter of days, which is made more complex when dealing with lower power grades and lighter support materials.

This dissertation was developed in collaboration with INEGI, in whose context such demonstrators have a value beyond the scientific one. A rig that can be carried into a meeting room and made to display the evolution of a condition indicator in real time materializes knowledge, serves as a platform for training and for testing new signal processing techniques, and allows the ideas behind a DT to be consolidated before any commitment is made to instrument a real machine.

1.2 Objectives

The objective of this work is the construction of a DT of a mechanical system: a numerical model of a gear transmission, kept in correspondence with the physical system through the vibration measurements taken from it, capable of inferring the wear state of the gear pair and, from it, its remaining useful life. A DT of this kind cannot be built, and still less validated, without a degradation history acquired under controlled conditions and a set of condition indicators tested against it. Designing and building a system in which wear can be induced in a controlled way and detected reliably from vibration is therefore a substantial part of the problem, and the specific objectives follow from it:

- assess the state of the art regarding DT applications in PdM, including selection of methods and case studies;
- to design and build a compact, instrumented test rig in which a mechanical system can be run continuously under controlled conditions until failure;
- to acquire a complete vibration history of that degradation process, together with periodic inspection of the physical condition of the system;

- to implement and compare vibration-based condition indicators, and to assess which of them track the progression of wear reliably and with the earliest detection;
- to establish, from the above, possible methods of wear quantification and of remaining useful life estimation, and to integrate them with the physical system into a DT of the transmission.

1.3 Structure of the Dissertation

Chapter 2 reviews the literature. The adopted case study, a single-stage spur gear pair, is introduced and justified, starting from the definition and terminology of wear and the forms it takes in gear pairs, and then examining how each of those forms, together with the shaft, bearing and pulley faults that accompany them, alters the vibration signature of a transmission. An exposition of various methods of wear evaluation is made.

Chapter 3 covers the design of the demonstrator: the requirements it had to meet, the comparison and selection of the components, ending with the completed design. Chapter 4 describes the computational implementation, from the instrumentation and the flow of data to its treatment and the calculation of the condition indicators. Chapter 5 reports the assembly of the rig, the limitations found once it was running and the modifications made to overcome them. Chapter 6 presents the experimental campaign, first the operating conditions and the results of the individual test days, and then the trend of each condition indicator over the full life of the gear pair. Chapter 7 summarises the conclusions and future work to be done.

Chapter 2

Literature Review

This chapter provides the theoretical background on which the rest of the work is built. It begins with a definition of wear, its mechanisms and terminology, followed by a review of the test rigs built for wear evaluation in the literature, from which the case study of the present work, a single-stage spur gear pair, is defined. The vibratory consequences of degradation are addressed next, covering the signature of a healthy gear pair, the way wear modifies it and the contribution of the surrounding shafts, bearings and pulleys, together with the models that link surface degradation to that signature. The chapter closes with the methods used to infer the state of the system from the measured signal, from signal treatment to the condition indicators and to machine learning approaches. Even though wear quantification is not the main focus of this work, some form of wear tracking algorithm has to be employed in order to verify the demonstrator's capability of producing wear detectable through vibration, and the review of the methods employed in spur gear systems serves as support for future work developed with the proposed physical demonstrator.

2.1 Wear

2.1.1 Definition and terminology

In the most general sense, every physical system or machine is subject to a progressive loss of effectiveness and functionality over time, this broad concept of wear describes the unavoidable degradation that occurs when components interact, eventually leading to the end of a machine's useful life. This may manifest in a physical alteration of the geometry of the components, misalignment between mating parts or a change in the properties of the materials.

According to Rabinowicz [10], wear is a universal process where the interaction of solid surfaces inevitably leads to a decline in their original state. Similarly, Hutchings and Shipway [11] characterize this broad nature of wear as the progressive damage to a solid surface caused by relative motion, emphasizing that it is a functional consequence of the system's operation rather than an isolated event.

While these broad definitions encompass the general decline of a system's performance, a narrower and more operative definition is required for engineering analysis and predictive maintenance. In this technical framework, wear is specifically defined as "the displacement or removal of material from a solid surface due to mechanical or chemical action." This distinction allows for the quantification of degradation as a physical change in geometry rather than just a loss of efficiency. Depending on the environment and the nature of the contact, this material loss can be classified into several mechanical wear mechanisms, as explored by Burwell [12] and Hutchings and Shipway [11]:

- **Adhesive wear:** Occurs when the high points (asperities) of two surfaces bond together under pressure and are subsequently sheared or torn during relative motion, depending on the location and severity of this mechanism it may evolve into scuffing which is usually treated separately in the literature.
- **Abrasive wear:** Involves a harder surface or particle cutting or plowing into a softer surface, effectively "machining" away material. Two common variants are "two-body" and "three-body" abrasive wear, it is referred as two-body abrasive wear when the asperities or hard protuberances of one body cut into the other surface, and it is called "three-body" when the abrasion is caused by hard particles in the contact interface. This type of wear may be further characterized as "sliding" or "rolling" wear, depending on the kinematics of the abrasive body.
- **Surface fatigue:** Usually involves the formation of pits or flakes in the loaded surface, due to the propagation of subsurface cracks. The rolling motion between the surfaces over a large number of cycles causes this fatigue phenomenon, the physical wear product may be characterized according to the size and interaction of defects as "micro" and "macro" pitting and spalling.
- **Erosive wear:** It is a mechanism similar to abrasive wear, and may even be considered a type of abrasive wear, however, while in abrasive wear the damage is caused by sliding or rolling between bodies, it is considered erosive wear when the damage is produced by the impact of particles, droplets, or high-velocity fluids against the surface.

2.1.2 Case Studies in the Literature

Experimental work on vibration-based wear evaluation falls into two broad families. The first consists of purpose-built laboratory rigs, in which a single component is isolated, instrumented and run until a controlled form of degradation develops. The second consists of full-scale or in-service systems, where the monitored component is embedded in its real operating environment and the measurement must contend with the excitation and transmission paths of the whole machine. The distinction matters because it determines how directly the measured signal can be attributed to the fault: the isolated rig trades realism for a clean signal and a known ground truth, while the full-scale system offers realism at the cost of a far more congested signal.

Rolling Element Bearings

Bearings are the most frequently instrumented component in the diagnostics literature, largely because their characteristic frequencies follow directly from the geometry and because faults can be seeded reproducibly. Daga et al. [13] describe the rolling bearing rig of the Dynamic and Identification Research Group at Politecnico di Torino, in which a high-speed spindle drives a shaft supported by two roller bearings, with the radial load applied by a third bearing mounted on a spring-loaded sledge. Damage was introduced artificially and acquisitions were taken across speeds up to 30 000 rpm and loads up to 1800 N. The authors also report an endurance test of roughly 330 h at constant speed and load, intended to follow the natural evolution of one of the seeded indentations. That second experiment is instructive for the present work: the defect widened while flattening, the resulting change in the statistical features was weak, and the measured novelty indices proved more sensitive to the disassembly of the bearing for inspection and to a change of lubricating oil than to the degradation itself [13].

Cutting Tools

Tool condition monitoring shares the same signal-processing toolbox but concerns a component whose wear is comparatively rapid. Tiwari et al. [14] monitored flank wear of a PVD-coated carbide insert turning a Nickel-based superalloy, comparing three discrete states labelled “no wear”, “medium wear” and “high wear” against the 0.6 mm flank wear limit. The RMS of the vibration signal rose from 3.21 to 10.07 across the three states, and the dominant tool-holder resonance in the 2–4 kHz band both grew in magnitude and shifted in frequency as wear progressed. Empirical mode decomposition was used to isolate the most informative intrinsic mode, with kurtosis identified as the indicator that tracked wear most consistently.

Railway Systems

Two railway studies illustrate the full-scale end of the spectrum. Liu et al. [15] built a 1:1 rolling and vibration test rig for a single high-speed wheelset, in which the wheelset is driven by two rail wheels under a simulated axle load of about 12 tonnes at speeds up to 500 km/h. Polygonal wear was reproduced by grinding 36 points into the rail wheel contact band. Accelerometers on the axle box and on the gearbox allowed the contributions of the three excitation sources to be separated: at 240 km/h, wheelset out-of-roundness, polygon wear and track irregularity accounted for 26.7%, 48.3% and 25% of the axle-box amplitude, and 38.5%, 32.1% and 29.5% of the gearbox amplitude.

Najeh et al. [16] took the opposite approach on a full-scale switch and crossing rig, dragging a 6-tonne bogie over the turnout at roughly 0.017 m/s with all six accelerometers housed inside the point machine, an optimal location for protection but distant from the defect. Wear was created artificially on the rail head in four levels, measured mechanically with a rail wear gauge and ranging from about 0.5 to 8 mm depending on position, and the vibration records were classified with Long Short Term-Memory (LSTM) and Residual Network (ResNet) architectures. Accuracy

reached 88% for the LSTM and slightly higher for the ResNet, but both models struggled to separate the two intermediate levels differing by only 1–2 mm, which shows the resolution limit of a purely data-driven approach when the sensor is far from the damage.

Gear Systems

Gear studies divide further according to the configuration of the transmission. For planetary gearboxes, Zhang et al. [17] used a single-stage rig driven by a 2.24 kW motor, running at 1800 and 3000 rpm with three seeded sun gear health states, and assessed the fault through the amplitudes of the sideband families around the meshing frequency. Miao and Zhou [18] likewise validated an analytical vibration signal model on a planetary rig with a seeded planet gear fault. In both cases the damage is introduced rather than grown, and the interest lies in the modulation produced by the rotating carrier rather than in the wear process itself.

For fixed-axis spur gearboxes, three run-to-failure campaigns are particularly relevant. Hu et al. [19] conducted accelerated lifetime tests at the University of New South Wales on unhardened, unground steel spur gears at 1380 rpm and 14.7 Nm, approximately 2.2 times the rated load for surface damage, under splash lubrication. Two tests were run, one starting from the factory surface finish and lasting 82 h, the other with artificially seeded pits and roughened flanks lasting 62 h. Vibration and oil samples were taken every two hours, the latter providing an independent assessment of the wear process against which the proposed indicator was validated.

Chin et al. [20] used a single-stage spur gearbox driven by a 4 kW induction motor and loaded by an electromagnetic particle brake, with a 19-tooth pinion and 52-tooth gear of module 2 mm in mild steel JIS S45C and 20 mm face width, the teeth deliberately left with low surface durability so that surface degradation would precede bending fatigue. Two campaigns were run: a dry test at 10 Hz and 5 Nm over about 42 000 input cycles, in which abrasive wear dominated and wear particles were collected and weighed, and a lubricated test over 3.25 million cycles in which fatigue pitting developed progressively. Transmission error was measured with shaft-mounted encoders alongside casing vibration, and the RMS of the transmission error signal was shown to follow the measured pitted area closely, with the authors concluding that transmission error was the more sensitive of the two quantities in that case.

The same rig underpins the digital twin methodology of Feng et al. [9], where a 20-degree-of-freedom dynamic model of the gearbox is updated against measured transmission error features. Wear was quantified by replicating the tooth surfaces with a moulding compound at predetermined stops and examining the moulds under optical and laser scanning confocal microscopy, yielding wear depth measurements that served as ground truth for the prognostic model. Abrasive wear dominated in the unlubricated tests, with adhesion and plastic deformation also observed as the degradation progressed.

2.1.3 Selected Configuration

A single-stage spur gear pair was selected as the object of the physical demonstrator, for three main reasons.

First, gears are very well established in the industrial transmissions targeted by PdM, and their vibration signature is well characterised both analytically and experimentally, which provides a large body of reference results against which the demonstrator can be validated.

Second, and most importantly for this work, gears degrade progressively. Surface wear, micropitting and macropitting develop gradually over a large number of cycles and produce a correspondingly gradual change in the tooth profile and hence in the transmission error. This is precisely the behaviour required to test a wear evaluation algorithm, since it generates a continuum of intermediate states rather than a binary healthy-or-damaged transition.

Finally, the test rigs most often seen in the literature have generally bigger dimensions: they use large gearboxes, high power three-phase motors and heavy load-imposing mechanisms, making it a particularly interesting concept to replicate in a more compact scale.

2.1.4 Wear in the Context of Gears

When applying these concepts specifically to gear transmissions, the terminology is further refined to distinguish between acceptable surface changes and catastrophic failure and to better represent common mechanisms present in these units. The International Organization for Standardization (ISO), in the standard ISO-10825, provides industry-standard terminology for describing these phenomena. Within this standard, non-fatigue, tribological wear is specifically defined as “changes to a gear tooth flank surface involving the removal of material without any evidence of fatigue cracks”. [21]

ISO-10825-1 distinguishes between mild wear, which may even be a beneficial part of the "running-in" process that smooths the tooth surface, moderate wear, and destructive wear, which significantly alters the involute profile and leads to increased vibration and transmission error [20, 21]. Furthermore, the standard provides specific terminology for failure modes that are related to wear but distinct in their visual and physical appearance, a summarizing table was adapted from the contents of the standard to give a general overview on the most relevant wear modes to this application (Table 2.1).

Regarding quantification of wear, as a general rule, mild wear is characterized visually as the appearance of minor changes to the gears’ flank or tooth profile, indicative of the type of wear mechanism taking place, but retaining most of the original machining marks, meaning there was no major alteration of the tooth flank’s topological profile. It is considered that severe wear has occurred when all or nearly all original machining marks have been erased by wear, usually resulting in significant changes to the tooth’s profile and flank surface. Moderate wear is visually characterized as a balance between the two aforementioned states. (See Figure 2.1).

It should be noted that gear wear may even give us information on other faults present in the system, such is noticeable in Figure 2.1f, where wear intensity has a clear gradient in the axial

Table 2.1: Nomenclature of gear failure modes (adapted from ISO 10825-1:2022). [21]

Type of damage	**General mode**	**Description**
Tribological damage (non-fatigue)	Polishing (unintentional)	Gradual smoothing of the flank by very fine abrasion, erasing machining marks and slowly altering the profile.
	Scratches	Fine grooves aligned with the sliding direction, cut by hard particles carried in the lubricant.
	Abrasive wear	Material removed by hard debris – swarf, scale, sand – suspended in the oil or embedded in the mating flank.
	Adhesive wear	Microwelding of asperities followed by tearing, transferring material between flanks; escalates to scuffing.
	Fretting corrosion	Oxidation-assisted damage from small-amplitude oscillation between nominally stationary contacting surfaces.
	Interference wear	Rubbing outside the intended contact path, where the tip of one tooth bears on the root of its mate.
Fatigue damage	Micropitting	Asperity-scale Hertzian fatigue producing ultra-fine cracks and pits typically under 20 µm deep; appears as a dull grey band.
	Macropitting	Hertzian fatigue cracks that grow until visible flakes of flank material detach, leaving craters.
	Case crushing (subcase fatigue)	Fatigue initiating beneath the hardened case, at the case–core boundary, collapsing the case over large areas.
	White layer flaking	Detachment of a brittle untempered-martensite layer formed by localised frictional overheating.
	Tooth fracture	Fatigue crack propagating through the tooth, initiating either at the root fillet under bending stress (root fatigue fracture), at a subsurface inclusion below the active flank, or internally near mid-height under alternating flank loading.
	Rim, web, and hub cracks	Fatigue cracking of the gear body rather than the teeth; typical of thin-rimmed or lightweight designs.
Plastic deformation	Indentation	Localised dents left by debris trapped in the mesh or by impact during handling and assembly.
	Root fillet yielding	Permanent bending of the tooth at the fillet under a load exceeding the yield strength.
	Cold flow	Slow plastic displacement of surface material under repeated contact, without significant temperature rise.
	Hot flow	Plastic displacement accelerated by frictional heating, producing rippling or ridging of the flank.
	Interference deformation	Permanent set caused by tip-to-root contact or by an excessively tight mesh.
Other surface damage	Corrosion	Chemical or electrochemical attack of the flank, usually from water ingress or acidic lubricant degradation products.
	Overheating	Discolouration and loss of surface hardness caused by excessive bulk or flash temperature.

direction, this is a possible indicator of shaft misalignment. Phenomena like this often manifests in the vibration signature of the system and can be used for general diagnostic techniques, which will be discussed later in this Chapter.

2.2 Effect of Wear on Gear Dynamics.

Like any dynamic mechanical system, gearboxes inherently produce vibration when in operation even with no wear present in the system. Purely based on the regular meshing dynamics, there will be a set of characteristic frequencies and vibration patterns associated with the gears and operating conditions employed that must be accounted for when managing the vibrational data.

2.2.1 Healthy Gear Vibration Signature

Under constant speed and load, a healthy gear set produces a repeatable vibration signature [26], [27]. The time-domain waveform is dominated by the steady harmonic pattern of successive teeth entering and leaving mesh and, since every tooth is nominally identical, each meshing cycle closely resembles the one before it. Transposed into the frequency domain, this regularity concentrates the energy into a small number of discrete peaks: the shaft rotational frequencies and the Gear Mesh Frequency (GMF) accompanied by its lower-order harmonics. The meshing frequency itself follows directly from the kinematics of the pair [26], [28]:

$$f_{\mathrm{GMF}} = z \cdot f_r \tag{2.1}$$

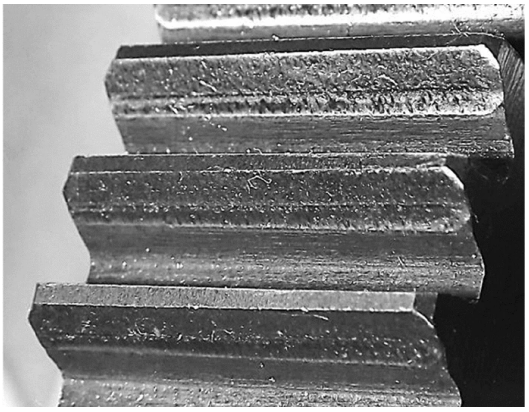
- f_{GMF} — gear mesh frequency [Hz];
- z — number of teeth of the gear under consideration;
- f_r — rotational frequency of the shaft carrying that gear [Hz].

A more complete description is obtained once the signal has been time synchronous averaged (TSA), a procedure that suppresses every component not phase-locked to the shaft of interest and leaves the meshing vibration as a sum of amplitude- and phase-modulated sinusoids [19], [29]:

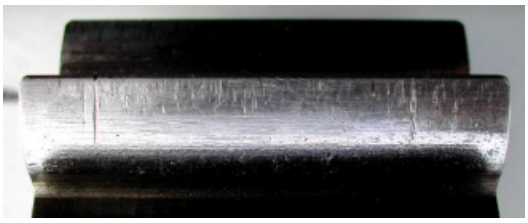
$$x(t) = \sum_{k=1}^{K} X_k[1 + a_k(t)] \cos\left(2\pi k Z f_r t + \Phi_k + b_k(t)\right) \tag{2.2}$$

Where

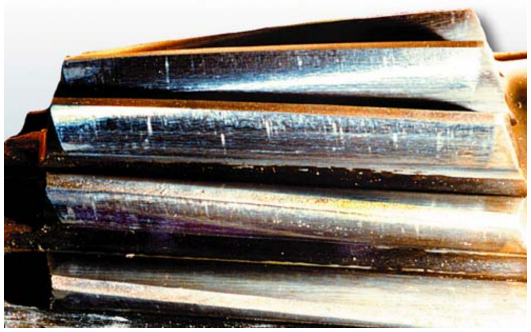
- $x(t)$ is the time synchronous averaged vibration signal;
- K is the number of meshing harmonics retained in the model;
- X_k is the deterministic amplitude of the k-th meshing harmonic;
- Φ_k is the initial phase of the k-th meshing harmonic [rad];



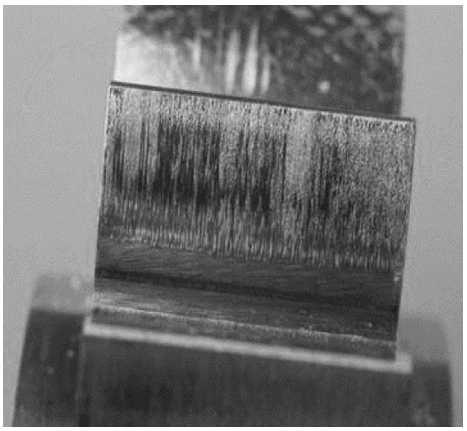
(a) Mild abrasive wear. [22]



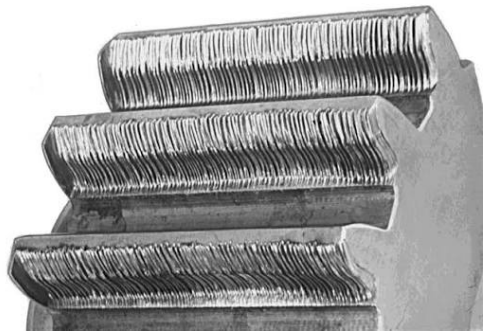
(b) Mild scuffing. [23]



(c) Moderate adhesion wear. [24]



(d) Moderate hot scuffing. [25]



(e) Severe abrasive wear. [24]



(f) Severe polishing wear. [21]

Figure 2.1: Various severities of gear tooth surface wear, similar to as depicted in ISO-108251-1.[21]

- $a_k(t)$ is the amplitude modulation function of the k-th harmonic;
- $b_k(t)$ is the phase modulation function of the k-th harmonic [rad].

The diagnostic value of this formulation lies almost entirely in the two modulation terms. When the gear is healthy, $a_k(t)$ and $b_k(t)$ remain small and vary slowly, so the spectrum shows only low-amplitude and approximately symmetric sidebands spaced at the shaft rotational frequency around each meshing harmonic ($f_{\mathrm{GMF}} \pm n \cdot f_r$) [19], [26], [27]. Such sidebands never vanish completely, since manufacturing tolerances and mounting eccentricities always introduce a residual amount of modulation. This baseline, illustrated in Figure 2.2, is the reference against which every deviation discussed in the remainder of this section must be interpreted.

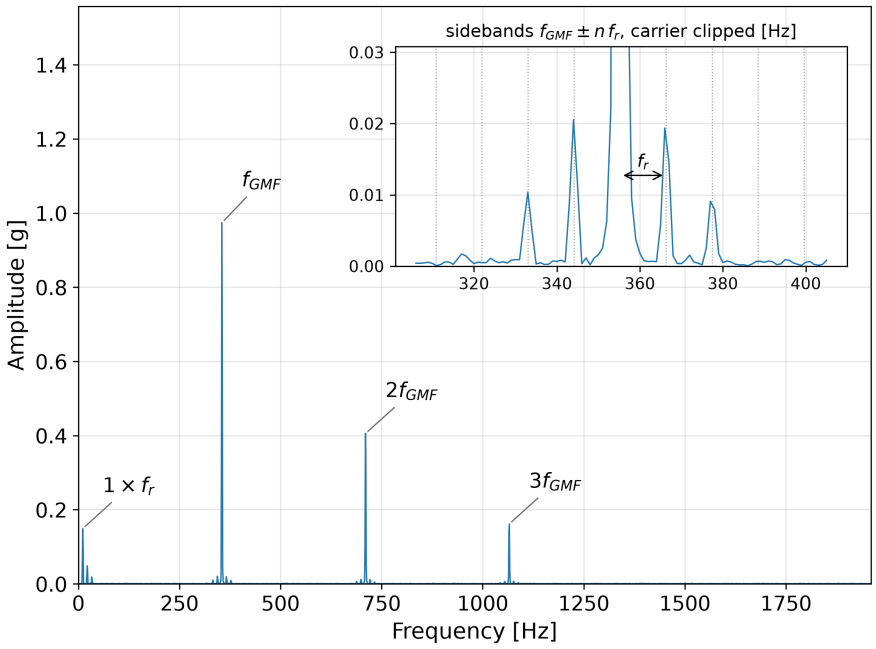


Figure 2.2: Frequency spectrum of a synthesized healthy gear meshing signal.

2.2.2 Uniform Wear

Uniform wear describes progressive material loss that affects every tooth in essentially the same manner, and is typically driven by abrasive mechanisms operating under boundary or mixed lubrication [19], [30]. Its shape is dictated by the kinematics of the mesh: contact between mating flanks combines rolling and sliding, with the sliding velocity falling to zero at the pitch line and reaching its maximum near the tooth root (dedendum) and tip (addendum) [30], [31]. Because material removal follows the sliding distance, the flank is eroded most severely at those two extremes while the pitch region stays comparatively intact, which gives each active tooth flank the characteristic "double-scalloped" deviation from the ideal involute profile [31]. The outcome is a slow, systematic distortion of the average working surface, and therefore a steady growth of the geometric transmission error (GTE) [19], [30].

This distinction matters when the signature is examined. Since all teeth degrade together, the tooth-to-tooth differences that normally feed the modulation functions barely increase, and the sidebands consequently remain low [19], [31]. What does change is the shape of the once-per-tooth excitation: a periodic waveform that departs from its original form while preserving its period can be described by adding higher-order terms, so the energy increases towards the upper meshing harmonics [19], [26], [31]. A pronounced rise in $2f_{\mathrm{GMF}}$ and $3f_{\mathrm{GMF}}$ with little or no sideband activity, as sketched in Figure 2.3, is thus the fingerprint of distributed wear, and trending these components over time remains one of the most reliable ways of catching it early [30], [31].

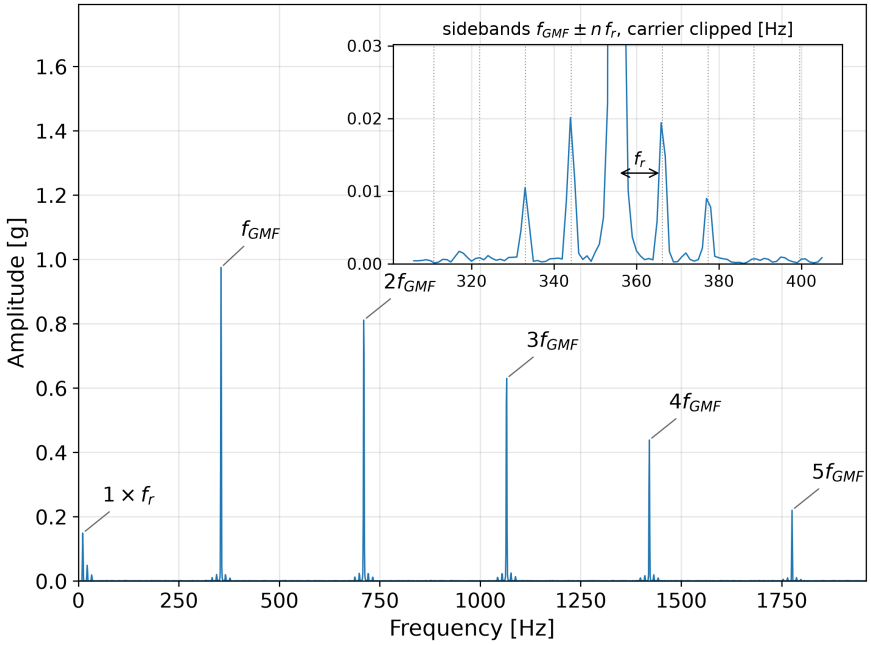


Figure 2.3: Typical spectrum changes due to uniform wear.

2.2.3 Localized Wear

It is also common for defects to appear where damage is confined to a single tooth or to a small group of teeth, which usually appears as fatigue pitting, spalling or a crack at the tooth root [30], [32]. A defect of this kind lowers the local bending stiffness and reduces the active contact area of the affected tooth during the short interval in which it carries load [29], [32]. The result is a structural discontinuity that the rest of the mesh does not share, producing a transient impulsive excitation and a heavy modulation of the meshing vibration once per revolution of the damaged tooth [29], [31].

Both domains reflect this behaviour clearly. The synchronously averaged waveform develops distinct spikes, or occasionally amplitude dips, at the angular position of the faulty tooth [26], [29]. Because a short-duration transient spreads its energy over a wide frequency range, the spectrum responds with a broad and comparatively flat family of sidebands around the meshing harmonics,

spaced at the rotational frequency of the faulty gear [26], [29], [31]. These sidebands are frequently unsymmetrical and, in advanced stages, may even exceed the amplitude of the mesh carrier itself, as represented in Figure 2.4 [26].

The two dominant failure modes are nevertheless not interchangeable from a monitoring standpoint. When a fatigue crack propagates at the root, the tooth deflects more than its neighbours under the same load, and this additional compliance is expressed mainly as a timing error: the tooth engages late and disengages early, producing a pronounced phase lag that can approach 60° at the higher mesh orders [28], [29]. Phase demodulation of the meshing harmonics is therefore considerably more sensitive to an incipient crack than amplitude demodulation [29], [31]. Pitting behaves differently. It originates from cyclic subsurface contact stresses that nucleate micro-cracks near the pitch line, and once material spalls away the contact area is locally reduced [30]. In its milder stages the damage is too small and too irregular to produce a coherent phase disturbance, and instead excites high-frequency random vibration associated with sliding over the roughened surface, which is best captured by second-order cyclostationary indicators rather than by low-frequency demodulation [30], [31].

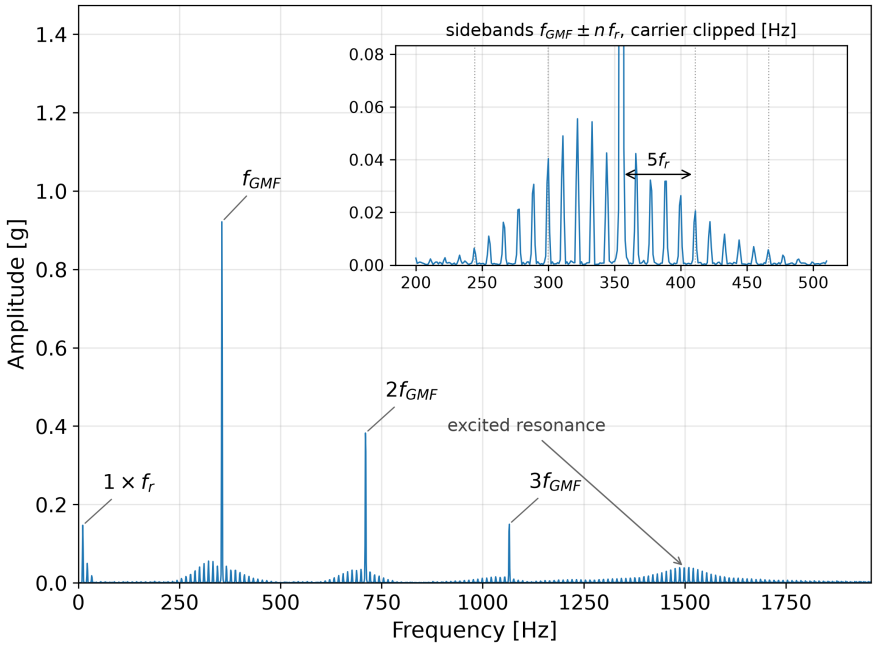


Figure 2.4: Frequency spectrum of a localized gear fault, characterized by wide, high-amplitude, unsymmetrical sideband families around the meshing harmonics.

2.2.4 Shaft Related Wear

Not every anomaly recorded by an accelerometer mounted on a gearbox originates at the tooth flanks. Unbalance, parallel or angular misalignment, a bent shaft and radial eccentricity all leave signatures that overlap with those of gear damage and must be recognised before any conclusion is drawn about the mesh itself [26], [28], [31]. Mechanically, a bent or misaligned shaft carries

static and dynamic bending moments that rotate with it, forcing the shaft into an orbital motion that periodically alters the centre distance and the relative alignment of the meshing gears [31].

Two effects follow from this. The first is direct: high-amplitude radial and axial vibration appears at the fundamental shaft speed (1×) and at its low-order harmonics (2×, 3×), with the axial component being particularly indicative of angular misalignment [26], [28], [31]. The second is indirect, since the cyclic variation in centre distance imposes severe amplitude and phase modulation on the meshing vibration, surrounding f_{GMF} with prominent and closely grouped sidebands [26], [28]. Their spacing is what makes the diagnosis possible: because the sidebands are separated by the rotational frequency of the offending shaft, the spacing identifies which of the two shafts is responsible, even though the modulation is observed on a component generated by both.

2.2.5 Bearings

Rolling element bearings fail through localized defects on the inner race, the outer race, the cage or the rolling elements themselves [26], [28], [31]. Each time a rolling element traverses such a defect it generates a sharp, high-frequency impact force, and since the kinematics of the bearing are fully determined by its geometry, these impacts repeat at fixed and predictable rates [26], [28], [31]. The four characteristic frequencies are given by [26], [28], [31]:

$$\mathrm{BPFO} = \frac{n \cdot f_r}{2}\left(1 - \frac{d}{D}\cos\phi\right) \tag{2.3}$$

$$\mathrm{BPFI} = \frac{n \cdot f_r}{2}\left(1 + \frac{d}{D}\cos\phi\right) \tag{2.4}$$

$$\mathrm{FTF} = \frac{f_r}{2}\left(1 - \frac{d}{D}\cos\phi\right) \tag{2.5}$$

$$\mathrm{BSF} = \frac{D \cdot f_r}{2d}\left[1 - \left(\frac{d}{D}\cos\phi\right)^2\right] \tag{2.6}$$

Where

- BPFO is the ball pass frequency of the outer race [Hz];
- BPFI is the ball pass frequency of the inner race [Hz];
- FTF is the fundamental train (cage) frequency [Hz];
- BSF is the ball spin frequency [Hz];
- n is the number of rolling elements;
- f_r is the relative rotational frequency between the inner and outer rings [Hz];
- d is the rolling element (ball) diameter [mm];
- D is the bearing pitch diameter [mm];

- ϕ is the contact angle [rad].

Locating these frequencies in the raw spectrum is, however, rarely possible. The impacts are relatively weak and act mainly as an excitation of the structural resonances of the housing, typically in a higher frequency region, so the low-frequency region where they nominally appear is dominated by the more energetic shaft and meshing components [26], [28]. Recovering them requires envelope analysis: the signal is band-pass filtered around the housing resonance frequency and amplitude demodulated, which discards the carrier and retains only the repetition rate of the impacts, bringing the bearing frequencies clearly into view [28], [31]. Figure 2.5 contrasts the raw and envelope spectra for a defective bearing. Two additional effects are worth noting when the bearing is installed in a gearbox: the defect can modulate the meshing vibration and create sidebands around f_{GMF} spaced at the bearing characteristic frequencies, while looseness in the bearing housing tends to excite exact half-order subsynchronous harmonics ($0.5\times$, $1.5\times$, $2.5\times$) of the shaft rotating speed [26], [31].

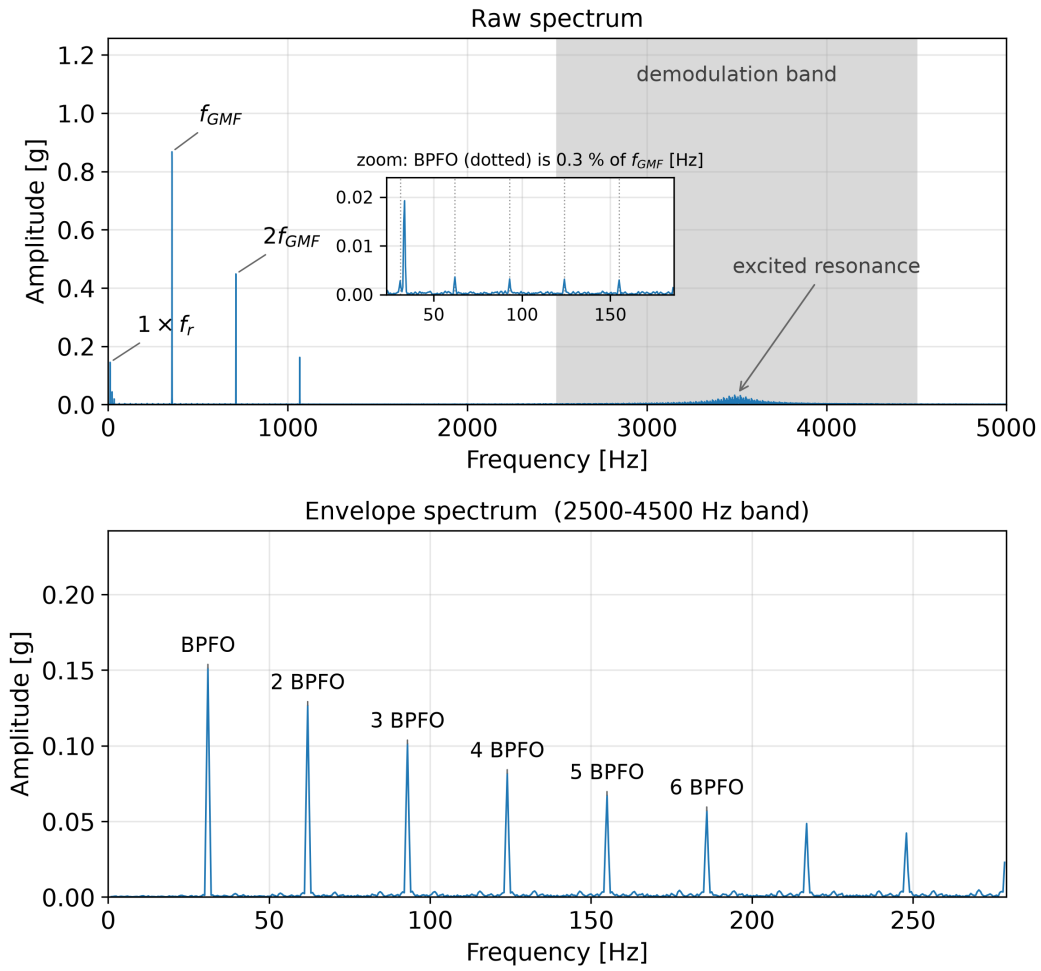


Figure 2.5: Synthesized raw and envelope spectra of a rolling element bearing with an outer race defect.

2.2.6 Pulleys

Where power is transmitted by belts, a further group of anomalies arises from belt slip, loss of tension, pulley eccentricity and pulley misalignment [26]. As a belt wears or loosens it begins to fluctuate transversally to the shaft axis during operation, and the periodic impact and friction forces that come with this motion are what the accelerometer registers [26]. The rate at which they repeat is the belt pass, or flexural, frequency [26]:

$$f_b = \frac{\pi \cdot f_r \cdot d_p}{L} \tag{2.7}$$

- f_b is the belt pass (flexural) frequency [Hz];
- f_r is the rotational frequency of the pulley [Hz];
- d_p is the pulley pitch diameter [mm];
- L is the total belt length [mm].

A worn or slack belt reveals itself through prominent but unstable peaks at f_b and at its integer harmonics ($2f_b$, $3f_b$, $4f_b$), the instability being a direct consequence of the slip that produced them in the first place [26]. The remaining two faults are easier to separate: misalignment between pulleys produces high-amplitude axial peaks at the rotational speeds of the individual pulleys, whereas eccentricity produces a purely radial peak at the rotating frequency of the eccentric pulley alone [26].

2.3 Dynamic Models of Gear Systems

As established in the beginning of the chapter, wear consists of the "displacement or removal of material from a solid surface" and so it represents a direct change in the mechanical and geometric properties of the system. This makes it natural for the development of precise dynamic models with the ability to mirror the physical behaviour of the gears affected by wear to be a target of research, as well as the capability of doing the inverse logic of inferring the wear state from measured vibration.

2.3.1 The Wear Dynamics Feedback Loop

The physical core of model-based gear diagnostics is a coupled interaction: sliding and rolling contact under high load removes material from the tooth flank, altering its geometry; this profile deviation changes the system's Dynamic Transmission Error and Time-Varying Mesh Stiffness, generating larger meshing forces that subsequently accelerate the wear rate [33], [34]. Ren and Yuan [33] describe this as a two-way relationship that yields more complex dynamic behaviour than a fault which perturbs the system in only one direction, and identify it as the reason why surface wear is harder to monitor than most other gear failure modes.

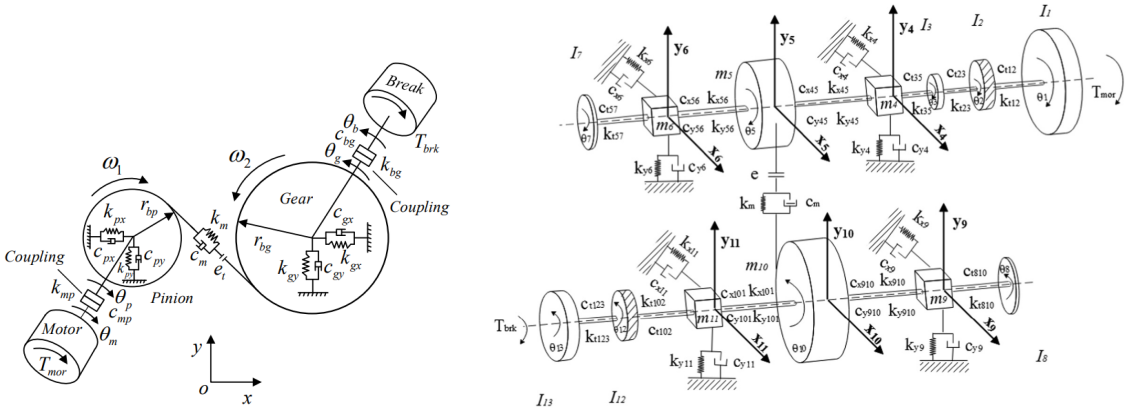
The macro-mechanical behaviour of a fixed-axis spur gear transmission is typically simulated using a lumped-parameter lumped-mass model [33], [35]. For a generalized system, the equations of motion can be written as:

$$\mathbf{M}\ddot{\mathbf{q}}(t) + \mathbf{C}\dot{\mathbf{q}}(t) + \mathbf{K}(t)\mathbf{q}(t) = \mathbf{f}(t) \tag{2.8}$$

Where

- $\mathbf{M}$ is the mass and inertia matrix;
- $\mathbf{C}$ is the damping matrix, frequently assembled as Rayleigh damping;
- $\mathbf{K}(t)$ is the stiffness matrix, time-varying due to the varying mesh stiffness terms;
- $\mathbf{q}(t)$ is the displacement vector, including the torsional and translational coordinates of shafts, gears and bearings;
- $\mathbf{f}(t)$ is the external torque and force excitation vector;
- t is the time [s].

Where published implementations differ is in how much of the drive train they choose to resolve, some models include the whole drive train [34] while others give a more focused approach on the gear pair itself [34]. In both cases the models were calibrated against measured natural frequencies showing results within eight percent across the first eight modes over the 0–2 kHz band of interest.



(a) Model by Ren and Yuan [33]. (b) Model by Feng et al. [34].

Figure 2.6: Examples of dynamic models developed for spur gear system analysis.

The coupling between the mechanical and tribological halves of the problem passes through a single quantity. The dynamic meshing force $F_m(t)$ acting along the line of action is modelled as [33], [34]:

$$F_m(t) = k_m(t)\delta_m(t) + c_m\dot{\delta}_m(t) \tag{2.9}$$

Where

- $F_m(t)$ is the dynamic meshing force along the line of action [N];
- $k_m(t)$ is the time-varying mesh stiffness [N/m];
- c_m is the mesh damping coefficient [N·s/m], generally taken as constant;
- $\delta_m(t)$ is the relative mesh deflection along the line of action [m] (the displacement of the meshing point from the ideal theoretical point).

where the relative mesh deflection is defined by:

$$\delta_m(t) = R_{b1}\theta_1(t) - R_{b2}\theta_2(t) - e_t(t) - y_{\text{disp}}(t) \tag{2.10}$$

Where

- R_{b1}, R_{b2} are the base radii of the driving and driven gears [m];
- $\theta_1(t)$, $\theta_2(t)$ are the rotational displacements of the two gears [rad];
- $e_t(t)$ is the GTE, governed by the worn tooth profiles [m];
- $y_{\text{disp}}(t)$ is the contribution of shaft and bearing deflections along the line of action [m].

The term $e_t(t)$ is the one that carries the wear state [33], [34], [35]. Defined as the deviation of the working surface from an ideal involute, it is ideally zero for a perfect gear, which makes it a natural container both for accumulated material loss and for initial manufacturing deviations [34]. Its role within the loop is that of a prescribed displacement excitation imposed at the mesh: the wear model writes into it, and the dynamic model reads out of it, as shown in the diagram in Figure 2.7.

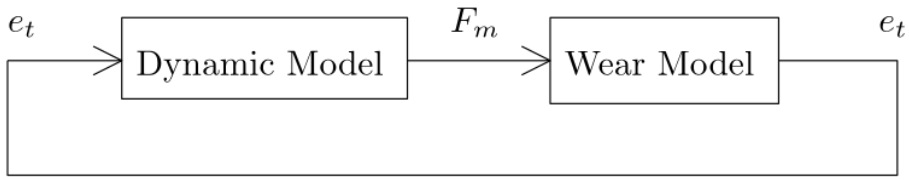


Figure 2.7: Diagram of the feedback loop used in spur gear lumped-parameter dynamic models.

2.3.2 Tribological Wear Modelling (Archard's Law)

The dynamic contact forces generated by the structural model serve as the input for the local tribological wear calculation. Although many wear formulations have been proposed, Archard's model will be the one presented in this section, due to its widespread usage in the literature. The material loss normal to the tooth flank surface is computed using the modified Archard wear formulation [12], [36], which goes as:

$$\frac{\partial h(t,\theta)}{\partial t} = K_{\text{wear}}(\theta) \cdot p(\theta,t) \cdot v(\theta,t) \tag{2.11}$$

- $h(t,\theta)$ is the worn depth normal to the flank [m];
- θ is the coordinate along the active line of action [rad];
- K_{wear} is the wear coefficient [m^2/N];
- $p(\theta,t)$ is the local contact pressure [Pa], obtained from $F_m(t)$ through Hertzian contact mechanics;
- $v(\theta,t)$ is the sliding velocity at the contact point [m/s].

The worn depth normal to the flank is the quantity taken as the GTE, that is then fed into the dynamic model, to recalculate the forces in the interface.

2.3.3 Tooth Crack Propagation

Although the present section is heavily focused on the evaluation of surface wear, it is worth noting that dynamic models are also used, for instance, in tooth crack detection, using basically the same models, but applying a different algorithm.

The structural half of the problem is shared. Wu et al. [37], Mohammed et al. [38] and Mohammed and Rantatalo [39] all employ single-stage lumped-parameter models of six to twelve degrees of freedom, with bearings as radial springs and dampers, motor and load as additional torsional discs, and a mesh element written exactly as before, $F_m = k_m(t)\delta_m + c_m\dot{\delta}_m$, with δ_m formed from base radii and angular displacements.

What differs is the point at which the damage enters the equations. Surface wear removes material from the flank, so the profile departs from the ideal involute and the GTE $e_t(t)$ is the main representation of the fault. A fatigue crack at the tooth root removes almost no material from the working surface, the flank remains involute, but the cracked tooth presents a larger deflection under load. The fault is therefore expressed entirely through the time-varying mesh stiffness $k_m(t)$, which drops during the engagement of the damaged tooth, and the term $e_t(t)$ is absent from all three crack models, which assume ideal geometry and perfect mounting [37], [38], [39]. The stiffness of a single tooth follows from treating it as a non-uniform cantilever, the bending, shear and axial compressive contributions being obtained by integration along its effective length [38], [39]:

$$\frac{1}{K_b} = \int_0^d \frac{(y\cos\alpha_1 - h\sin\alpha_1)^2}{EI_x}\,\mathrm{d}y, \qquad \frac{1}{K_s} = \int_0^d \frac{1.2\cos^2\alpha_1}{GA_x}\,\mathrm{d}y, \qquad \frac{1}{K_a} = \int_0^d \frac{\sin^2\alpha_1}{EA_x}\,\mathrm{d}y \tag{2.12}$$

Where

- K_b, K_s and K_a are the bending, shear and axial compressive stiffness of the tooth, respectively [N/m];
- d is the effective length of the equivalent cantilever [m];
- y is the distance from the load application point along the tooth [m];

- h is the distance from the load application point to the tooth centre line [m];
- α_1 is the angle of the applied load, varying with the meshing position [rad];
- I_x and A_x are the area moment of inertia [m^4] and cross-sectional area [m^2] of the section at y;
- E and G are the Young's and shear moduli [Pa].

A crack is introduced by reducing I_x and A_x over the cracked portion of the section, so that only K_b and K_s are affected while the axial and Hertzian contributions remain unchanged [37]. These act in series, giving the stiffness of one tooth as $K_t = (1/K_b + 1/K_s + 1/K_a)^{-1}$, evaluated separately for the cracked pinion tooth (K_{tp}) and its uncracked mating tooth (K_{tg}). Adding the fillet foundation deflection of each gear body and the Hertzian contact stiffness, the mesh stiffness of a single tooth pair and the equivalent stiffness of the mesh become [38]:

$$K_{m,i} = \left(\frac{1}{K_{tp}} + \frac{1}{K_{fp}} + \frac{1}{K_{tg}} + \frac{1}{K_{fg}} + \frac{1}{K_h} \right)^{-1} \qquad \text{and} \qquad K_m = \sum_{i=1}^{n} K_{m,i} \tag{2.13}$$

Where

- $K_{m,i}$ is the mesh stiffness of the i-th tooth pair in contact [N/m];
- K_{tp}, K_{tg} is the cantilever stiffness of the pinion and gear teeth [N/m];
- K_{fp}, K_{fg} is the stiffness due to fillet foundation deflection of the pinion and gear bodies [N/m];
- K_h is the Hertzian contact stiffness of the tooth pair [N/m];
- n is the number of tooth pairs simultaneously in contact, alternating between one and two for a contact ratio below two;
- K_m is the equivalent mesh stiffness entering the dynamic model [N/m].

Since a cracked tooth perturbs the signal once per revolution, the usage of statistical time-domain indicators is common in the literature (these methods will be discussed later in Section 2.4), however, purely based on the modelled physics, a further route exploits the fact that a reduction in k_m shifts the mesh-stiffness-dependent eigenfrequencies of the system. Mohammed and Rantatalo [39] compute the frequency response functions (FRF) for the maximum and minimum stiffness of each segment of the meshing cycle, then apply a short-time Fourier transform whose block sizes follow those same segments. As the crack propagates, a shift in the peaks of the FRFs can be tracked, which can be used as an indirect measurement of crack length.

The presented crack models are, however, inherently different from the previously discussed surface wear models, they are not able to model wear propagation as there is no feedback loop present or input of real data as to update the crack length, limiting their usage as wear evaluation methods.

2.4 Condition Indicators

Using full dynamic models of the gear transmission can be computationally expensive and, as shown in the previous section, is relatively limited in the modes of wear that can be reliably modelled and detected. Instead of analysing the gear transmission as a fleshed out mechanical system, we may look for changes in the signal, according to the effects showcased in Section 2.2. Using a variety of mathematical techniques, from statistical measures to simpler relationships between values extracted from the vibration data, the signal can be characterized and trended using a set of scalars, that evolve to mimic the evolution of wear in the system. Such scalars are designated condition indicators (CIs) [32], [40].

CIs are conventionally divided according to the domain in which they are computed, into time domain, frequency domain and time–frequency domain parameters [32], and that division is the one followed here.

The indicators presented below are not all computed on the same signal, the following notation is therefore adopted throughout this section [37], [40]:

- **Raw signal**, $x(n)$: the acceleration as delivered by the accelerometer, sampled uniformly in time. It contains the contribution of every component of the machine, together with background noise.
- **Time synchronous averaged signal**, $y(n)$: the raw signal resampled in the angular domain, divided into blocks one revolution of the shaft of interest long and averaged over a large number of those revolutions. It is one revolution long, uniformly sampled in shaft angle, and everything not phase-locked to that shaft has, in theory, been suppressed.
- **Regular meshing signal**, $y_{\mathrm{reg}}(n)$: reconstructed from the shaft rotational harmonics, the meshing harmonics and their first-order sidebands, that is, the components a healthy pair is expected to produce.
- **Residual signal**, $r(n)$: the TSA signal with the shaft and meshing harmonics removed, retaining the sidebands.
- **Difference signal**, $d(n)$: the residual signal with the first-order sidebands of the meshing harmonics additionally removed, so that only the irregular content survives.
- **Band-passed mesh signal**, $b(n)$: the TSA signal filtered around a chosen meshing harmonic, isolating that carrier and the modulation imposed on it from the neighbouring harmonics.
- **Envelope**, $s(n)$: the amplitude modulation extracted from $b(n)$ by demodulation.

Beyond the averaging itself, each of these steps removes a component that a healthy gear also produces, so the same statistic applied further down the chain becomes progressively more sensitive to damage, at the cost of becoming noisier and more dependent on the quality of the healthy reference used to build $y_{\mathrm{reg}}(n)$.

2.4.1 Time-Domain Indicators

2.4.1.1 Raw and Synchronously Averaged Signal

Root Mean Square (RMS). The RMS measures the energy content of a record,

$$\mathrm{RMS} = \sqrt{\frac{1}{N}\sum_{n=1}^{N} x(n)^2}, \tag{2.14}$$

and coincides with the standard deviation of the record when its mean is zero, as is the case for an AC-coupled acceleration signal. The definition applies unchanged to any of the signals listed above, and it is used on most of them: on the raw signal it gives the overall vibration level, on the TSA signal the level of the content synchronous with the shaft of interest, and on the residual and difference signals it is used to build more complex indicators. Being an average over the whole record, the RMS responds to changes that persist over the full signal and dilutes those confined to a small fraction of it: a single damaged tooth adds energy over a short interval which is averaged against the remaining, healthy fraction [31], [37]. It is dimensional and varies with load, speed and sensor location, so it is only interpretable when trended under repeatable operating conditions.

Maximum Peak Acceleration. The peak value is the largest absolute excursion of the record,

$$x_{\mathrm{pk}} = \max_{n} \big|x(n)\big|, \tag{2.15}$$

and is often normalised by the RMS to give the crest factor, $\mathrm{CF} = x_{\mathrm{pk}}/\mathrm{RMS}$, which sits close to 3 for a signal free of impulsive content and rises as isolated impacts appear [31], [39]. It is normally evaluated on the raw signal, since averaging reduces exactly the isolated excursions it is meant to capture, although the same definition may be applied to the residual signal. The rationale for tracking the peak rather than the RMS is that a localised defect produces a large amplitude over a very short interval, which the averaging of Equation (2.14) suppresses.

This statistic also has the advantage of being comparable to standardized values. ISO 20816-9 [41] assesses gear units through housing vibration true peak acceleration, and assigns each unit an acceleration rating (AR) according to its type, so that a quiet precision unit is not held to the same limit as a straight-cut reduction gear. Within each rating, four evaluation zones are defined: zone A corresponds to newly commissioned machines, zone B to vibration acceptable for unrestricted long-term operation, zone C to vibration considered unsatisfactory for continuous operation, and zone D to levels severe enough to cause damage. The boundaries between them are reproduced in Table 2.2 for the two ratings relevant to general-purpose and straight-cut spur reduction units.

Kurtosis. Kurtosis is the fourth central moment of the record normalised by the square of its variance,

Table 2.2: Boundary values of housing vibration true peak acceleration for two acceleration ratings (adapted from ISO 20816-9). [41]

	AR 80		**AR 125**	
Zone boundary	[m/s^2]	[g]	[m/s^2]	[g]
A/B	50.0	5.1	80.0	8.1
B/C	80.0	8.1	125.0	12.7
C/D	125.0	12.7	200.0	20.4

$$\text{Kurt} = \frac{\frac{1}{N}\sum_{n=1}^{N}\left(x(n)-\bar{x}\right)^4}{\left[\frac{1}{N}\sum_{n=1}^{N}\left(x(n)-\bar{x}\right)^2\right]^2}, \tag{2.16}$$

and quantifies the peakedness of the amplitude distribution, taking a value of approximately 3 for a Gaussian signal and increasing as the distribution develops heavier tails. It is dimensionless, requires no baseline, and is reported as one of the most robust indicators for localised gear and bearing faults [37], [39]. Equation (2.16) is written for the raw signal but kurtosis is applied throughout this section to other signals: evaluated on the residual signal it gains sensitivity to anomalous vibration in the shaft's revolution, on the difference signal it becomes FM4, and on the envelope it becomes the envelope kurtosis, both of which are described in the following section.

Two limitations should be noted. Kurtosis is not a monotonic function of damage severity: as a defect grows from an isolated occurrence towards a distributed condition, the impacts become more numerous and more closely spaced, the energy they contribute begins to dominate the RMS in the denominator of Equation (2.16), and the indicator falls back towards its "healthy" value even though the component is in a worse state [31]. Nor is it a direct measure of severity at a fixed damage level, since its value also depends on the spacing between the fault impulses and on the damping of the excited resonances, for instance, Randall states that doubling the rotational speed of a machine roughly halves the kurtosis obtained for the same fault [31].

2.4.1.2 Residual and Difference Signals

FM4. Proposed by Stewart in 1977, FM4 was designed to detect faults confined to a limited number of teeth and is defined as the normalised kurtosis of the difference signal [32], [40]:

$$\text{FM4} = \frac{N\sum_{n=1}^{N}\left(d(n)-\bar{d}\right)^4}{\left[\sum_{n=1}^{N}\left(d(n)-\bar{d}\right)^2\right]^2}, \tag{2.17}$$

which is dimensionless and, like kurtosis, has a nominal value of 3 when $d(n)$ is purely Gaussian. The reasoning behind the parameter lies entirely in how the difference signal is constructed, any peak surviving in $d(n)$ is attributable to a tooth that behaves differently from its neighbours. It is the origin of a large family of derived parameters, obtained either by raising the order of the moment, as in M6A and M8A, or by replacing the instantaneous variance in the denominator with an average including previous records, as in NA4, or by locking that average once it exceeds a statistical limit, as in the starred variants NA4* and FM4* [40].

Energy Ratio (ER). The ER compares the energy held in the irregular content of the signal with that held in the regular meshing components, and is obtained by calculating the ratio between their RMS values [32], [40]:

$$\mathrm{ER} = \frac{\mathrm{RMS}_d}{\mathrm{RMS}_{y_{\mathrm{reg}}}}. \tag{2.18}$$

It was conceived for heavy uniform wear, on the premise that as the tooth profiles degrade the deterministic meshing pattern loses coherence and energy is transferred from the regular signal to the difference signal, so that the numerator rises while the denominator falls. That double sensitivity is also the source of its main weakness: Hu et al. [19] report that an increase in ER may originate in a decrease of the meshing harmonic amplitudes rather than in any growth of the residual content, so that the indicator cannot by itself distinguish the two situations.

2.4.1.3 Band-Passed Mesh Signal

Envelope Kurtosis. Amplitude demodulation isolates the modulating function from its carrier, so that the statistics of the modulation can be examined without interference from the meshing vibration itself [29]. The envelope of the band-passed mesh signal is the modulus of the corresponding analytic signal,

$$s(n) = \left| b(n) + \mathrm{j}\,\mathscr{H}\{b(n)\} \right|, \tag{2.19}$$

where $\mathscr{H}\{\cdot\}$ denotes the Hilbert transform, and the envelope kurtosis is Equation (2.16) evaluated on $s(n)$. The underlying reasoning is that damage confined to a few teeth produces transient load fluctuations that differ from those generated by healthy teeth, and that these appear as isolated peaks in the envelope even when they are not visible in the raw waveform [40]. The parameter NB4 is the standard formalisation of this idea, differing only in that the fourth moment is normalised by the run-time averaged variance of the envelope rather than by the instantaneous one [40]. In gearboxes the band is normally placed around a meshing harmonic; in bearing diagnostics it is placed around a housing resonance excited by the fault impacts [31]. The choice of that band is the critical parameter of the method, and is addressed by the spectral kurtosis.

2.4.2 Frequency-Domain Indicators

Envelope Amplitude. Where the envelope kurtosis characterises the shape of the modulation, the envelope amplitude characterises its strength at a known rate. Taking $S(f)$ as the spectrum of the

envelope signal of equation (2.19), the indicator is the amplitude of that spectrum at a characteristic frequency f_c,

$$\mathrm{EA}(f_c) = \left|S(f_c)\right|, \tag{2.20}$$

with f_c chosen from the kinematics of the machine: the rotational frequency of the gear under study for a tooth defect, or one of the bearing characteristic frequencies for a rolling element defect. Simpler variants take the peak or the RMS of the envelope waveform $s(n)$ instead of a specific spectral line.

Sideband Ratio (SBR). The average deviation of the working surface from the ideal involute contributes to the meshing harmonics themselves, whereas differences between individual teeth appear as modulation of those harmonics [19]. The SBR quantifies that modulation for each harmonic individually. Taking the amplitude- and phase-modulated model of the TSA signal introduced in Section 2.2.1, the k-th meshing harmonic may be band-pass filtered and its carrier removed, leaving a signal $r_k(n)$ that contains only the sidebands of that harmonic. Denoting by X_k the deterministic amplitude of the carrier, the SBR is the normalised power of the modulation [19]:

$$\mathrm{SBR}_k = \frac{\left[\mathrm{RMS}_{r_k}\right]^2}{X_k^2}, \qquad k = 1,2,\ldots,K. \tag{2.21}$$

The SBR may thus be read as an envelope power referred to its own carrier, which makes it a dimensionless quantity and largely removes the influence of the overall vibration level, so that what it reports is the relative weight of the tooth-to-tooth differences against the average working surface deviation represented by that harmonic

Averaged Logarithmic Ratio (ALR). A single SBR describes only part of the transmission behaviour, so Hu et al. [19] assembled the ratios obtained from all significant meshing harmonics into a gear state vector, $\mathbf{SBR}_i = (\mathrm{SBR}_{i,1}, \mathrm{SBR}_{i,2}, \ldots, \mathrm{SBR}_{i,K})$, evaluated at measurement time i, and measured how far that vector has drifted from a reference state $\mathbf{SBR}_0$. The ALR is defined as

$$\mathrm{ALR}_{i,0} = \frac{1}{K}\sum_{k=1}^{K}\left|\ln\frac{\mathrm{SBR}_{i,k}}{\mathrm{SBR}_{0,k}}\right|, \tag{2.22}$$

and a moving version, obtained by replacing the fixed reference with the preceding measurement,

$$\mathrm{mALR}_i = \frac{1}{K}\sum_{k=1}^{K}\left|\ln\frac{\mathrm{SBR}_{i,k}}{\mathrm{SBR}_{i-1,k}}\right|. \tag{2.23}$$

The absolute value is required because wear does not drive every harmonic in the same direction, so that a plain average would allow increases in some SBRs to cancel decreases in others, while the logarithm prevents a large change in a single harmonic from dominating the mean. The construction satisfies the axioms of a distance, so that $\mathrm{ALR}_{i,j}$ is properly read as a generalised distance between two gear states. The two versions carry different information: referred to a fixed baseline, ALR accumulates the total deviation from the reference condition, whereas mALR, referred to the

previous measurement, reports the rate at which the state is changing. Since the transmission error is strongly load dependent, both require that the vibration be always measured at the same load [19].

2.4.3 Time–Frequency Domain Indicators

Spectral Kurtosis (SK). Every parameter discussed so far collapses the record into a single number, so a transient confined to a narrow frequency band is averaged together with the broadband content surrounding it. The SK, introduced by Dwyer and formalised by Antoni [42], restricts the signal to one narrow band at a time and evaluates a kurtosis on the envelope of each, which reports not only that impulsive components are present but also where in frequency they occur. It is the same operation as the envelope kurtosis of Section 2.4.1.3, swept across all bands instead of applied to one. Writing $H(n,f)$ for the complex envelope of the process at frequency f in the Wold–Cramér decomposition, and $\langle\cdot\rangle$ for the time average, the SK is the normalised fourth-order spectral cumulant

$$K_x(f) = \frac{\left\langle |H(n,f)|^4 \right\rangle}{\left\langle |H(n,f)|^2 \right\rangle^2} - 2, \tag{2.24}$$

where the constant 2 is used instead 3, used often with Equation (2.16), to refer to excess kurtosis, because the moments are taken of the magnitude of a complex envelope rather than of a real signal. Where the power spectral density gives the time average of the energy at each frequency, the SK gives its time dispersion [42]. It is constant with frequency for a stationary process, zero for a stationary Gaussian process, and in additive stationary noise it degrades as

$$K_{x+b}(f) = \frac{K_x(f)}{\left[1+\rho(f)\right]^2}, \tag{2.25}$$

where $\rho(f)$ is the noise-to-signal ratio at that frequency, so bands in which the fault dominates keep a high value and bands in which it is buried do not.

Equation (2.24) depends on the frequency resolution used to estimate it, since a transient is characterised by its bandwidth as well as by its centre frequency. Antoni therefore generalised the SK to a function of the frequency–frequency-resolution dyad $(f,\Delta f)$, whose representation is the kurtogram, and gave a fast algorithm of complexity $O(N\log N)$ [42]. This serves two purposes. As an indicator, the kurtosis of the signal filtered in the optimal band has been shown to track fault development, in documented cases following accumulated oil wear debris and measured spall size [31]. As a pre-processing step, the optimal dyad supplies the demodulation band required by the envelope indicators of Section 2.4.1.3. As with ordinary kurtosis, the value is not a direct measure of severity, since it responds to the spacing of the impulses and to the damping of the excited resonance as much as to the size of the fault [31].

Table 2.3 collects the indicators described above, together with the signal each is computed on, the damage they were designed to detect, and their principal limitation.

Table 2.3: Overview of the CIs considered.

Indicator	**Domain**	**Base signal**	**Designed for**	**Main limitation**
RMS	Time	Any; usually $x(n)$ or $y(n)$	Overall energy of the vibration	Averages out short transients; dimensional and load dependent
Max peak acceleration	Time	$x(n)$ (true peak)	Isolated impacts; ISO zone assessment	Set by a single sample; unstable and record-length dependent
Kurtosis	Time	$x(n)$, $y(n)$ or $r(n)$	Impulsive, localised faults	Non-monotonic with severity; scales with shaft speed
FM4	Time	$d(n)$	Damage confined to a few teeth	Returns to nominal once the damage becomes distributed
ER	Time	$d(n)$ and $y_{\mathrm{reg}}(n)$	Heavy uniform wear	Ambiguous, since numerator and denominator both vary
Envelope kurtosis	Time	$s(n)$	Transient load fluctuations from damaged teeth	Sensitive to the choice of demodulation band
Envelope amplitude	Frequency	$S(f)$ at f_c	Modulation strength at a known rate	Requires f_c to be known; dimensional
SBR	Frequency	$y(n)$, per meshing harmonic	Depth of modulation of each harmonic	A single harmonic describes only part of the gear state
ALR / mALR	Frequency	Gear state vector of SBRs	Cumulative deviation from a reference and rate of change	Requires a reliable reference and a constant load
SK	Time–frequency	$x(n)$, via STFT or filter bank	Transients buried in stationary noise; band selection	Not a direct severity measure; speed dependent

2.5 Machine Learning Applications

The CIs of Section 2.4 share a common structure: a human chooses the statistic, the signal it is computed on and the threshold at which an alarm is raised. Machine learning approaches displace that choice, replacing the hand-designed indicator and threshold with a mapping learned from data. The section that follows is not intended as a review of the field, which is large and moves quickly, but as a brief overview of the routes that have been taken and of what they require from an experimental setup such as the one proposed here.

2.5.1 Learning from Extracted Features

The first and most classical route keeps the CIs and uses them as the input to the learning algorithm, which is then asked only to find the rule that best separates the health states, rather than to interpret the raw signal. The reasoning is that no single indicator separates the states cleanly, but a combination of them may.

Because several indicators are usually computed on several measurement channels, the description of each acquisition quickly becomes a long list of numbers, many of which carry overlapping information. It is therefore common to condense the list first, replacing the original indicators by a smaller number of combinations that account for most of the variation between acquisitions, before any classification is attempted. Daga et al. [13] follow this sequence on the bearing dataset described in Section 2.1.2, computing a set of time-domain statistics on each channel, condensing them by principal component analysis, and training a linear classifier to draw the boundary between the known damage states.

The same work also illustrates the alternative formulation available at this stage. Instead of learning to recognise each fault, the method can be asked only to characterise how the measurements are distributed when the machine is healthy, and to flag any later acquisition that falls too far outside that distribution. This is known as novelty detection, and its practical advantage is that it requires labelled data only for the healthy condition, which in an industrial setting is usually the only condition available in quantity. [43]

2.5.2 Learning from the Signal

The second route removes the feature extraction stage altogether and presents the signal directly to a neural network, on the premise that the network will learn a more informative description than the one specified by the indicators. The signal is either fed in as a time series, using architectures designed to handle sequences, or first converted into a time–frequency image such as a spectrogram, which can then be treated with the same networks used for image recognition. The second option is attractive because it allows a network already trained on a large collection of generic images to be reused, with only its final layers retrained on the vibration data, which substantially reduces the number of labelled examples needed.

Najeh et al. [16] compare the two routes on the same problem, estimating the wear of a railway switch and crossing from accelerometers housed inside the point machine. In the first, time-domain features are computed on successive windows of the vibration record and passed to a network designed for sequential data; in the second, the records are converted to spectrogram images and used to retrain an existing image-recognition network.

Architectures of these two families dominate the recent literature, and are applied both to classification, where the task is to assign a discrete health state, and to regression, where the target is a continuous quantity such as wear depth or remaining useful life. Much of the current effort, however, is directed less at accuracy than at the practical obstacles that follow it. Pan et al. [44] address two of these: the computational cost of large networks, which they reduce by training a smaller network to reproduce the behaviour of a larger one and by removing the parts of it that contribute least, so that the result can run on hardware installed at the machine itself; and the loss of performance when a model trained on one machine or one operating condition is applied to another, which is treated as a problem of adapting an existing model to a new setting rather than of training it again from the beginning.

2.5.3 Limitations and Relation to the Present Work

Three limitations are worth stating, as they bear directly on the role of a physical demonstrator.

The first is the requirement for data. A model trained on labelled examples needs those examples for every state it is expected to recognise, and run-to-failure campaigns of the kind reviewed in Section 2.1.2 are slow and expensive to produce. This is the main reason why seeded faults are so common in the literature, and why the resulting models are trained on a few discrete severity levels rather than on a continuum.

The second is that the learned mapping is tied to the machine and to the operating conditions on which it was trained. A change of speed, load or even of lubricant shifts the measured quantities, and the model may interpret that shift as damage. Daga et al. [13] report exactly this effect, finding the influence of the operating conditions on the measurements to be comparable to that of the damage itself, and the alarm rates to become acceptable only once each condition was analysed against its own healthy reference.

The third is interpretability. A model that assigns the correct health state does not thereby explain which physical mechanism produced it, which limits its usefulness for diagnosis as opposed to detection, and makes validation difficult in the absence of an independent measurement of the wear.

These limitations are complementary to the objectives of this work rather than an argument against the approach. A physical demonstrator that produces progressive, naturally developed wear alongside an independent measurement of its severity generates precisely the kind of labelled data that these methods require and that is currently scarce. Machine learning is therefore not pursued further in this dissertation, but the proposed rig is intended to leave that route open for future work.

Chapter 3

Demonstrator Design

In this chapter, the practical approach taken in this thesis is defined, starting with the definition of design requirements for the test rig, and then the design choices are presented for each developed constructive solution or chosen components.

3.1 Design Requirements

The design of the test rig is governed by two sets of requirements: the constraints under which it is built, and the subsystems it must incorporate.

The following constraints apply to the design as a whole:

- **Reduced scale:** the demonstrator must be compact and portable, which limits the admissible power, torque and overall envelope of every subsystem described below;
- **Cost-efficiency:** the rig is intended to be worn, dismantled and reassembled repeatedly over the course of testing. A modular architecture is therefore adopted, together with inexpensive and rapid manufacturing techniques, namely Fused Deposition Modelling and showing preference for bought components over own fabrication.

The rig is composed of the following subsystems:

- **Driving unit:** although the gears are the components of interest, the scale constraint and the range of gear types available make the driving unit the first element to be defined, since its power rating bounds the remainder of the design. An electric motor was selected according to its power rating, its behaviour under constant load and its commercial availability;
- **Loading element:** wear develops considerably faster under load, so a system to impose a controlled torque is dimensioned within the limits established in Section 3.2. Hu et al. [19] recommend applying a torque above the rated capacity of the gear pair in order to shorten test duration, which would otherwise extend to weeks or months of acquisition. This requirement subsequently conditions gear selection;

- **Gear pair:** a set of gear pairs is selected within the torque limits imposed by the driving unit and the loading element,varying in geometry (module, number of teeth, face width) and in material;
- **Drivetrain:** a mechanical transmission connects the driving unit to the loading element through the selected gear pair. It comprises the shafts, couplings and a load-adjustment mechanism that allows tests to be performed at different torque levels;
- **Structural components:** the bearings, supports and frame on which the preceding subsystems are mounted, ensuring the stability and transportability of the assembly.

3.2 Driving unit

The driving unit is a fundamental component of the test rig, as it provides the mechanical energy required to rotate the transmission under study. In the context of vibration-based condition monitoring, the selection of the motor is governed by the need for a stable input velocity and the minimization of noise. In this section an overview of available motors is presented including: AC motors and various types of DC motors such as Brushed, Brushless and Stepper motors, followed by the selection process.

Alternating Current (AC) induction motors are the most common driving units found in industrial gear transmissions. Their primary advantage for experimental research is their ability to maintain a relatively constant speed under varying load conditions. They are highly durable, cost-effective, and require minimal maintenance, making them suitable for long-duration wear tests. However, for a laboratory-scale table-top demonstrator, induction motors present significant integration challenges. They are generally larger and heavier than DC alternatives of equivalent power, leading to a much lower torque-to-weight ratio. Additionally, the requirement for a high-voltage AC power source limits the portability and safety profile of a compact laboratory setup.

Direct Current (DC) motors are frequently utilized in high-precision and small-scale mechanical assemblies due to their high power density and ease of control. For experimental rigs focused on automated parameter control, DC motors are often preferred because their speed and torque can be easily modulated via low-voltage scripts and microcontrollers. Within this category, three distinct technologies are commonly considered:

- **Brushed DC Motors:** The simplest form of DC drive, requiring no external commutation electronics, since current is switched between armature coils by brushes bearing on a rotating commutator. The switching produces torque ripple at the segment passing frequency, to which cogging adds further components; both are harmonics of the shaft speed, overlap the lower meshing orders and, being synchronous with the rotation, are not removed by time synchronous averaging. The brush contact adds impulsive events and sparking, repeating at that same rate and modulated once per revolution, which is the signature the envelope indicators are intended to recover from the mesh. The brushes also wear, introducing a secondary degradation variable into the system.

- **Brushless DC (BLDC) Motors:** BLDC motors are modern alternatives that eliminate the maintenance issues of brushes. They offer the highest efficiency and torque-to-volume ratio, making them ideal for compact demonstrators. A technical disadvantage in vibration research is the "torque ripple" caused by the electronic commutation of the phases. This can manifest as periodic fluctuations in the shaft speed.
- **Stepper Motors:** Steppers allow for open-loop position and speed control without the need for encoders. While they are useful for low-speed applications, they are generally avoided in high-fidelity vibration studies. The "stepping" nature of their movement creates significant inherent vibration and resonance at specific frequencies. This discrete movement pattern introduces harmonic noise across the vibration spectrum, which typically makes the isolation of gear-mesh sidebands extremely difficult.

Given the specific constraints of a table-top rig, the choice of a DC unit generally prioritizes the reduction of the system's footprint and the simplification of the control interface, provided the signal processing pipeline can account for the specific noise profile of the chosen motor. The motor chosen was the RS PRO Brushless DC Motor (RS Stock No.: 536-6030), since it was already available. Its main operating characteristics are presented in Table 3.1.

Table 3.1: Operating characteristics of the BLDC motor.

Rated Torque	Max. Torque	Rated Speed	Voltage	Current
0.25 Nm	0.75 Nm	4000 rpm	24 V	20 A

It should be noted that, at the rated operating conditions, the selected motor does output a relatively small steady state torque, making it potentially difficult to find suitable gears to induce wear in, so, due to its high nominal speed, a reduction stage was therefore employed to achieve a larger torque.

3.3 Loading elements

Having set a reference value for torque, a system to impose the load on the system had to be designed. As stated earlier in this paper, the test rig should have a mechanism that allows for the performance of tests at various load values and, for each test, the torque imposed by the loading element should be higher than the gear's surface strength limit. In this section an exposition is made on commonly used loading elements such as gear pump systems, Eddy Current Brakes and friction brakes, followed by the definition of the constructive solution to employ.

3.3.1 Gear Pump System

Similarly to the test rig presented by Hu et al.[19], a pump system was considered as a possible load-imposing element for the test rig. Pump systems come as a compelling option for a number

of reasons: they do not require external power sources to operate (contrary to electromagnetically-actuated friction brakes, another widely used alternative, which is discussed in Section 3.3.3) and the load imposed is relatively easy to vary through a simple valve. The proposed layout is presented in Figure 3.1.

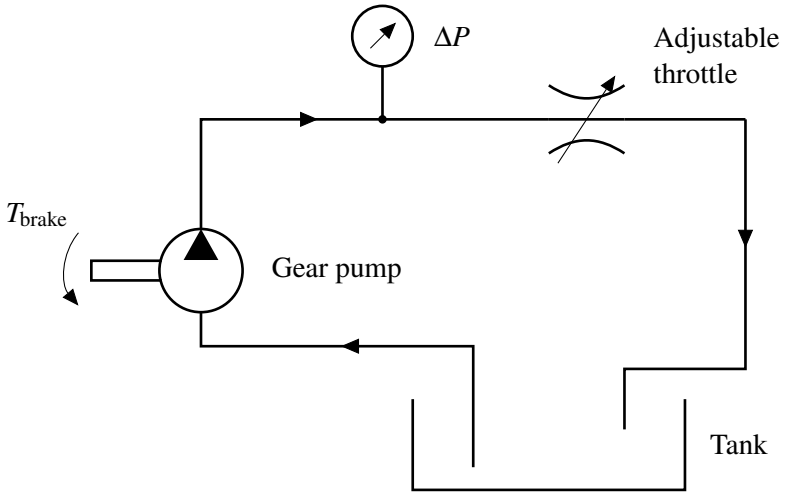


Figure 3.1: Hydraulic circuit of the loading element. The gear pump absorbs the braking torque T_{brake}, and the load is set by the adjustable throttle, across which the pressure drop ΔP is measured.

Various types of mechanical pumps are available on the market for this application, for preliminary design considerations, an external gear pump unit is considered, although they present lower volumetric efficiency when compared to vane pumps or piston pumps, for instance, its simple and compact constructive solution, availability at lower displacement volumes and robustness make it acceptable for use and a more cost-effective option. [45]

The governing equation behind the design of a pump brake system comes as [45]:

$$T = \frac{V_d \cdot \Delta P}{2\pi \cdot \eta_0} \tag{3.1}$$

Where,

- T is the input torque, in [N m];
- V_d is the pump's rated volumetric displacement, in [$\text{m}^3\,\text{rev}^{-1}$];
- η_0 is the pump's overall efficiency; for external gear pumps, $0.8 < \eta_0 < 0.9$.

In Section 3.2 it is established that the gear pump should be able to impose a loading torque ranging from 0.25 N m to an upper limit value yet to be determined, so as a general feasibility check, a resistant torque of up to 1.5 N m was defined as the target, calculating for standard volumetric displacement values available (Group 1 pumps) the results shown in Table 3.2 were obtained.

All pressure values are within ordinary rated limits for the necessary components and are low enough that the pressurized fluid does not pose a significant safety hazard. It should be noted that

Table 3.2: Required pressure differential for target torque range ($T_{min} = 0.25$ Nm, $T_{max} = 1.5$ Nm, $\eta_0 = 0.8$)

V_d [cc]	ΔP_{min} [bar]	ΔP_{max} [bar]
1.1	11.42	68.54
2.7	4.65	27.92
5.0	2.51	15.08
8.0	1.57	9.42

some manufacturers indicate a minimum operating speed for the pumps (for instance, a minimum speed of 1000 rpm for a 1.1 cc pump [46]).

3.3.2 Eddy Current Brakes

Using an Eddy Current Brake (ECB) as a loading mechanism in rotating motion test rigs is also quite common; Loedolff [47] used an ECB as the loading mechanism for a bicycle drive train test rig, and even at NASA research facilities, ECBs have been used as loading mechanisms since 1991 [48].

The working principle behind ECBs relies on Faraday's Law of Induction and Lenz's Law. When a conductive material, such as aluminium or copper, moves through a stationary magnetic field, the change in magnetic flux induces circular loops of electrical current, known as eddy currents, within the conductor. According to Lenz's Law, these induced currents create their own magnetic field that opposes the original change in flux. This interaction generates a Lorentz force that acts in the opposite direction of the motion. [49]

For this specific application, the ECB is an interesting loading solution for several reasons:

- **Frictionless braking:** Since there is no mechanical friction, the brake does not generate high-frequency acoustic or vibratory noise. This is convenient for this study, as it ensures the vibration signals captured by the accelerometers are purely a result of the gear meshing dynamics and wear, rather than brake-induced noise.
- **Thermal Stability:** the ECB's thermal performance is predictable and changes only slightly with the temperature-dependent resistivity of the disc, these problems can be avoided with a simple dedicated cooling system.
- **Simplicity:** The system requires no external hydraulics or power sources, making it suitable for a laboratory-scale demonstrator.

The brake assembly (see Figure 3.2) usually consists of an aluminium disc rigidly attached to the output shaft of the gear transmission. The magnetic field is provided by a set of Neodymium (NdFeB) permanent magnets positioned on either side of the disc.

The design and torque prediction of ECBs may be governed by the analytical model presented by Schieber [51], which yields the following equation:

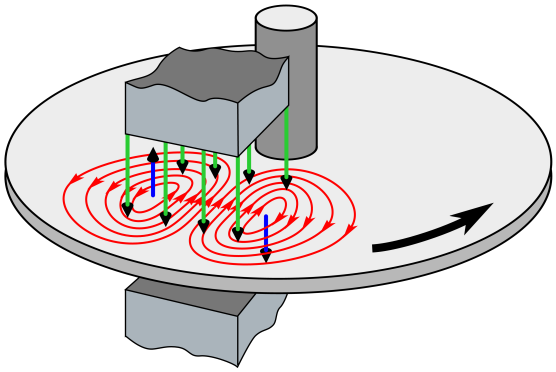


Figure 3.2: Sketch of rotor-stator interaction in an ECB. [50]

$$T = \frac{1}{2}\sigma\delta\omega R^2\pi m^2 B_z^2\left[1 - \frac{(R/a)^2}{(1-(m/a)^2)}\right] \tag{3.2}$$

Where,

- σ is the disc's material electrical conductivity, in $[S/m]$.
- δ is the disc's thickness, in $[m]$.
- ω is the disc's angular speed, in $[rad/s]$
- $R^2\pi$ corresponds to the magnet's pole area, in $[m^2]$, considering circular section magnet.
- m is the distance from the disc's axis to the magnetic pole's centre, in $[m]$.
- B_z is the magnetic flux going through the disc, in $[Wb/m^2]$.
- a is the Aluminium disc's radius, in $[m]$.

To ensure operation within the brake's linear region we may use Wouterse's model to calculate the critical speed (Equation 3.3), the speed at which the torque reaches its maximum and beyond which the brake behaves non-linearly.

$$\omega_k = \frac{2}{\mu_0 R}\sqrt{\frac{1}{c\xi}}\left(\frac{1}{\delta\sigma}\right)\sqrt{\frac{x}{2R}} \tag{3.3}$$

Where,

- μ_0 is the permeability of vacuum (physical constant, $\mu_0 = 4\pi\cdot 10^{-7}$ [H/m]);
- $cand\xi$ are geometric parameters, their product is taken as unity, conservatively;
- x is the air gap between pole faces, including the disc thickness, in [m].

Table 3.3: Geometric and physical parameters of the ECB prototype.

δ	a	R	σ	m	T
5.0 mm	65.0 mm	12.0 mm	35.0 MS/m	[40; 53] mm	[1.045 ; 1.744] Nm

Given the components available on the market, an ECB was designed with the characteristics described in Table 3.3, showcasing the feasibility of the solution, having the capability of imposing the desired range of loading torque, with design-wise sound dimensions.

The magnetic flux, B_z, considered when calculating the loading torque was of 0.5 T. A simulation of the magnetic flux between the two poles was performed using the FEMM software, the material properties and problem parameters defined are presented in Table 3.4, the plot of the simulated results is shown in Figure 3.3. The designed prototype yielded a critical speed of 951.13 rad/s ($n_c \approx 9081$ rpm) which is largely above the operating speed employed.

Table 3.4: Definition of the magnetostatic finite element model and material properties assigned to each region (FEMM 4.2 [52]).

(a) Model definition				
Problem type	2-D planar, magnetostatic			
Depth	12 mm			
Outer boundary[a]	Asymptotic (mixed), $c_0 = n/(\mu_0 r_0)$, $c_1 = 0$, $n = 1$			
Mesh	4891 nodes, 9405 elements, automatically generated			
(b) Material properties				
Region	**Material**	μ_r	H_c [A m^{-1}]	σ [MS m^{-1}]
Surrounding medium	Air	1.00	–	–
Brake disc	Aluminium 6061-T6	1.00	–	24.59
Permanent magnets	NdFeB, grade N48	1.05	1 014 538	0.667

[a] The coefficients of the mixed boundary condition were determined according to the software's manual [52, Appendix A.3.2] so that the circular outer boundary approximates an unbounded solution domain.

3.3.3 Friction Brakes

Friction-based loading mechanisms represent a traditional and widely documented approach to generating resistive torque in mechanical testing. These systems rely on the physical contact between stationary pads and a rotating element, such as a disc or drum, to dissipate kinetic energy as heat. Given the requirements of a lab-scale gear transmission demonstrator, several friction-based technologies present themselves as viable candidates:

- **Electromagnetic Friction Brakes:** These units utilize an electromagnetic coil to actuate an armature that engages the friction surfaces. They are highly valued in industrial automation for their rapid response times and the ability to be easily integrated into digital control scripts, allowing for variable load profiles via Pulse Width Modulation. However, they

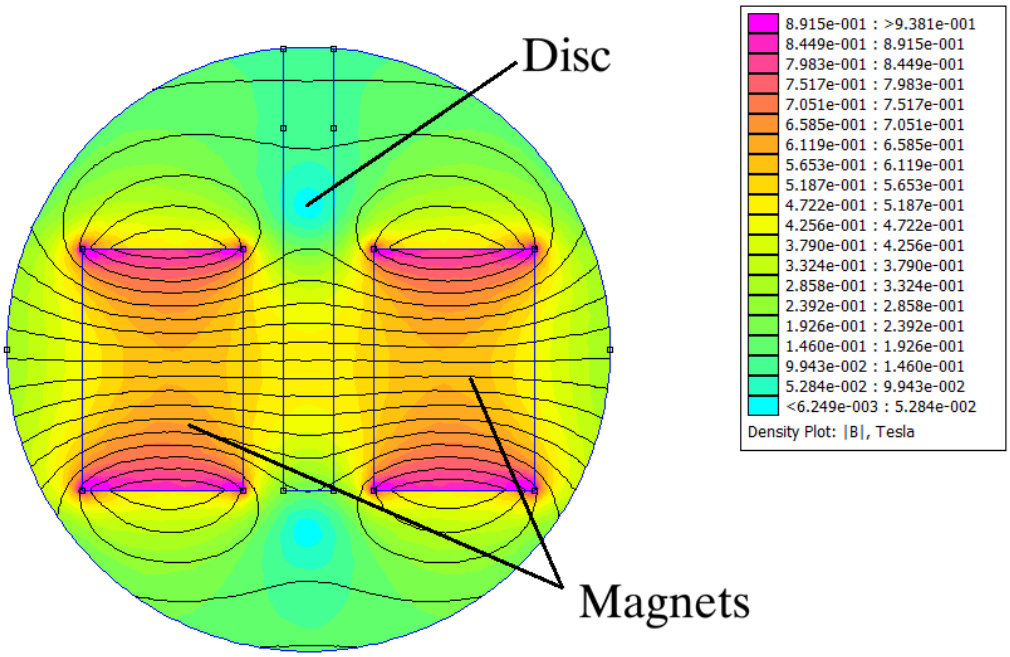


Figure 3.3: Magnetic flux field in the ECB assembly, simulated in FEMM.

are susceptible to significant thermal sensitivity; as the internal windings heat up during operation, the electrical resistance increases, leading to a drop in current and a subsequent fade in braking torque.

- **Magnetic Powder Brakes:** Frequently cited in gear research, these brakes consist of two concentric rotors with a gap between them, filled with fine magnetic powder. When a magnetic field is applied, the powder forms "chains" that create a shear-based resistive torque. Their primary advantage is that the torque is almost entirely independent of the rotational speed, providing a smooth operation at low velocities. However, these units are generally characterized by a high weight-to-torque ratio and higher price. Furthermore, the requirement for a constant external power supply and the potential for the magnetic particles to settle or degrade over long cycles of time present challenges for maintaining a stable, portable table-top demonstrator.

- **Pneumatic and Hydraulic Brakes:** These systems utilize fluid pressure (either compressed air or hydraulic oil) to provide the normal force on the friction surfaces. These are capable of generating the highest torque densities out of any friction-based system, making them ideal for heavy industrial power trains. Despite their robustness, they require significant auxiliary infrastructure, including compressors, pumps, and high-pressure lines. From a vibration monitoring perspective, this infrastructure is problematic as it introduces acoustic noise into the system frame. Such interference can easily contaminate the high-frequency vibratory signatures from the gears.

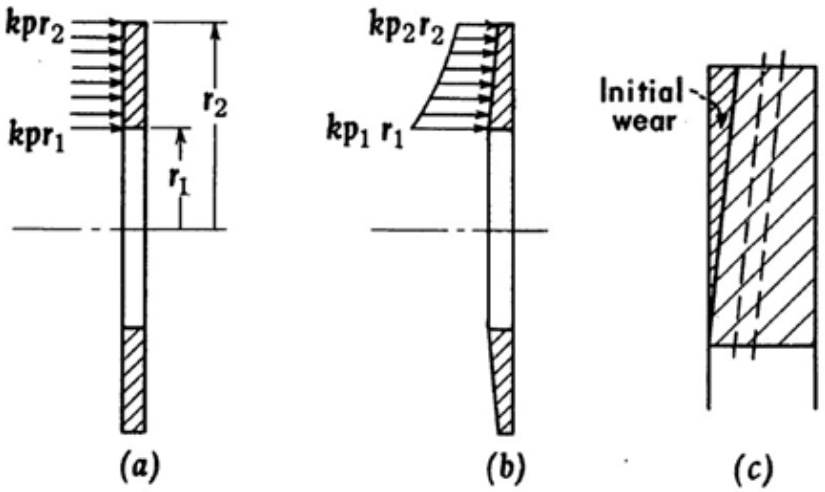


Figure 3.4: Typical wear pattern in friction disc surface's [53].

- **Spring-applied Friction Brakes:** This configuration utilizes the elastic potential energy of calibrated springs to maintain the normal force on the friction surfaces. The primary benefit of this approach is the passive nature of the load, meaning once the spring compression is manually set, the system does not require an external power source to provide a load (only to lift it). A notable characteristic of these systems is their irregular wear pattern, due to the difference in sliding speeds across the disc's radius, the disc suffers from different wear rates in an initial running-in stage (Figure 3.4) until the surface wear caused by the faster sliding speed results in a pressure redistribution, compensating the wear gradient. This behaviour can cause fluctuation in braking torque in the initial wear-in stage. While the load is not perfectly constant (the force will decrease slightly according to the spring's stiffness coefficient (k) as it expands) it retains a predictable macro load profile.

3.3.4 Selection

The magnetic powder brakes and fluid based options (both friction based and the gear pump brake) were excluded due to sizing incompatibility, the resulting assemblies were deemed to be too bulky to fit the scale of the demonstrator. The electromagnetically actuated options were ruled out due to the necessity of having the brake imposing the load during hours-long tests, inducing heat-related problems.

Designing an ECB was also ruled out due to the sensitivity of the design, the torque would not be easily regulable and deflection in the magnet supports could induce a "feedback" loop, increasing the magnetic force between the poles and damaging the brake structure, making it a less robust option for the test rig.

In order to vary the load imposed on the system a variable reduction stage was employed. This mechanism also has the function of isolating possible vibration noise caused by the brake.

All options considered, the chosen method to impose a load on the system was a spring applied friction brake, the model chosen was the M.1703.2221 Electromagnetic Brake Power On, by Warner Electric Europe, it is a Friction Spring-applied Brake with electromagnetic release, its main rated characteristics are shown in Table 3.5.

Table 3.5: M.1703.2221 rated operating characteristics.

Torque	Voltage	Current	Diameter
0.79 Nm	24 V	0.247 A	62 mm

3.4 Gear Pair

Taking into account the driving unit and loading component employed, a suitable gear pair was chosen. As stated in Section 3.1 the loading torque should be larger than the gear's rated allowable torque value, so gears with an allowable torque lesser than 0.25 Nm would be the target. This would result in very small gear units, making it harder to obtain clear visual results regarding wear. For that reason allowable torque values up to 1.3 Nm were considered.

Consulting the catalogues of known gear manufacturers and distributors the list of possible gear pairs presented in Table 3.6 was built. The gears were chosen spanning over different materials and geometric characteristics with the objective of, in future works, testing the wear evaluation method's performance for various gear types, which is also a reason why the demonstrator must have a versatile design.

Table 3.6: Main characteristics of the gears considered for the demonstrator. [54], [55], [56], [57]

Material	**Number of Teeth** z	**Module** m [mm]	**Face Width** b [mm]	**Allowable transmission torque.** T_{lim} [Nm]
Steel	24	1.0	10	0.49
	32	1.0	10	0.9
	38	1.0	10	1.3
Brass	25	0.8	5	0.53
	30	0.8	7	0.96
	48	0.8	5	1.26
Polymer (Poliacetal)	26	1.25	10	0.638
	38	1.25	10	0.932
	28	1.5	12	1.187

It should be noted that for the steel gears, the referenced resistance torque limit is regarding surface pressure, whereas for the brass and polymer gear bending fatigue torque limits were taken. This is due to the fact that for brass and polymer gears, surface resistance is not usually documented.

3.5 Drive train

The designed drive train had to be compliant with the requirements defined in the previous sections, this includes the following: reduction stages for the driving unit and the loading element, appropriate driving shafts to transmit rotational motion, and couplings between shafts.

3.5.1 Reduction stages

Due to the nature of this test rig, all gear-type solutions were excluded to avoid the appearance of extra gear wear information on the vibration signal. To achieve the required torque, two belt-pulley mechanisms were employed. This was deemed the best solution due to the vibrational isolation provided by the mechanism: the only physical connection between the pulleys is the flexible belt, whose elasticity and internal damping attenuate and isolate the structure-borne vibration originating at the brake rather than transmitting it rigidly to the instrumented shafts [58, Ch.17].

A schematic drawing of the full drivetrain is shown in Figure 3.5 and the pulleys used for the aforementioned reduction stages are characterized in Table 3.7.

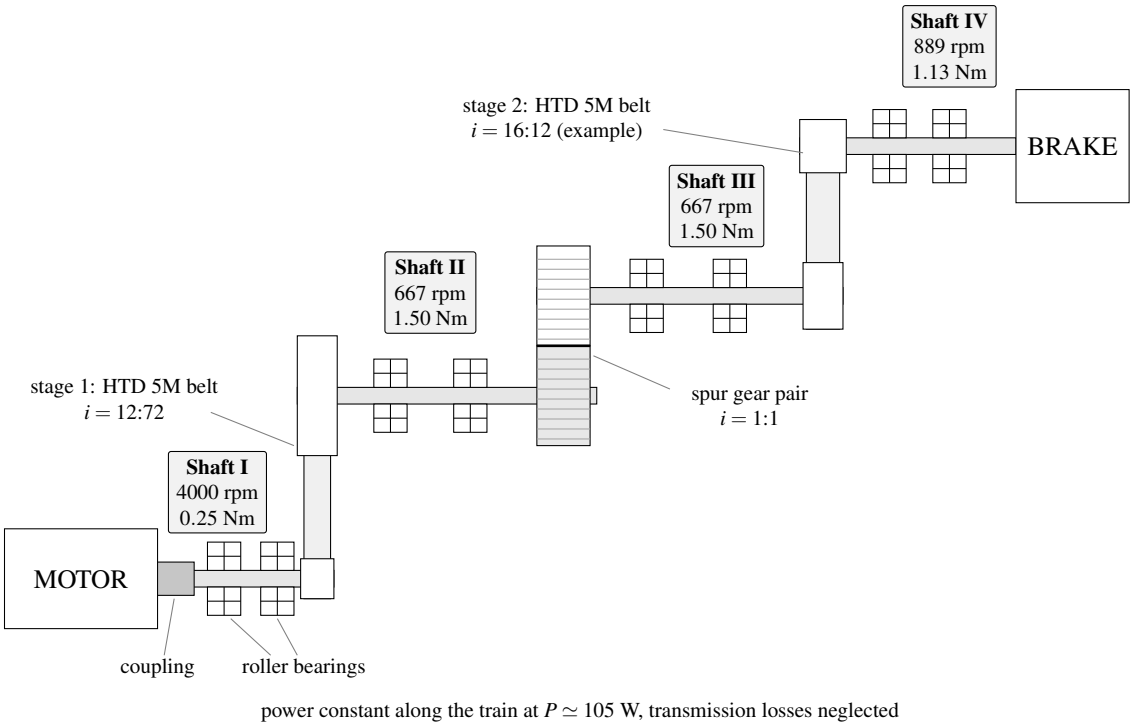


Figure 3.5: Layout of the demonstrator and operating conditions along the power train.

Table 3.7: Characterization of reduction stages.

Stage	Small Pulley (no. of teeth)	Large Pulley (no. of teeth)	Reduction	Belt length [mm]	Center Distance [mm]	Torque [Nm]
Motor	12	72	6	400	80.91	1.5
Brake	12	14	1.167	275	104.99	0.922
	12	16	1.333	275	102.45	1.053
	12	22	1.833	275	94.67	1.448

The values for the required centre distance where obtained using the following equation, which is an approximation developed for friction drives, but serves the purpose of guaranteeing that the proposed assemblies do not require inconceivable centre distances [59]:

$$L = 2C + \frac{\pi}{2}(D_L + D_s) + \frac{(D_L - D_s)^2}{4C} \tag{3.4}$$

Where,

- L is the length of the timing belt;
- C is the centre distance between the pulleys;
- D_L and D_s are the pitch diameters of the large and small pulleys, respectively.

3.5.2 Shafts

To transmit rotational motion regular steel shafts were used. The main design constraint for the shafts was the diameter compatibility with the chosen pulleys, gears, motor and brake. The shaft length was minimized to prevent excessive deflection while remaining long enough to accommodate the required supports and components.

Due to the small dimensions of the test rig, the speed and forces in motion are relatively small, making the shaft fatigue problem somewhat negligible, however, as a sanity check, the fatigue verification of the critical shaft was performed according to the procedure described in Shigley's Mechanical Engineering Design [58, Ch. 7]. A critical speed verification was also carried out, regarding the motor shaft (Shaft I), which spins at the full 4000 rpm, making it a critical component in the design.

Design data and assumptions

The shaft material is EN 1.1191 (C45E), untreated. The data adopted for the verification are summarised in Table 3.8. The shaft is solid with a circular cross section and consists of three parts: a ∅6 mm stub, 6 mm long, where the motor coupling is mounted; a ∅10 mm body, 40 mm long, where the two bearings are fitted; and a ∅6 mm end, 26 mm long, where the small pulley of the first reduction stage is mounted. The axial coordinate x is measured from the edge of the

coupling end, so the two shoulders lie at $x = 6$ mm and $x = 46$ mm and the bearings at $x = 9$ mm and $x = 43$ mm (Figure 3.7).

Table 3.8: Design data and modelling assumptions.

Quantity	Value
Ultimate strength S_{ut}	620 MPa
Yield strength S_y	340 MPa
Surface condition	machined
Operating temperature	20 °C
Reliability	99%
Rotational speed	4000 rpm
Transmitted torque T	0.25 N m
Pulley axial position	$x = 60$ mm
Coupling radial load	neglected
Relief groove (both shoulders)	flat bottomed, 1 mm wide, root ∅5 mm
Groove corner radius	$r \approx 0.1$ mm (assumed)

At 4000 rpm the shaft reaches 10^6 cycles in approximately four hours of operation, so the verification is carried out for infinite life and the endurance limit S_e applies directly.

Load induced by the pulley

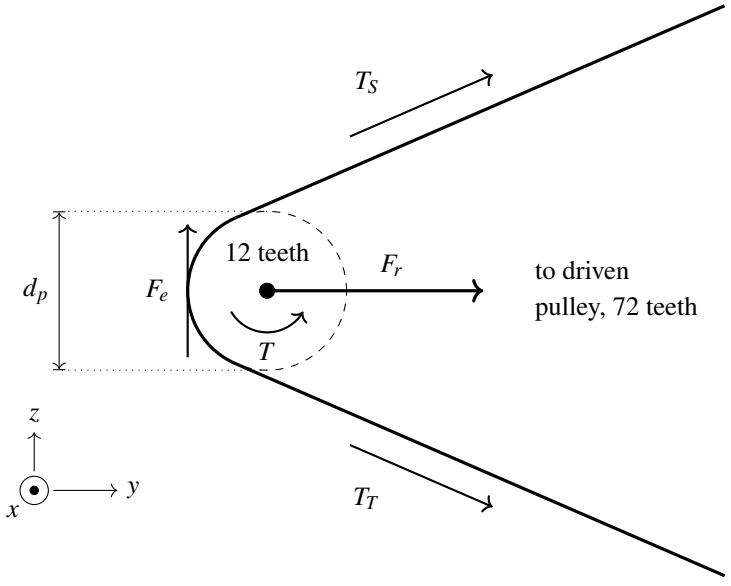


Figure 3.6: Forces acting on the driving pulley.

The driving pulley is an HTD 5M with $z = 12$ teeth, so its pitch diameter and pitch radius are:

$$d_p = \frac{pz}{\pi} = \frac{5 \times 12}{\pi} = 19.10 \text{ mm} \qquad r_p = 9.55 \text{ mm} \tag{3.5}$$

The effective (net) tension is the tangential force that delivers the transmitted torque,

$$F_e = \frac{T}{r_p} = \frac{250}{9.55} = 26.2 \text{ N} \tag{3.6}$$

The shaft is not loaded by F_e alone, however, but by the vector sum of the tight (T_T) and slack (T_S) side span tensions, $T_T + T_S$, whose magnitude depends on the installation tension. Synchronous belt drives are not treated in detail in the reference text, which defers to manufacturer data. Gates defines this resultant as the belt pull and computes it assuming the belt is pre-tensioned to a tension ratio of 8 : 1 for synchronous drives [60]. Combining that ratio with the definition of the effective tension,

$$\frac{T_T}{T_S} = 8 \qquad F_e = T_T - T_S \qquad \Longrightarrow \qquad T_S = \frac{F_e}{7} \quad T_T = \frac{8F_e}{7} \tag{3.7}$$

so that the radial load applied to the shaft by the belt is

$$F_r = T_T + T_S = \frac{9}{7} F_e = 1.286 \times 26.2 = 33.7 \text{ N} \tag{3.8}$$

Equation (3.8) is conservative on two counts: the arithmetic sum of the span tensions is the resultant for a wrap angle of 180°, whereas the wrap on the 12-tooth pulley is appreciably smaller and the true resultant correspondingly lower; and the belt pull excludes the pulley weight, which is negligible here.

The torque is constant and equal to $T_m = 0.25$ N m from the coupling to the pulley. The belt load is stationary in space while the shaft rotates, so the bending stress is completely reversed. Consequently:

$$M_m = 0 \qquad T_a = 0 \tag{3.9}$$

Reactions and bending moment diagram

All loads act in the xOy plane, so a single-plane analysis is sufficient. The pulley is overhung 17 mm beyond the second bearing, while the bearing span is only 34 mm. Equilibrium gives

$$R_2 = F_r \frac{60-9}{43-9} = 50.6 \text{ N } (\uparrow) \qquad R_1 = -F_r \frac{60-43}{43-9} = 16.9 \text{ N } (\downarrow) \tag{3.10}$$

The first bearing is therefore loaded downwards: the overhung pulley levers the shaft about the second bearing. The bending moment diagram is shown in Fig. 3.7. Its maximum, 0.573 N m, occurs at the second bearing, and its value at the relief groove of shoulder B is

$$M_a = F_r (60 - 46) = 33.7 \times 14 = 472 \text{ N mm} = 0.472 \text{ N m} \tag{3.11}$$

Critical Section

Only a few locations need to be evaluated: those where the bending moment is large, where torque is present, and where stress concentrations exist. Three candidates are considered:

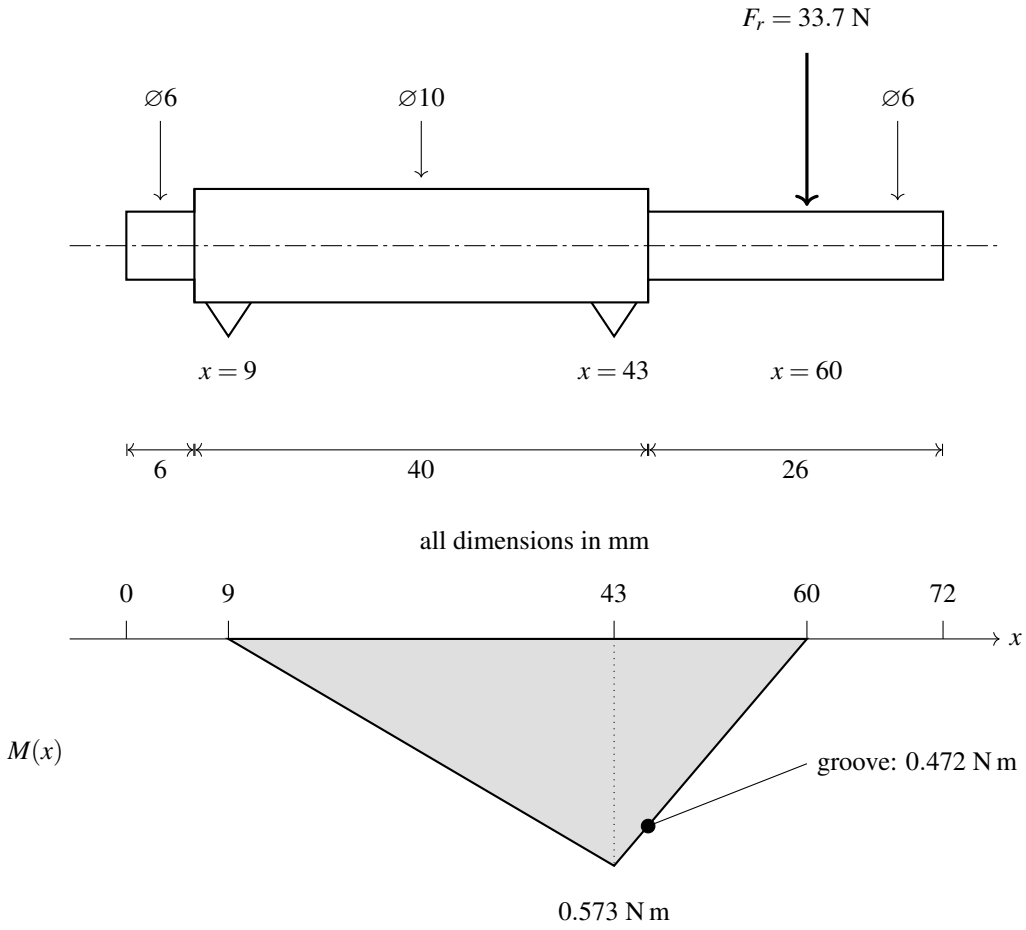


Figure 3.7: Shaft geometry (relief grooves not represented) with the applied loads and the corresponding bending moment diagram.

- **Second bearing,** $x = 43$ **mm.** Largest bending moment (573 N mm), but located on the ∅10 body with no stress raiser.
- **Shoulder A,** $x = 6$ **mm.** A relief groove is present, but there is no transverse load on the shaft between $x = 0$ and the first bearing, so $M = 0$ and only the steady torque acts.
- **Shoulder B,** $x = 46$ **mm.** A relief groove reduces the local diameter to ∅5 mm while the bending moment is still 472 N mm.

Shoulder B governs: its section modulus is $\pi d^3/32 = 12.27$ mm^3 against 98.2 mm^3 at the second bearing, an eightfold penalty for an 18% reduction in bending moment. The verification is therefore done for this section.

Stress concentration at the groove

The groove is a flat-bottomed relief, $a = 1$ mm wide and $t = 0.5$ mm deep radially, cut as a square step from the ∅6 mm section down to a root diameter of ∅5 mm. Because the bottom is flat and the corners square, the radius that governs the stress concentration is not the groove depth but the small corner radius left by the tool, which is not specified on the part. The reference work notes that flat-bottomed grooves of this kind, in which the bottom radius is of the order of one tenth of the groove width, produce stress-concentration factors near 5 in bending and 3 in torsion [58]. Taking the worst credible case, $r \approx 0.1$ mm, the governing ratios are

$$\frac{a}{t} = \frac{1}{0.5} = 2.0 \qquad \frac{r}{t} = \frac{0.1}{0.5} = 0.20 \tag{3.12}$$

and the corresponding charts for flat-bottomed grooves give

$$K_t = 5.0 \text{ (bending)} \qquad K_{ts} = 3.0 \text{ (torsion)} \tag{3.13}$$

These geometric factors are reduced to fatigue stress-concentration factors through the notch sensitivity q, obtained from the Neuber relation:

$$q = \frac{1}{1 + \dfrac{\sqrt{a}}{\sqrt{r}}} \tag{3.14}$$

in which the Neuber constant $\sqrt{a}$ is a function of the ultimate strength alone. For $S_{ut} = 620$ MPa the constants are $\sqrt{a} = 0.361$ $\sqrt{\text{mm}}$ in bending and $\sqrt{a} = 0.272$ $\sqrt{\text{mm}}$ in torsion, so that with $r = 0.1$ mm Eq. (3.14) yields $q = 0.47$ and $q_s = 0.54$. The fatigue stress-concentration factors follow as

$$K_f = 1 + q\,(K_t - 1) = 1 + 0.47\,(5.0 - 1) = 2.87 \tag{3.15}$$

$$K_{fs} = 1 + q_s\,(K_{ts} - 1) = 1 + 0.54\,(3.0 - 1) = 2.07 \tag{3.16}$$

The sharpness of the corner is partly self-limiting: a smaller radius raises K_t but lowers the notch sensitivity through Eq. (3.14), so the product K_f is far less sensitive to r than K_t alone. Repeating the calculation for $r = 0.05$ mm changes final factor of safety by less than 8%, which makes the assumed corner radius an acceptable basis for the verification despite not being specified.

Endurance limit

For steels with $S_{ut} \leq 1400$ MPa the rotating-beam endurance limit is estimated as

$$S'_e = 0.5\, S_{ut} = 0.5 \times 620 = 310 \text{ MPa} \tag{3.17}$$

This value is corrected to the conditions of the actual component through the Marin factors,

$$S_e = k_a\, k_b\, k_c\, k_d\, k_e\, S'_e \tag{3.18}$$

whose expressions and values for this shaft are given in Table 3.9. The load factor is $k_c = 1$ because the combined bending and torsion is handled through von Mises equivalent stresses, and the temperature factor is $k_d = 1$ at 20 °C.

Table 3.9: Marin modifying factors at the groove of shoulder B.

Factor	Expression	Value
Surface, k_a	$a\, S_{ut}^{b}$, with $a = 4.51$, $b = -0.265$ (machined)	0.821
Size, k_b	$1.24\, d^{-0.107}$, with $d = 5$ mm	1.044
Load, k_c	combined loading via von Mises	1
Temperature, k_d	20 °C	1
Reliability, k_e	99% reliability	0.814

The surface factor uses S_{ut} in MPa, and the size factor d in mm. The latter exceeds unity because the expression rewards diameters below 7.62 mm and remains valid down to 2.79 mm. Substituting into Eq. (3.18),

$$S_e = 0.821 \times 1.044 \times 1 \times 1 \times 0.814 \times 310 = 216 \text{ MPa} \tag{3.19}$$

Safety factor

Among the distortion-energy fatigue criteria available for a rotating round shaft under fluctuating bending and torsion, the DE–Soderberg criterion [61] is adopted here. It is the most conservative of the family, and because it references the midrange stress to the yield strength rather than to the ultimate strength it inherently guards against first-cycle yielding, so that no separate static check is required. Introducing the alternating and midrange load combinations

$$A = \sqrt{4\,(K_f M_a)^2 + 3\,(K_{fs} T_a)^2} \qquad B = \sqrt{4\,(K_f M_m)^2 + 3\,(K_{fs} T_m)^2} \tag{3.20}$$

the criterion reads

$$\frac{1}{n} = \frac{16}{\pi d^3}\left(\frac{A}{S_e} + \frac{B}{S_y}\right) \tag{3.21}$$

At the groove of shoulder B the load set is $M_a = 0.472$ N m, $T_m = 0.250$ N m, $M_m = T_a = 0$ and $d = 5$ mm, so that $16/(\pi d^3) = 0.0407$ mm^{-3} and Eq. (3.20) reduces to

$$A = 2K_f M_a = 2706 \text{ N mm} \qquad B = \sqrt{3}\,K_{fs} T_m = 898 \text{ N mm} \tag{3.22}$$

Substituting into Eq. (3.21),

$$\frac{1}{n} = 0.0407\left(\frac{2706}{216} + \frac{898}{340}\right) = 0.0407\left[12.53 + 2.64\right] = 0.618 \tag{3.23}$$

which gives

$$n = 1.6 \tag{3.24}$$

The governing section is the relief groove at shoulder B, where the DE–Soderberg factor of safety is $n = 1.6$. Since this criterion also covers first-cycle yielding, the shaft is verified for infinite life under the loads considered.

The margin is dominated by a single feature. The flat-bottomed relief groove alone accounts for a factor of roughly two in the result: with a full-radius groove of the same depth, all other data unchanged, the same calculation returns $n = 3.0$. The flat-bottom groove is an inherent design feature imposed by the shaft manufacturer, so, should the design of the shafts be revisited, filleting the bottom of the relief groove is by a margin the most effective change available.

Critical speed

At certain rotational speeds a shaft resonates laterally and its deflections grow without bound. The design requirement is that the first critical speed be at least twice the operating speed [58], that is, 8000 rpm for this shaft.

The procedure of the reference work is followed: the assembly is reduced to a set of discrete masses and their contributions combined through Dunkerley's equation [62],

$$\frac{1}{\omega_1^2} \simeq \sum_i \frac{1}{\omega_{ii}^2} = \sum_i m_i\,\delta_{ii} \tag{3.25}$$

where m_i is the mass of station i and δ_{ii} the deflection at that station under a unit transverse force applied there. The term $\omega_{ii} = (m_i\delta_{ii})^{-1/2}$ is the critical speed the assembly would have if station i were its only mass: the natural frequency of a mass m_i on a spring of stiffness $1/\delta_{ii}$, the shaft being that spring. Equation (3.25) neglects the higher modes and therefore underestimates the first critical speed, which is conservative.

The closed-form expressions for δ_{ij} given alongside Eq. (3.25) in the reference work are not applicable here. They assume a constant flexural rigidity, whereas this shaft steps from ∅6 to ∅10 and back; and they assume both the load and the station of interest to lie between the supports,

whereas the pulley overhangs the second bearing by 17 mm and the coupling overhangs the first by 6 mm. The tabulated case for an overhanging load removes the second objection but not the first, and since the change of section falls inside the overhang it also falls out of the equation's scope.

Influence coefficients Castigliano's theorem gives the deflection at a point as the derivative of the strain energy with respect to a force applied there. With a unit force, and retaining only bending strain energy, this gives the unit-load integral

$$\delta_{ii} = \int_0^{\ell} \frac{M_i^2(x)}{E\,I(x)}\,\mathrm{d}x \tag{3.26}$$

in which $M_i(x)$ is the bending moment produced along the shaft by a unit transverse load at station i, the shaft being supported at the two bearings. Since $I(x)$ remains inside the integral and $M_i(x)$ follows from statics alone, Eq. (3.26) accommodates both the change of section and the overhangs without modification.

The moment distribution is constructed as in Fig. 3.7, replacing the belt load by a unit load at the station of interest. For a station on the pulley overhang, at $x_i > x_B$, equilibrium gives

$$R_B = \frac{x_i - x_A}{x_B - x_A}\ (\uparrow) \qquad R_A = 1 - R_B\ (\downarrow) \tag{3.27}$$

Evaluating Eq. (3.26) with $E = 207$ GPa over the stepped geometry gives the influence coefficient at the pulley (δ_p) and coupling (δ_c) locations,

$$\delta_p = 1.088 \times 10^{-4}\ \text{mm/N} \qquad \delta_c = 5.319 \times 10^{-6}\ \text{mm/N} \tag{3.28}$$

Figure 3.8 shows the variation of the influence coefficient along the shaft.

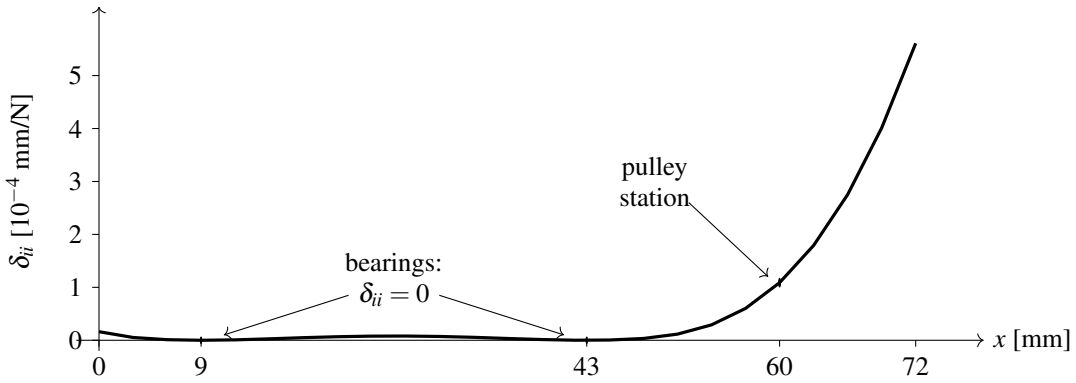


Figure 3.8: Influence coefficient δ_{ii} along the shaft.

Discretisation The mass of the assembly is partly distributed, in the shaft material, and partly concentrated, in the pulley and the coupling. Writing it as a single mass measure along the axis,

$$\mathrm{d}m(x) = \underbrace{\rho\, A(x)\,\mathrm{d}x}_{\text{shaft}} + \underbrace{m_p\,\delta_{\mathrm{D}}(x-x_p)\,\mathrm{d}x \;+\; m_c\,\delta_{\mathrm{D}}(x-x_c)\,\mathrm{d}x}_{\text{attachments}} \tag{3.29}$$

with δ_{D} the Dirac distribution, Dunkerley's sum becomes a single integral against that measure,

$$\frac{1}{\omega_1^2} \simeq \int_0^{\ell} \delta_{ii}(x)\,\rho\, A(x)\,\mathrm{d}x \;+\; m_p\,\delta_p \;+\; m_c\,\delta_c \tag{3.30}$$

the concentrated terms being sifted out by the Dirac distributions.

The distributed integral is evaluated by partitioning the shaft into segments and placing the mass of each at its own centroid,

$$\int_0^{\ell} \delta_{ii}(x)\,\rho\, A(x)\,\mathrm{d}x \;\simeq\; \sum_k m_k\,\delta_{ii}(\bar{x}_k) \qquad m_k = \rho \int_{x_k}^{x_{k+1}} A(x)\,\mathrm{d}x \tag{3.31}$$

$\bar{x}_k$ denoting the centroid of segment k. The shaft is divided into 36 segments of equal length, $\Delta x = 2$ mm, this being the smallest number of equal segments for which no segment contains a change of section (Figure 3.9).

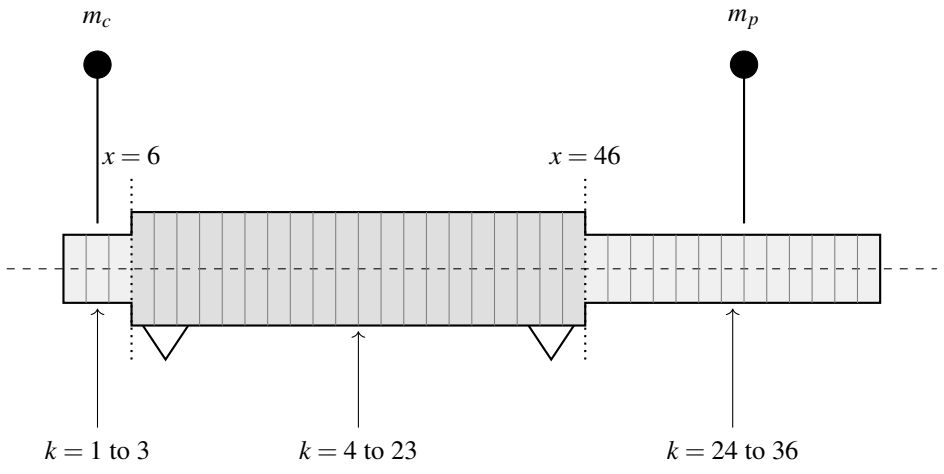


Figure 3.9: Discretisation of the shaft into 36 equal segments of $\Delta x = 2$ mm.

Results The pulley is a steel cylinder of 19.1 mm diameter and 21 mm length, and the coupling an aluminium tube of 14 mm outer diameter, 6 mm bore and 12 mm length, so that

$$m_p = \rho_{\mathrm{st}}\,\frac{\pi d^2}{4}\,\ell = 46.9\ \mathrm{g} \qquad m_c = \rho_{\mathrm{Al}}\,\frac{\pi(D^2-d^2)}{4}\,\ell = 4.1\ \mathrm{g} \tag{3.32}$$

with $\rho_{\mathrm{st}} = 7800$ kg/m^3 and $\rho_{\mathrm{Al}} = 2700$ kg/m^3. Table 3.10 collects the thirty-eight stations of Eq. (3.30), the shaft segments being grouped by diameter.

Table 3.10: Stations contributing to the first critical speed, grouped by diameter.

Station	Position [mm]	m_i [g]	δ_{ii} [mm/N]	$\sum m_i \delta_{ii}$ [s^2]
Coupling	$x_c = 3$	4.1	5.32×10^{-6}	2.17×10^{-11}
Shaft $k = 1$ to 3, ⌀6	$0 \le x \le 6$	1.3	—	8.34×10^{-12}
Shaft $k = 4$ to 23, ⌀10	$6 \le x \le 46$	24.5	—	9.07×10^{-11}
Shaft $k = 24$ to 36, ⌀6	$46 \le x \le 72$	5.7	—	8.81×10^{-10}
Pulley	$x_p = 60$	46.9	1.09×10^{-4}	5.11×10^{-9}
Sum		82.5		6.11×10^{-9}

Substituting into Eq. (3.25),

$$\omega_1 = \sqrt{\frac{1}{6.11 \times 10^{-9}}} = 12\,796 \text{ rad/s} \simeq 122\,000 \text{ rpm} \tag{3.33}$$

which is about 31 times the considered operating speed of 4000 rpm. The pulley accounts for 84% of the sum. Of the shaft's own 16%, nine tenths comes from the thirteen segments of the pulley overhang, although they hold under a fifth of the shaft mass: in Eq. (3.30) position outweighs mass, since δ_{ii} varies by orders of magnitude along the shaft while the segment masses vary only with the square of the diameter.

Limitations of the model. Several effects have been omitted, and their direction is worth recording:

- **Rotary inertia of the attachments.** The pulley and coupling are treated as point masses with no diametral moment of inertia. A real overhung disc resists the angular deflection of the shaft at its station, which raises the critical speed.
- **Local stiffening.** The hubs clamp over the shaft and stiffen it locally, whereas $I(x)$ is taken as that of the bare shaft.
- **Finite width of the attachments.** Lumping the pulley mass at a single station slightly overstates its contribution, since part of that mass lies inboard where δ_{ii} is smaller.
- **Bearing flexibility and shear deformation.** The bearings are treated as ideal pin supports and only bending strain energy is retained in Eq. (3.26). Both make the real shaft marginally more flexible than modelled.

None of these act against safety, the shaft is therefore free of any critical speed concern, and it is the fatigue verification at the relief groove that governs the design.

3.6 Structural components

The structural integrity of the test rig is a fundamental requirement for ensuring the accuracy and repeatability of the vibration data. The frame must not only support the mechanical load of the motor and brake but also provide a rigid reference that guarantees geometrical alignment between the components. Two other key aspects of this specific test rig are: the size and weight constraints due to the intended scale of the rig, it must maintain a portable weight and reasonable, ergonomic dimensions; and the setup should allow a degree of modularity to accommodate different configurations, including various gear pairs and load reductions.

3.6.1 Rig Frame: Aluminium Profiles

The primary frame of the demonstrator is constructed from T-slot aluminium extrusion profiles. This material was selected primarily for its high strength-to-weight ratio and design modularity. The standardized profile connections make for an efficient way to easily vary the positions of the main components, allowing for the versatility required for this application.

3.6.2 Rotational Support: Rolling Element Bearings

To support the shafts and ensure smooth power transmission, deep-groove rolling element bearings were utilized. In the context of a vibration-based test rig, the choice of the bearings is critical as they represent a secondary source of vibration. Rolling element bearings are preferred over bushings for this application due to their lower and more consistent friction coefficient, which ensures that the torque required to drive the system remains stable. Additionally, because the vibration signatures of healthy and faulty bearings are well-documented in the literature, utilizing standard commercial units allows the signal processing pipeline to more easily identify and filter out bearing-induced frequencies, thereby isolating the signals of interest.

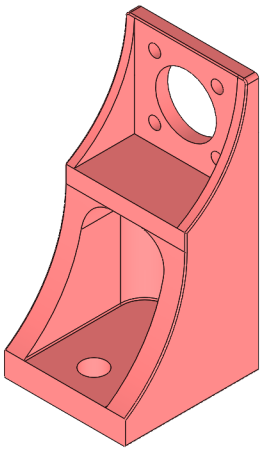
3.6.3 Custom Interfaces: 3D Printed Supports

For the more geometrically non-standard components, such as sensor mounts, motor and shaft supports, Additive Manufacturing (3D printing) was employed, specifically Fused Deposition Modelling, using Polyethylene Terephthalate Glycol filament (PETG). This manufacturing solution presents the following key characteristics:

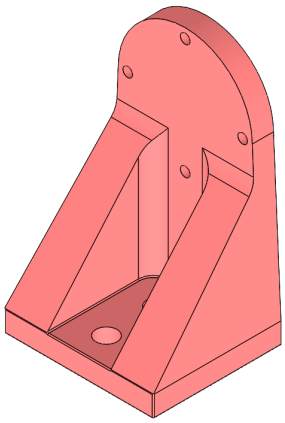
- **Design Versatility:** 3D printing allows for the creation of optimized geometries that would be difficult or expensive to produce via traditional subtractive manufacturing.
- **Cost-Efficiency:** It significantly reduces the prototype development cost, allowing for multiple iterations of the structural interface to ensure good component alignment.
- **Compliance:** The 3D-printed supports cannot be expected to match the structural rigidity of a cast iron gearbox housing, which represents a potential weakness of the design. Given

the low torque levels involved and the time available, this limitation was accepted at the design stage.

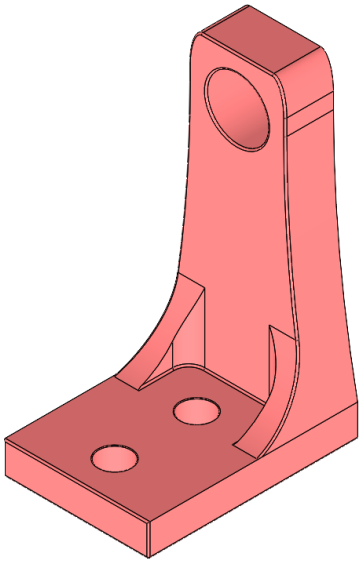
For this test rig 4 types of supports were developed (Figure 3.10). The motor and brake supports were designed to maximize shaft alignment by reducing possible deflection due to the components' weight, 2 different types of bearing supports were developed to satisfy the space constraints of the rig.



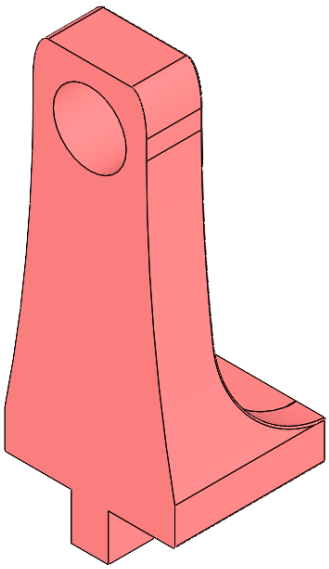
(a) Motor support



(b) Brake support.



(c) Long bearing support



(d) Short bearing support.

Figure 3.10: Additively manufactured supports used in the demonstrator.

The bearing supports were printed in PETG using a grid infill pattern at 15 % infill density. The grid pattern was selected because, among the patterns characterised by Öteyaka et al. [63], it

exhibited the lowest damping ratio, with the cross pattern the most dissipative and the tri-hexagon intermediate. As the supports lie in the transmission path between the gear mesh and the accelerometer, low damping is desirable, since any attenuation introduced by the mounting would dilute the high-frequency content on which the diagnostic indicators depend.

The 15 % density was set by print time and material economy rather than by a structural requirement, and it represents a deliberate compromise. The same study reports that flexural modulus and flexural strength increase monotonically with infill ratio; for the grid pattern the flexural modulus rises from 2.12 GPa at 0 % to 3.23 GPa at 100 % [63]. If it is verified that the supports are too flexible, increasing the infill density is a direct remedy, since it substantially raises the stiffness and strength of printed PETG [64].

It should be noted that Öteyaka et al. [63] tested PLA rather than PETG, and over an infill range of 0–100 % in 20 % steps, so both the ranking of patterns and the behaviour at 15 % are transferred on the assumption that damping is governed primarily by infill geometry.

3.7 Completed Design

Using the components described in the previous sections, the demonstrator assembly was designed using Solidworks, the necessary components were bought or manufactured, resulting in the demonstrator shown in Figure 3.11.

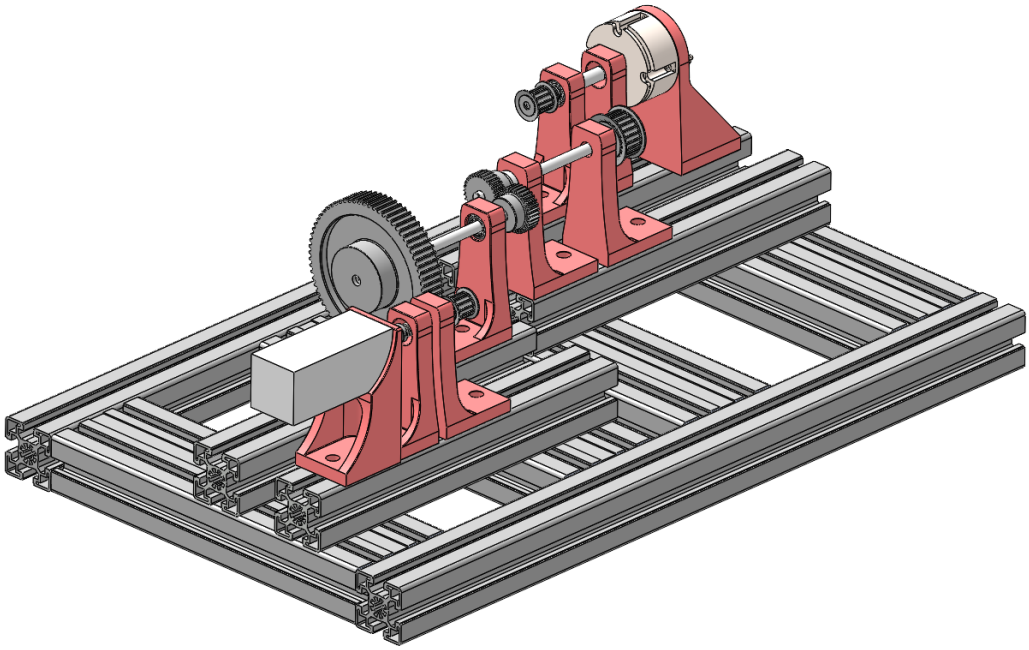


Figure 3.11: 3D assembly of the demonstrator, designed in Solidworks.

Chapter 4

Computational Implementation

4.1 Wear evaluation

In DT applications, aside from the physical characterization of the mechanical system, an important metric to have available is the Remaining Useful Life (RUL) of the system. As shown in the previous chapter, there are no widespread methods to determine the RUL of a gear pair from its vibration signal, currently available methods often depend on available test data from similar systems and calibrating the indicators with the recorded RUL of the test. Alternatively, Machine Learning algorithms can be employed that may provide some flexibility on system parameters, but on the other hand, require large amounts of good quality training data, that matches the sensor data and metrics included in the present study.

The computational implementation done in this work will not have a RUL algorithm, falling short of a DT's desired capability, leaving that gap for future research done on this project. The wear quantification carried out will be based on visual examination of the test gears as the experimental campaign progresses and comparing with standardized records and other reference images found in the literature.

From the vibration monitoring standpoint, several CIs will be calculated and analysed against visually recorded wear, as to verify the demonstrator's capability, not only of inducing damage on the gear pair, but also of providing a reliable propagation path for the vibration signature produced by the worn-out components. This check is necessary due to the fact that pieces supporting the gear shafts will be made of PETG polymer, posing a risk of the material's inherent damping properties affecting the recorded signal in incapacitating ways.

4.2 Instrumentation

To perform the wear evaluation on the developed demonstrator 2 types of data need to be acquired: the vibration on the shaft supports and the angular position of the shafts, to register shaft revolutions.

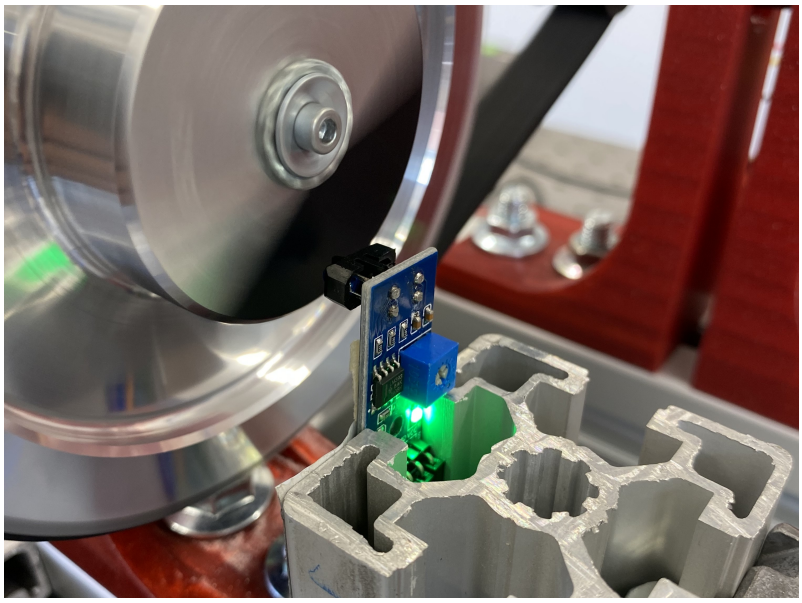


Figure 4.1: Demonstrator tachometer.

The accelerometers used are the Model 35A17 accelerometers from PCB Piezotronics, and will be placed on top of the 3D-printed supports, attached using wax. They provide tri-axial vibration sensoring with an acquisition rate up to 4 kHz. Taking as an example the 48 teeth brass gear from Table 3.6, assuming that the motor is spinning at 4000 rpm, due to the 6:1 reduction in stage 1, we have a meshing frequency of 533 Hz and so the sensor can safely register information up to the GMF's third harmonic (Nyquist frequency = $4000/2 = 2000$, $GMF_3 = 1600$ Hz) this is not the ideal acquisition rate capturing up to the 6th harmonic as recommended by Hu et al. [19], but for the purpose of this work it was deemed sufficient.

As for the angular position sensor since, due to the lack of space, it was not possible to include an incremental encoder in the design, a revolution counter was built using a TCRT5000 reflective optic sensor pointed at the face of the large Stage 1 pulley (see Figure 4.1). From now on this sensor will be referred to as the "Tachometer".

The acceleration data was collected using NI-9232 modules and the tachometer data was acquired through an NI-9219 module, these were mounted on a cDAQ-9189 chassis, connected to the lab's computer. All of the data was then logged into .csv files via the National Instruments software Flexlogger.

Regarding the control of the motor a STEVAL-SPIN3201 driver from ST Microelectronics (STM) was used, connected to the DC power supply and the computer and ran using STM's own Motor Control Workbench software. A sketch representation of the demonstrator's sensor placement and connectivity is shown in Figure 4.2.

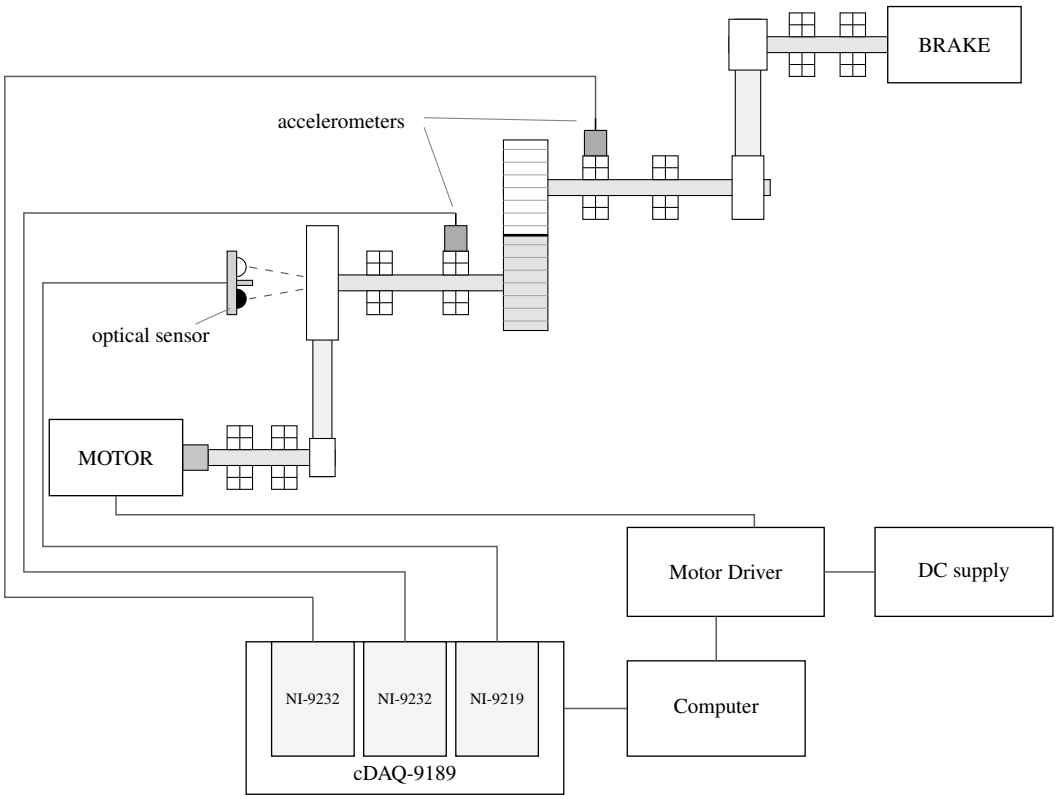


Figure 4.2: Sensor placement on the demonstrator and the data acquisition chain.

4.3 Data flow and signal processing

The algorithm developed is composed of two main stages, the signal building stage, where the test data is imported into the model and treated to form the required vibration signals described in Chapter 2 and the CIs calculation stage, where the computed signals are used to calculate the proposed CIs.

4.3.1 Signal Treatment

A diagram portraying the data flow and operations included in this stage can be analysed in Figure 4.3. The .csv file containing the test data is imported into the model and converted into a Dictionary variable, the signals are then truncated as to guarantee that there are only full revolutions in the data, this yields the raw vibration signal which will be used for CI calculation. The raw signal is then split into revolutions according to the transitions in the tachometer signal, the individual revolutions are order tracked into the angular domain as to perform the TSA, obtaining another signal for CI calculation. The TSA signal is used to calculate the remaining signals, its frequency spectrum is calculated to extract the relevant amplitudes at shaft harmonics, GMF harmonics and first-order sidebands used to compute the regular meshing signal and the difference signal.

Aside from purely treating the test data and forming the signals, in this stage the computed signals are also plotted in the time and frequency domain for visualization purposes.

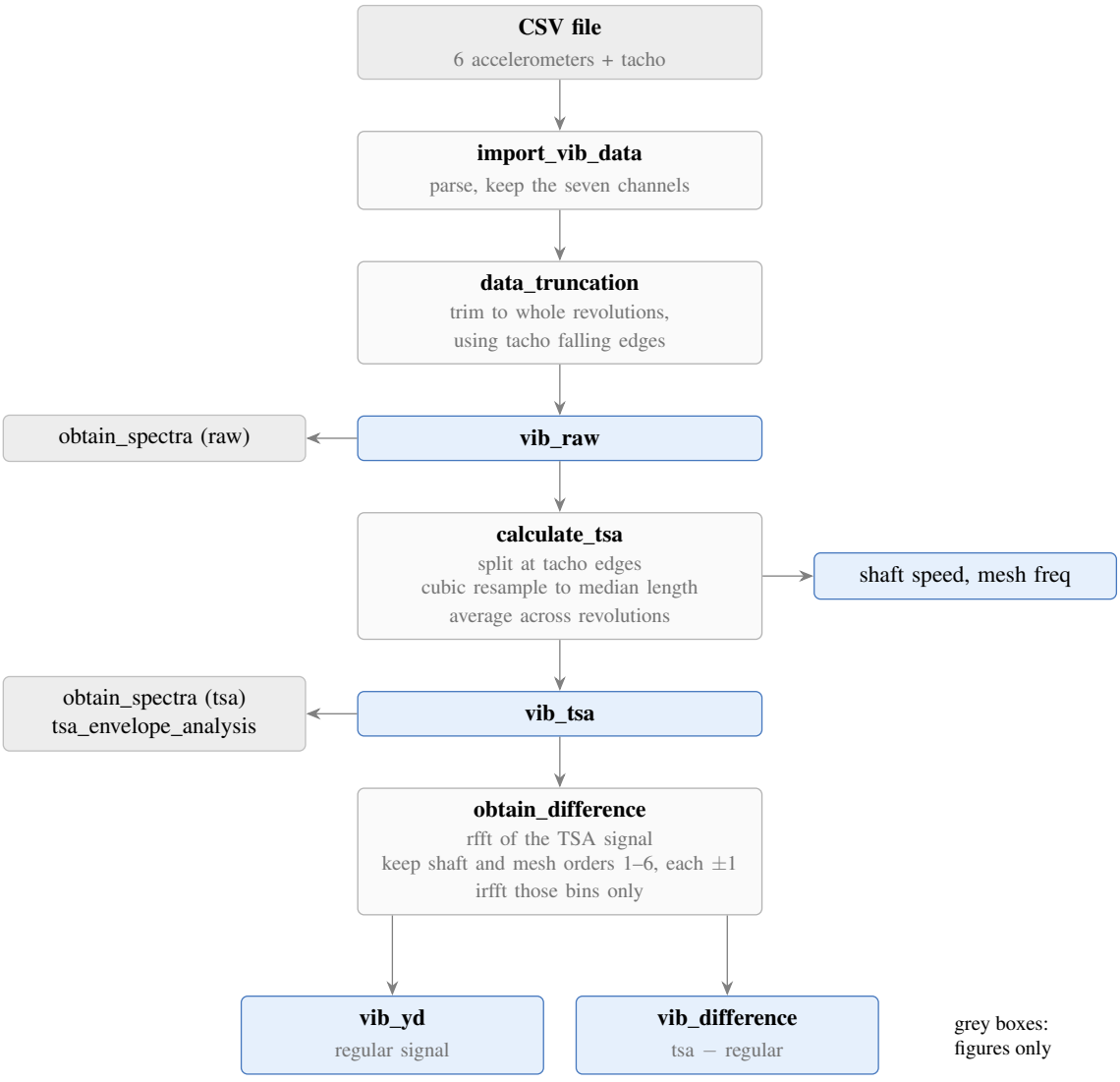


Figure 4.3: Diagram of the Signal Treatment stage of the program.

4.3.2 CIs Calculation

A diagram portraying the data flow and operations included in this stage can be analysed in Figure 4.4. The four signals computed in the previous stage are the input of this stage, each one feeding the indicators for which it is best suited. The RMS value and the kurtosis are obtained for the raw, TSA and difference signals, while the maximum peak acceleration is taken only from the raw signal. The FM4 indicator is computed from the difference signal and the ER from the RMS values of the difference and regular signals. The frequency-domain indicators are then computed in two separate branches: the raw signal is used to locate the frequency band in which the impulsive content is most prominent, which is then band-pass filtered and demodulated to extract the envelope indicators; the TSA signal is used in the order domain to compute the SBRs of the meshing harmonics, which form the gear state vector and from which the ALR is obtained against the first file of the run.

All the indicators computed are stored in a dictionary indexed by the timestamp of the corresponding data file, with one entry per accelerometer, so that their evolution over the test campaign can be plotted against the visually recorded wear.

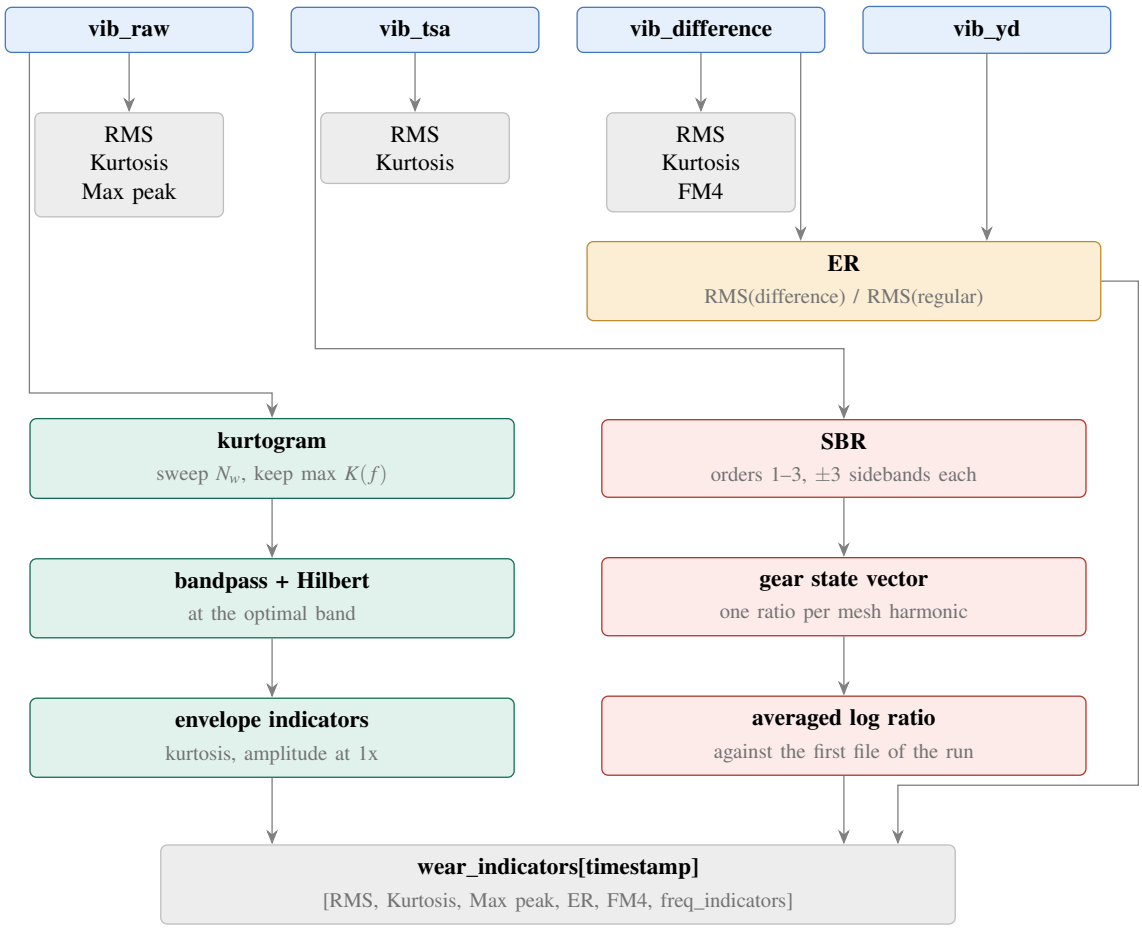


Figure 4.4: Diagram of the CI Computation stage of the program.

Chapter 5

Demonstrator Assembly

After manufacturing and acquiring all the necessary components the demonstrator was assembled (see Figure 5.1) and initial tests were performed to assess the demonstrator's capabilities and working conditions.

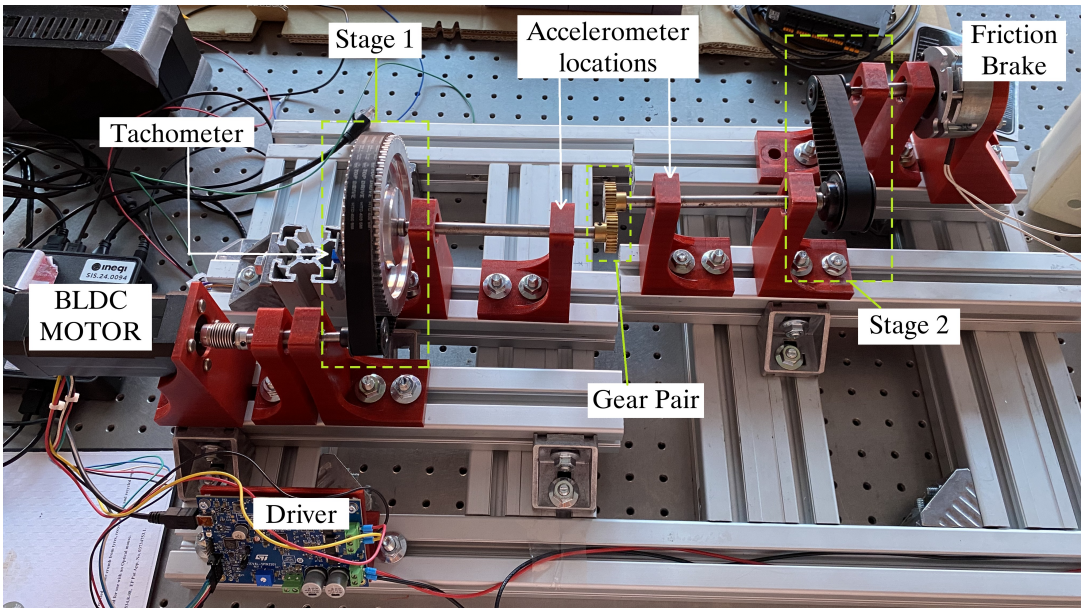


Figure 5.1: Assembled demonstrator at INEGI's facilities.

5.1 Test Rig Limitations

On the initial trials when trying running the demonstrator powered by the motor it was verified that the chosen motor was not able to drive the system, upon powering on the supply the motor drew up current without being able to rotate the shafts and kept drawing more current until one of the following occurred:

- **Tooth skipping at the gears**: as the motor's power increased, the normal force at the gear interface increased, causing the 3d-printed supports to deflect, until the deflection allowed

for the teeth to skip and the input gear to rotate for a short time, until clashing into the output gear and stopping again.

- **Tooth skipping at the stage 2 pulleys**: as the motor drew increasing current from the power supply the belt tension increased and, due to poor meshing between the toothed belt and the pulleys, the belt teeth eventually started skipping over the pulleys until the demonstrator was shut down. The reason behind poor meshing might be in the lack of a tensioning system in the pulley and the fact that we are working in the lower end of standard diameters for HTD 5M pulleys, resulting in a lower number of teeth in mesh.

Regarding vibration data acquisitions, a preliminary data acquisition was performed, running the system with no load, and it was verified that the registered vibration yielded rather unintelligible results, FFTs of the raw, unfiltered vibration appeared smeared and with difficult to distinguish peaks. The absence of load is the principal explanation: the deterministic mesh excitation scales with the transmitted torque, and with no resisting torque the tooth flanks are not held in contact, so contact is repeatedly lost and re-established within the available backlash, producing an impulsive excitation that is not repeatable from one mesh to the next and that distributes energy across the spectrum instead of concentrating it at the GMF's harmonics. Shaft speed fluctuation, likewise unopposed under a *loadless* regime, broadens the peaks further, and the gear misalignment from support deflection degrades the mesh conditions themselves. The fixation method is not a plausible cause, since the measurement band is limited to 2 kHz (Section **??**) and wax, adhesive and stud mountings are reported to give indistinguishable responses over that range [65], [66], [67]. The result nevertheless highlighted the importance of having a proper signal filtering algorithm employed before computing any type of indicator.

5.2 Modifications

Due to the malfunctions encountered in the early testing phase, two priorities were defined for the test rig modifications: increase in the lateral rigidity of the shaft supports and a redesign of the mounting method of the sensors. The following modifications were employed:

- Design of a box-like structure as a housing for the gear pair, having shafts II and III physically connected instead of their only interface being the meshing gears will greatly increase lateral rigidity and make the system more similar to gear applications in the industry, as they often appear in the form of reduction gearboxes.

- The designed housing includes slots that locate the accelerometers, clamped in place with a screw. Wax provides no feature to position the sensor and its bond softens over long runs, so the transfer path between mesh and sensor is not repeatable between acquisitions; since the wear evaluation compares indicators across the campaign, a drift in mounting would be indistinguishable from one produced by wear [31].

Another relevant design feature for the gearbox is the centre distance. The gearbox was designed with the bearing housings sitting 31.75 mm, a distance smaller than the theoretical wheelbase of 32 mm for a pair of 32 teeth, 1 mm modulus gears. This was done as an added safety measure to avoid the possibility of tooth skipping in the gears, increasing the support deflection needed for the phenomenon to happen and to further accelerate wear.

A 3D model of the proposed modifications is shown in Figure 5.2.

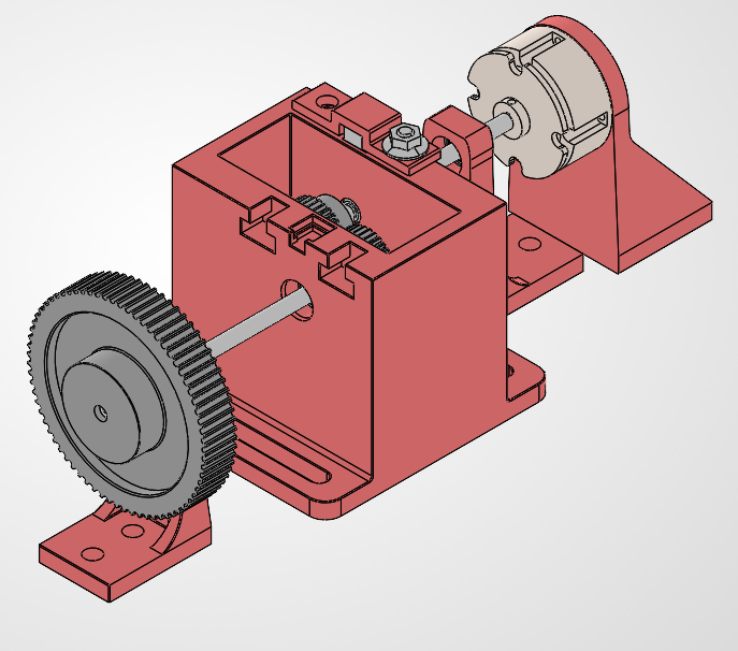


Figure 5.2: Simplified 3D model of the modified test rig, excluding the structural base, the motor and the first reduction stage.

5.3 Modified Test Rig Behaviour

Following the implementation of the modifications described in the previous section, a new set of trials was carried out in order to verify whether the identified limitations had been corrected. These trials were performed without the second reduction stage, meaning the output shaft was directly connected to the brake.

The gearbox modification proved effective. With shafts II and III rigidly connected through the housing, no tooth skipping was observed at the gear pair for any of the attempted operating conditions, confirming that the lateral deflection of the shaft supports had been the mechanism responsible for the loss of mesh reported in Section 5.1. The relative position of the gear axes is now imposed by the housing rather than by the individual supports, which both avoids the failure mode and brings the assembly closer to the configuration of industrial reduction gearboxes.

The motor, however, remained unable to drive the system. Upon powering the supply, the current drawn rose progressively until stabilising at approximately 300 mA, at which point the

motor either stabilized at that current value or the drive returned an error in the STM Motor Control Workbench environment, forcing a shutdown. This behaviour was repeatable across trials.

In order to determine whether the obstruction was mechanical or electrical in nature, the drive train was manually rotated at the stage 1 large pulley. Under manual actuation the complete kinematic chain rotated, including the actuated brake, without any tooth skipping at the gear pair, and without any evidence of critical damage to the components. This demonstrates that the torque required to drive the system is within the capability of a manual input, and therefore that the malfunction is likely confined to the motor and its control algorithm rather than to the mechanical assembly.

Three hypotheses were formulated for the observed behaviour:

- **Additional power losses due to misalignment**: although the supports adjacent to the gear pair were redesigned and no longer present significant deflection, the remaining supports are of the same design and may still deflect, rotating the shafts in plane when loaded. Furthermore, the bearing housings' geometry is itself 3D-printed and the assembly is mounted on an aluminium profile frame, which offers limited control over the concentricity between bearings and the over wheelbase of both the gear pair and the pulleys. The resulting misalignment introduces loads at the bearings and at the mesh, increasing the torque demanded from the motor.

- **Underestimation of the brake torque**: the brake is of the spring-applied friction type, a constructive solution intended primarily for holding and full-stop applications, in which an excess of torque relative to the rated value is not detrimental and may even be desirable. It is therefore plausible that the rated torque is affected by a safety factor and that the actual resisting torque delivered by the brake exceeds it.

- **Current limitation in the motor control chain**: the current at which the motor stalls, approximately 300 mA, is far below both the rated current (5 A) and the maximum peak current of 20 A declared for the motor. The fact that the drive never approaches these values suggests that the current is being capped somewhere in the control sequence rather than by the physical load, which would explain the inability to develop the necessary starting torque.

Of the three, the last is considered to be the most likely to be the dominant cause, since the motor never draws a current consistent with the torque it is rated to produce and the manual rotation test established that the mechanical resistance of the drive train can be overcome by a modest input torque.

Due to time constraints, no alternative load-imposing solution was implemented, and the data acquisition campaign was consequently carried out under no-load conditions. A set of preliminary runs was performed in the modified rig in order to assess whether the smearing of the spectra reported in Section 5.1 persisted after the redesign of the housing and of the sensor fixation; these results are presented and discussed in Chapter 6.

Chapter 6

Results and Discussion

This Chapter presents and discusses the results of the experimental campaign carried out on the demonstrator. The test rig layout used for the testing phase is shown in Figure 6.1.

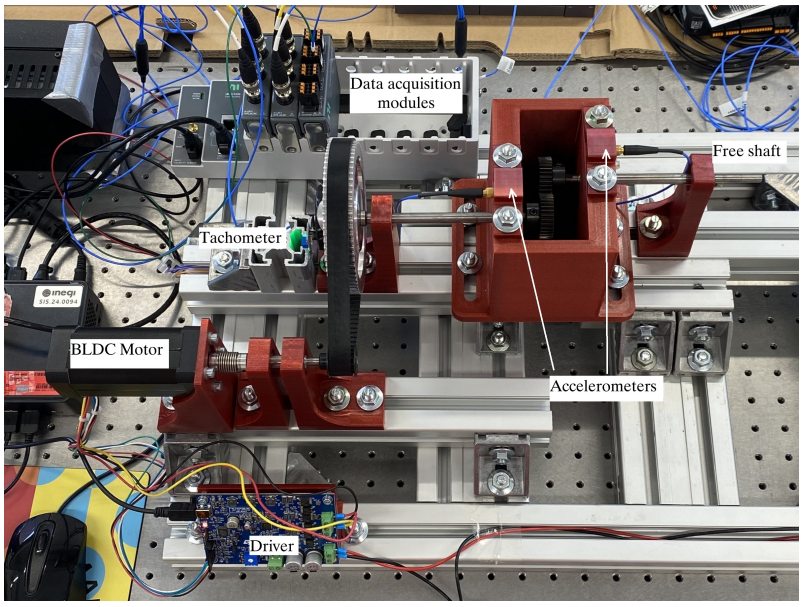


Figure 6.1: Test rig layout used for data acquisition.

The Chapter opens with a definition of the operating conditions under which the data were acquired, followed by an overview of the campaign and of its outcome. The condition of the gear pair and the events observed during operation are then reported, before the evolution of the CIs is examined.

6.1 Experimental Conditions

As established in the previous Chapter, the motor was not able to drive the system against the brake, and the campaign was therefore carried out under no-load conditions, with the second

reduction stage and the brake removed from the rig, as shown in Figure 6.1. Since there was no load, the only operating parameter left to define was the motor speed.

The acquisition chain is the one described in Section 4.2. Two triaxial accelerometers were mounted on the gearbox housing, one on the input side and one on the output side, giving the six channels referred to throughout this Chapter as `IN_pos1_x`, `IN_pos1_y`, `IN_pos1_z` and the corresponding `OUT_pos1_*` channels. The tachometer was acquired as a seventh channel on the same time base, and all channels were sampled at $f_s = 4$ kHz.

A set of preliminary runs was performed with the motor commanded at speeds between 1500 and the nominal 4000 rpm, with one record acquired at each speed. Two criteria were used to judge the operating point: the agreement between the measured shaft speed and the expected value, and the legibility of the tachometer pulse train. The comparison between the theoretical shaft speeds and the measured results is presented in Table 6.1.

Table 6.1: Verification of the measured shaft speed against the theoretical value, for the speeds tested in the preliminary runs.

Commanded motor speed [rpm]	Theoretical shaft speed [rpm]	Measured shaft speed [rpm]	Relative error [%]
1500	250	251	+0.4
2000	333	334	+0.3
3000	500	502	+0.4
4000	666	714	+7.2

Between 1500 and 3000 rpm the measured speed follows the expected value to within 0.4 %, with no apparent dependence on the speed itself. At 4000 rpm the error rises to +7.2 %, which means that the edge detector registered more transitions than the pulley made revolutions. For that reason the 4000 rpm motor speed was excluded.

The time synchronous average, and with it every signal derived from it, rests entirely on the tachometer as the angular reference of the input shaft, so the pulse train itself was inspected before the monitoring records were accepted. A segment acquired at 3000 rpm is shown in Figure 6.2. The transitions are sharp and although the tachometer did not retrieve exactly rectangular pulses, they are relatively equidistant. Tests were performed with a variety of thresholds for edge detection having detected no significant differences between them, and a threshold of 2 V was adopted.

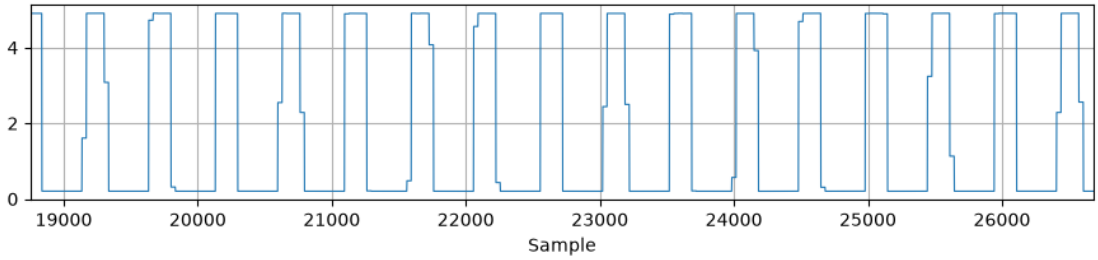


Figure 6.2: Segment of the tachometer signal (Voltage) at 3000 rpm.

As a further check, the number of samples counted in each revolution was extracted for a representative record, the number of samples registered through transition detection of the tachometer signal will be compared with the expected theoretical value for a shaft rotating at 500 rpm. Over the record examined, 271 revolutions were detected with a mean length of 479.74 samples, against the 480 expected at 500 rpm, and a standard deviation of 16.52 samples, or 3.44 % of the mean. As shown in Figure 6.3 the counts fall at two distinct levels, at around 480 ± 16.52 samples, which is coherent with the slight speed fluctuation characteristic of BLDC motors rather than with an acquisition defect, although the latter cannot be excluded.

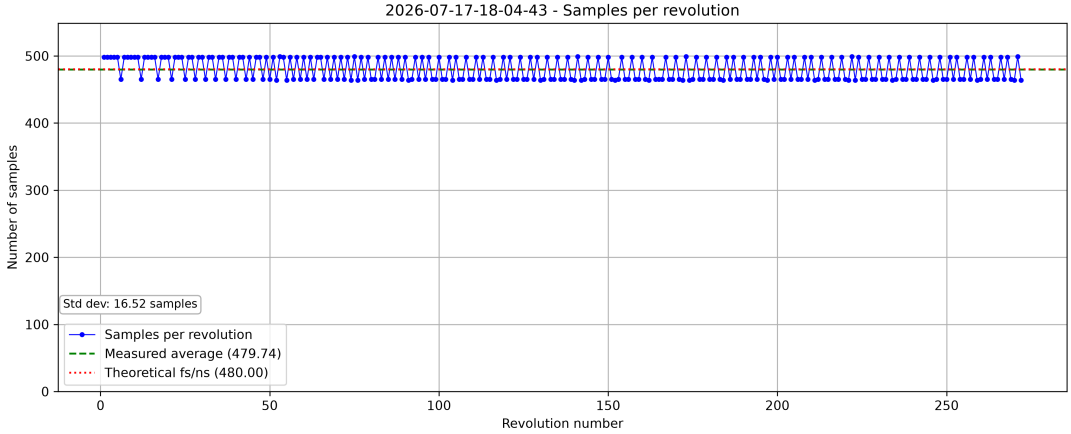


Figure 6.3: Number of samples per revolution in the preliminary tests.

The previous Chapter reported that the records taken on the first iteration of the rig produced smeared spectra in which the meshing harmonics could not be distinguished. In the spectrum of the record acquired at 3000 rpm, Figure 6.4, some smearing is still present and is heavier on some channels than on others, as the comparison between the x and y directions shows. On `IN_pos1_y`, however, the meshing frequency appears as an identifiable peak at 266.7 Hz, concentrated in a few bins rather than spread over a wide band, and its harmonics remain individually identifiable up to the sixth order, so the gear meshing information does come through the background noise.

Taking both criteria together, a commanded motor speed of 3000 rpm was adopted for the remainder of the campaign. Among the speeds at which the tachometer counted correctly it is the highest, which places the meshing frequency and its harmonics as high as possible within the measured band while still leaving seven mesh harmonics below the Nyquist frequency, and it stays clear of the regime in which the pulse train ceased to be reliable. Of the three directions, the y channels return the clearest meshing content. This is expected: the meshing force acts primarily in the lateral direction, which is also the direction recommended for gearbox measurements in ISO 20816-9 [41]. The resulting operating conditions are collected in Table 6.2 and apply to every record presented in this Chapter.

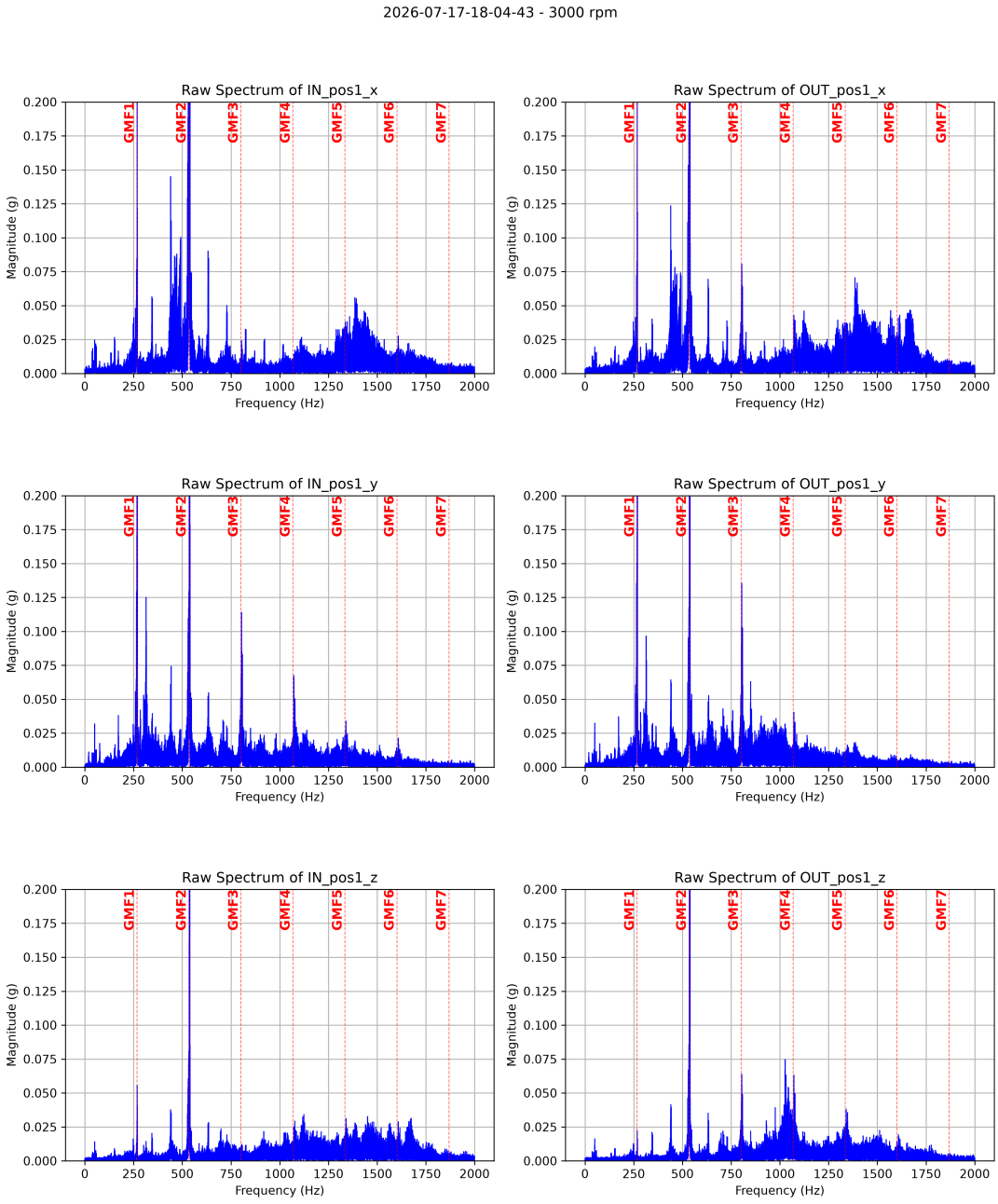


Figure 6.4: Amplitude spectrum of the raw signal acquired at 3000 rpm, with the shaft rotational frequency and the meshing harmonics indicated.

Table 6.2: Operating conditions adopted for the monitoring campaign.

Parameter	Value
Commanded motor speed, n_{motor}	3000 rpm
Stage 1 reduction, i	6
Gear shaft speed, $n_{II} = n_{III}$	500 rpm (8.33 Hz)
Number of teeth, z	32
Gear ratio	1:1
Meshing frequency, GMF	266.7 Hz
Sampling rate, f_s	4000 Hz
Nyquist frequency	2000 Hz
Mesh harmonics below Nyquist	7
Applied load	none
Lubrication	none
Measurement direction	Y

6.2 Campaign Overview and Outcome

The campaign was carried out over three test days, 20, 21 and 22 July 2026, preceded by a single record acquired on 17 July with the gear pair in the as-received condition. Within each day the rig was run in a morning and an afternoon session, and on the last day the afternoon session was extended into the evening. The schedule is summarised in Table 6.3.

Table 6.3: Schedule of the experimental campaign.

Date	Session	Running time [hh:mm]
17 July	Preliminary	$\sim$ 00:02
20 July	Afternoon	01:26
21 July	Morning	03:34
21 July	Afternoon	00:53
22 July	Morning	04:04
22 July	Afternoon	00:45
22 July	Evening (failure)	00:30
Total		11:14

Two outcomes should be stated from the start, since they determine how the results that follow are to be read. The first is that the wear produced on the gear pair was very light. The black oxide coating was progressively removed from the working flanks, in a band whose position revealed a misalignment between the gear axes, and a change of profile developed near the tooth tip; beyond these two features no loss of material was registered. The experimental campaign produced no response in any of the CIs, for two main reasons. The first is that the meshing vibration does not stand out against the background of this rig, the shaft-synchronous component amounts to only about 5 % of the recorded signal in RMS (see Figure 6.11), so the indicators computed after the time synchronous average have little to work with. The second is that the campaign was interrupted

rather than concluded, by the failure of the coupling connecting the motor to shaft I. Gear wear had no opportunity to develop further, and the failure itself was only partly characterised, since the coupling sits upstream of the gearbox and the transmission path to the accelerometers is likely to dissipate much of its vibration signature; a sensor placed closer to it would probably have registered a more gradual and clearer change in the indicators.

The lack of development in gear wear is a consequence of the conditions under which the demonstrator had to be run rather than of the duration of the campaign. At the nominal 500 rpm of the gear shafts, the total running time of Table 6.3 corresponds to approximately 3.37×10^5 revolutions of the gear pair. Feng et al. [34] destroyed a dry spur gear pair after only 18 000 revolutions under 10 N m, and Hu et al. [19] reached the transition to rapid wear after about 2.6×10^6 revolutions under splash lubrication and 14.7 N m. What separates this campaign from both is not its duration but the load the demonstrator was unable to apply, as established in the previous Chapter. A measurable amount of surface wear was consequently not to be expected, and the results below are to be read as a characterisation of the measurement chain and of the behaviour of the rig rather than as a wear progression.

6.3 Condition of the Gear Pair

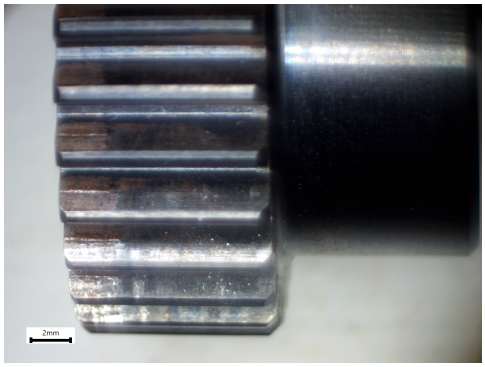
The gear pair was removed from the demonstrator and photographed at the end of each test day, on the working flanks and along the tooth profile. Figure 6.5 compares the working flanks and the tooth profiles at the first and last inspections.

The progressive removal of the black oxide coating from the working flanks was observed over the campaign, exposing the base metal underneath. The removal is not uniform across the face width: it begins at one end of the face and advances towards the other as the campaign progresses, so that the exposed region remains a band along one side of the tooth rather than a patch centred on the face.

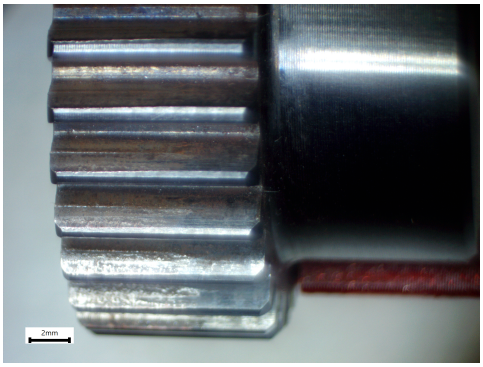
A contact band confined to one end of the face indicates that the two gear axes are not parallel, so that contact is carried on one side of the tooth rather than distributed across it. Given that the bearing housings are 3D printed and mounted on an aluminium profile frame, a misalignment of this order is consistent with the positioning tolerances available in the assembly. The observation is therefore a statement about the demonstrator, not the gears.

Beyond the coating, a slight change of the tooth profile is noticeable near the tip. It is most evident in the images of the flank surface, where a gradient in tooth tip thickness can be identified in the images taken at the end of the tests, shown with more detail in Figure 6.6. This is a consequence of the reduced centre distance adopted for the gearbox, which moves the contact towards the tip of the tooth and makes it harsher there than a nominal pair would experience.

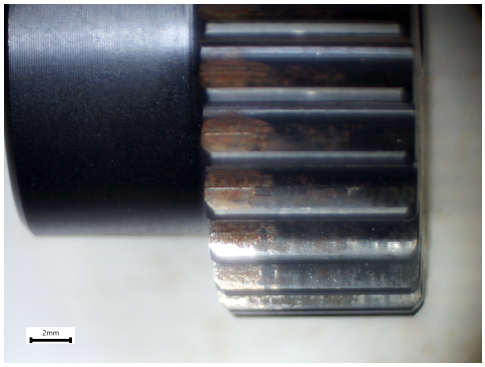
Apart from these two features, no change of the tooth profile was detected and no loss of material could be resolved.



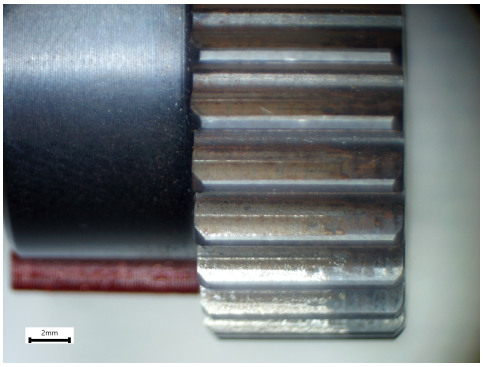
(a) Input gear flank, first inspection.



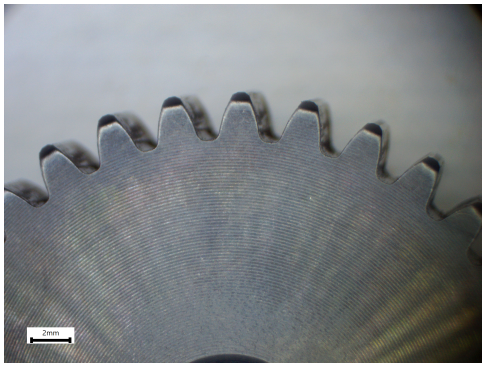
(b) Input gear flank, last inspection.



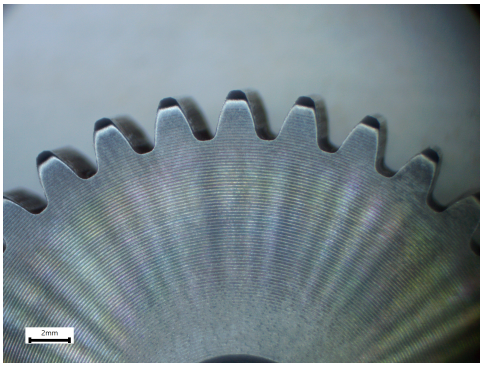
(c) Output gear flank, first inspection.



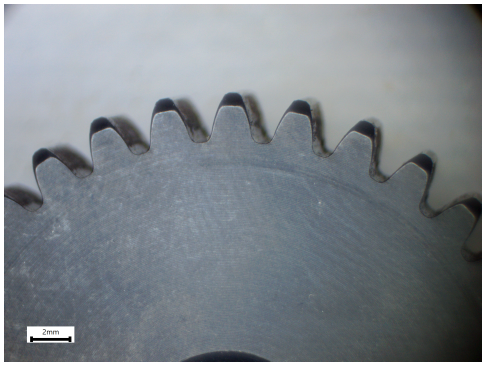
(d) Output gear flank, last inspection.



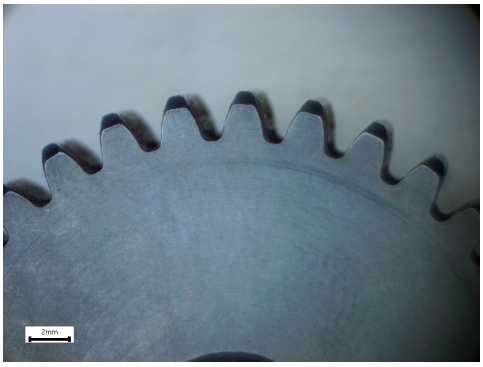
(e) Input gear profile, first inspection.



(f) Input gear profile, last inspection.

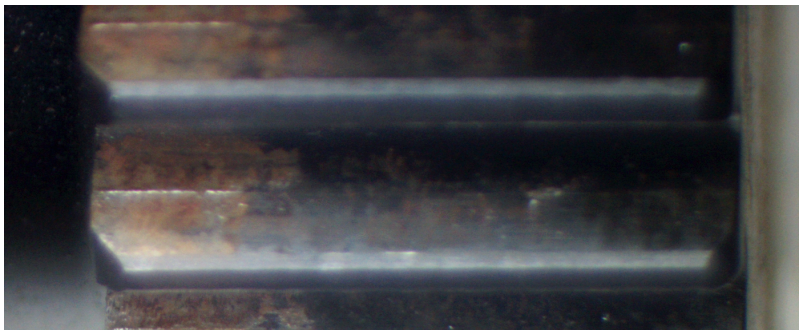


(g) Output gear profile, first inspection.

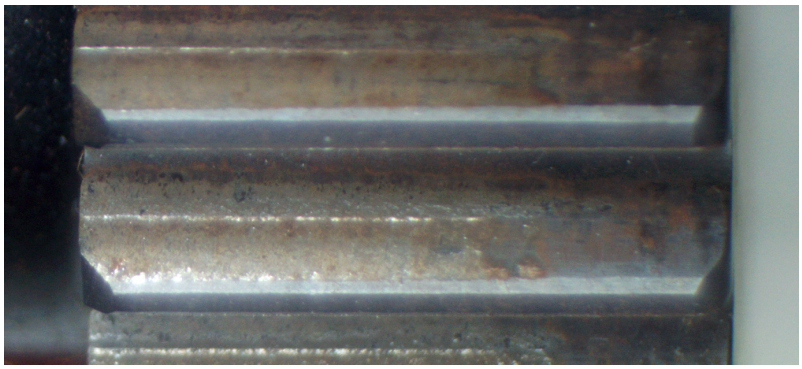


(h) Output gear profile, last inspection.

Figure 6.5: Condition of the gear pair at the first and last inspections of the campaign.



(a) Start of the campaign.



(b) End of the campaign.

Figure 6.6: Tooth tips of the output gear at the start and at the end of the campaign.

6.4 Events Observed During the Campaign

Two main anomalous events were detected during the otherwise uniform running of the rig. Both are described here in physical terms; how the CIs responded to them is treated in Section 6.5.

6.4.1 Noise emission and impulsive events

The demonstrator was audibly loud throughout the campaign, louder than would be expected of a regular 200 W drive. Two features of the design account for this. The gear pair runs dry, so there is no lubricant film to separate the flanks or to damp the meshing impacts, leaving direct metal-to-metal contact and a correspondingly higher friction at the mesh. In addition, the centre distance was deliberately set below the theoretical 32 mm, by bringing the two shafts closer together than the nominal value, so that the teeth would remain in mesh regardless of the positioning tolerances and possible deflection of the printed supports; the reduction lowers the backlash and holds the flanks in tighter contact than a nominal pair would experience, raising the friction at the mesh and with it the noise emitted.

Against this background, during the first test session the gearbox also produced an audible click at irregular intervals. The clicks were not periodic, with no constant interval identifiable and no fixed relation to the shaft revolution, and each of them coincided with an isolated spike in the raw acceleration signal, visible in Figure 6.7. The peaks did not appear consistently on the same

channel: some appeared only on the x channels, some only on y or z, and some on several axes at once, with no pattern relating the affected axis to the sensor position.

The most plausible explanation is debris passing through the mesh. Running-in of the as-received surfaces is ruled out by the timing: asperities are highest before any running, yet the preliminary record of 17 July shows the lowest maximum peak acceleration of the campaign. Debris, by contrast, has to be generated first, which accounts for the delay of the events. Inspection at the end of testing showed black oxide coating particles dispersed inside the gearbox and the accelerometers, with the reduced centre distance leaving almost no backlash, the teeth cannot separate to let a fragment through and it is crushed in a single sharp event. The clicking would then stop once the loosely adherent coating had been shed, consistent with its absence over the remainder of the campaign. No debris was collected during the tests, but an image taken at the end of the campaign, Figure 6.8, confirms the presence of coating debris inside the gearbox and even reaching the sensors.

6.4.2 Failure of the motor coupling

The campaign ended during the evening session of the last test day with the failure of the coupling connecting the motor to shaft I, shown in Figure 6.9. The rig was unattended at the time, so the failure was not observed directly; it was identified on the following inspection.

A fracture was found in the connection between the metal bellows of the coupling body and the hub to which shaft I was attached. The shape of the fracture, Figure 6.9a, suggests lateral bending rather than torsion as its cause, which suggests that the forces induced by the belt tension on shaft I deflected the 3D-printed supports beyond the radial misalignment the coupling was rated to tolerate, cracking it by fatigue. The remaining components of the drive train were inspected afterwards. The only other significant damage recorded was to the bearings supporting shaft I: a manual check showed that this shaft lost rotational energy noticeably faster than the others, indicating that the same misalignment had also affected the bearings.

The vibration records were re-examined after the failure, and pronounced peaks in acceleration were found in the records acquired during the afternoon preceding it, Figure 6.10. A plausible reading is that the crack formed at this point without fully detaching the hub from the rest of the coupling, allowing power transmission to continue for the remaining sessions. The feature of this record that matters for the present work is the difference between the input-side and the output-side channels: the peaks in acceleration are essentially absent from the latter, which is consistent with a malfunction occurring upstream of the gearbox. This behaviour is examined quantitatively in Section 6.5.1.

6.5 CIs over the Campaign

The indicators are trended over the 29 records of the campaign. Each record contains seven minutes of continuous acquisition, and consecutive records within a session are separated by approximately 30 minutes of running time, so each point summarises seven minutes of vibration and the

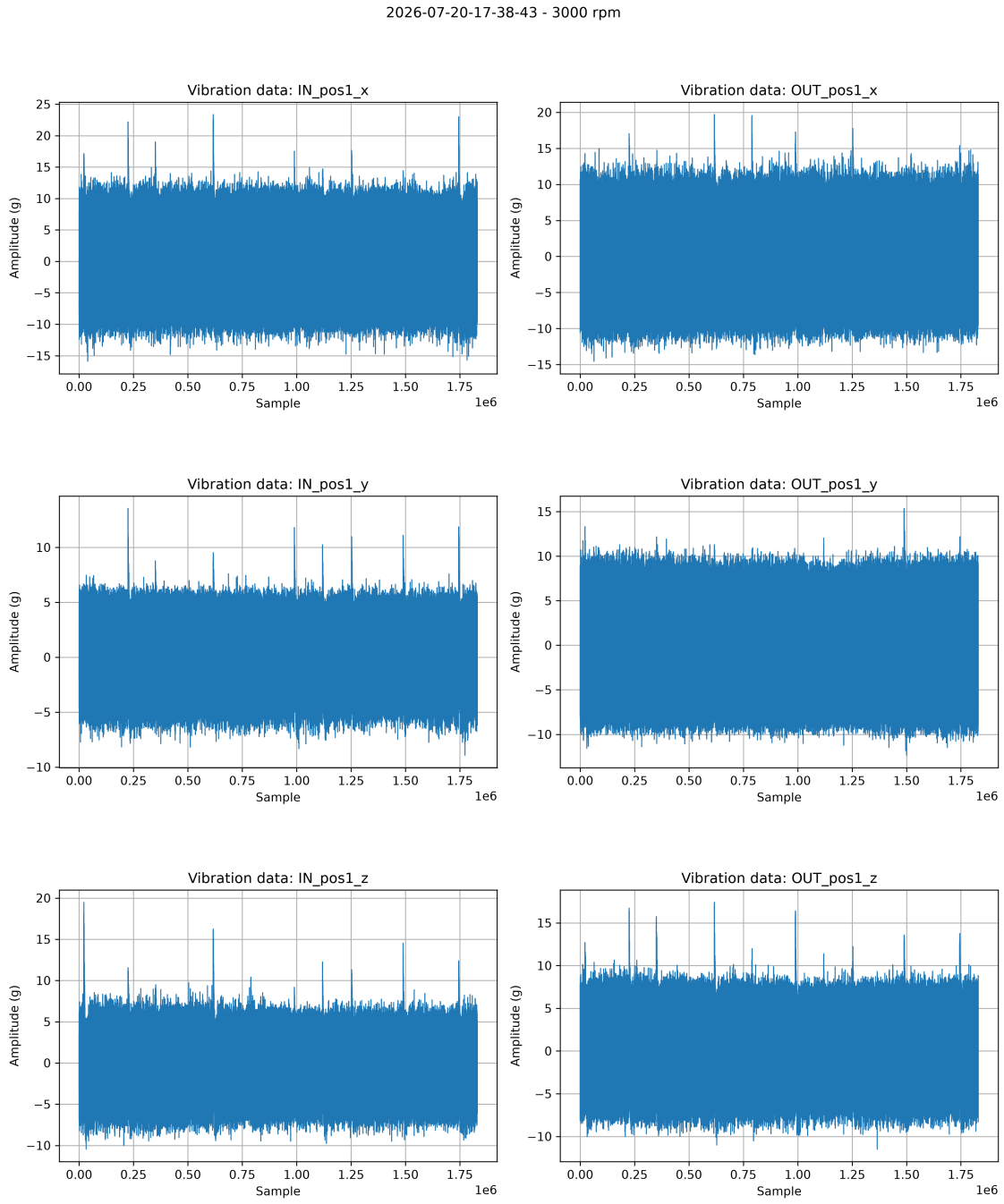
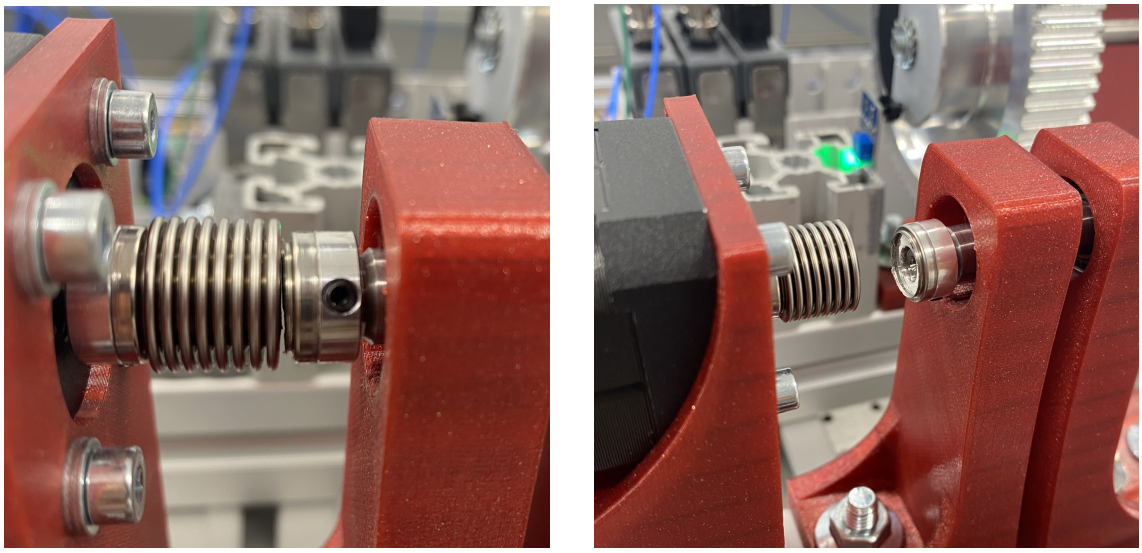


Figure 6.7: Raw acceleration signal of a record acquired during the first test session, showing the isolated spikes coincident with the audible clicking.



Figure 6.8: Coating particles in the test rig at the end of testing.



(a) (b)

Figure 6.9: Coupling between the motor and shaft I after the failure.

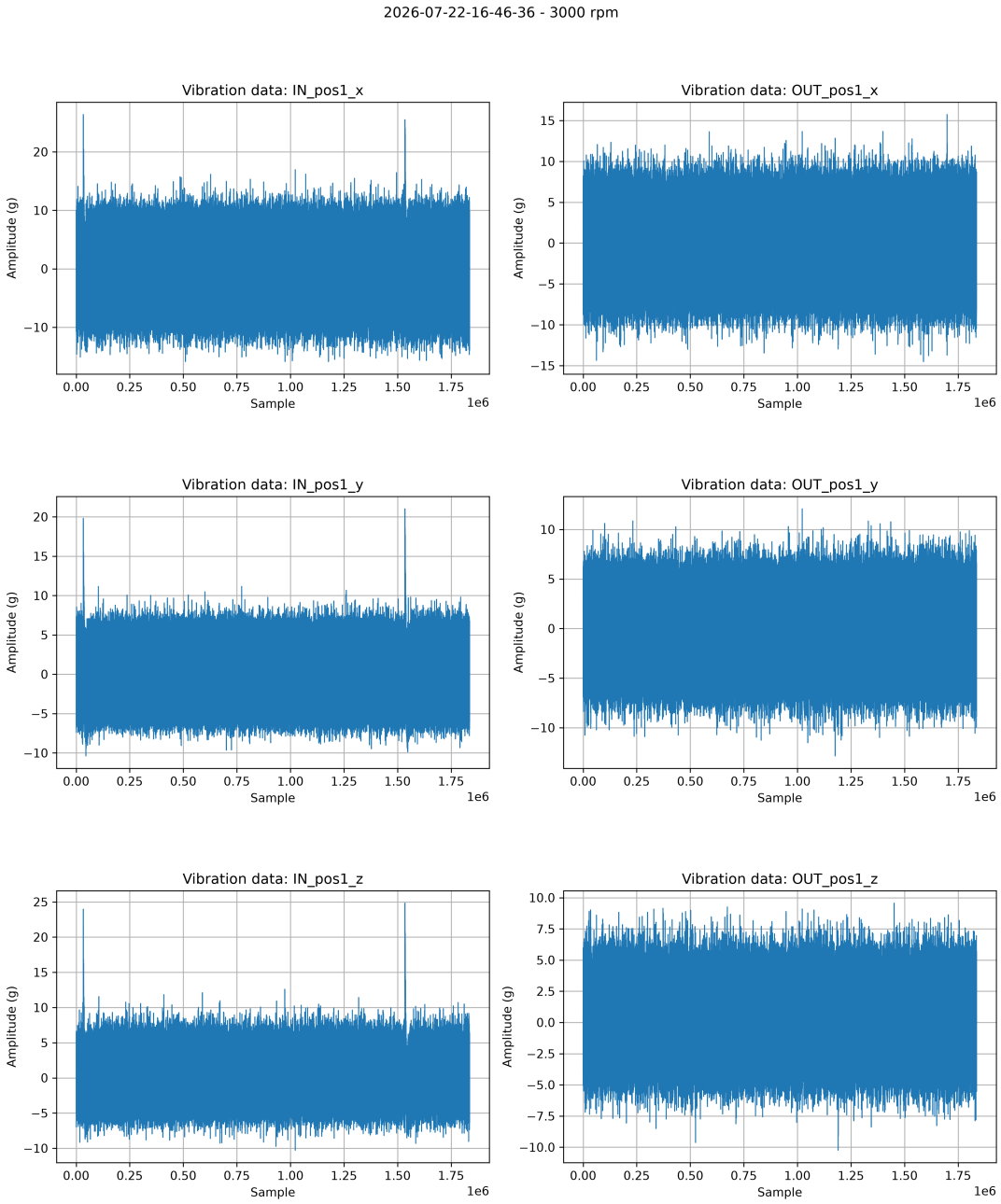


Figure 6.10: Raw vibration data from the record preceding the coupling failure.

interval between points represents half an hour of operation that was not recorded. Only steady-state operation is included: records containing the acceleration of the rig from rest, its deceleration, or any stoppage were excluded, so every point represents the rig running at the operating point of Table 6.2.

For the reasons given in Section 6.1 only the y channels are presented, with the input-side sensor on the left of each figure and the output-side sensor on the right.

6.5.1 Indicators computed on the raw signal

The raw RMS shown in Figure 6.11 shows no progressive trend. On `IN_pos1_y` it sits around 2.1 g through the first session, rises to about 3.1 g at the start of the second test day and decays back to 2.1 g by the end of the campaign, the only outlier being a sudden rise upon restart in the middle of the second day, with `OUT_pos1_y` following roughly the same shape. The more significant variation aligns with session boundaries rather than with running time, which raises a question over the repeatability of the test conditions across runs.

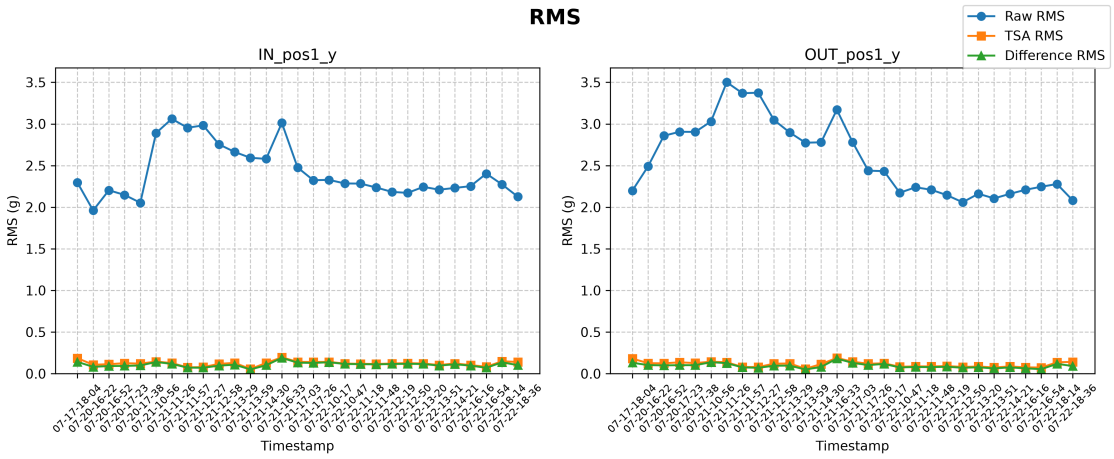


Figure 6.11: RMS of the raw, TSA and difference signals over the whole campaign.

The same figure also fixes the scale of the synchronous content. The RMS of the TSA signal and of the corresponding difference signal never exceeds about 0.22 g, against a raw RMS between 2.0 and 3.5 g, so the shaft-synchronous component amounts to the order of 5 % of the signal in RMS. Every indicator computed downstream of the average therefore operates on a small residue of a much larger asynchronous background, to which the unloaded, unlubricated mesh and the belt drives both contribute.

The maximum peak acceleration and the raw kurtosis behave differently. Neither trends, but both respond sharply to the two events of Section 6.4. On `IN_pos1_y` the maximum peak sits on a baseline of 10 to 12 g and departs from it during the records containing the clicking, reaching 18.2 g, and at the record preceding the coupling failure, reaching 24.2 g; the raw kurtosis follows the same pattern, rising from a baseline near 2.6 to 4.4 and to 4.6 respectively. The kurtosis of the TSA and difference signals is plotted on the same axes and stays inside a band of roughly 2.2 to

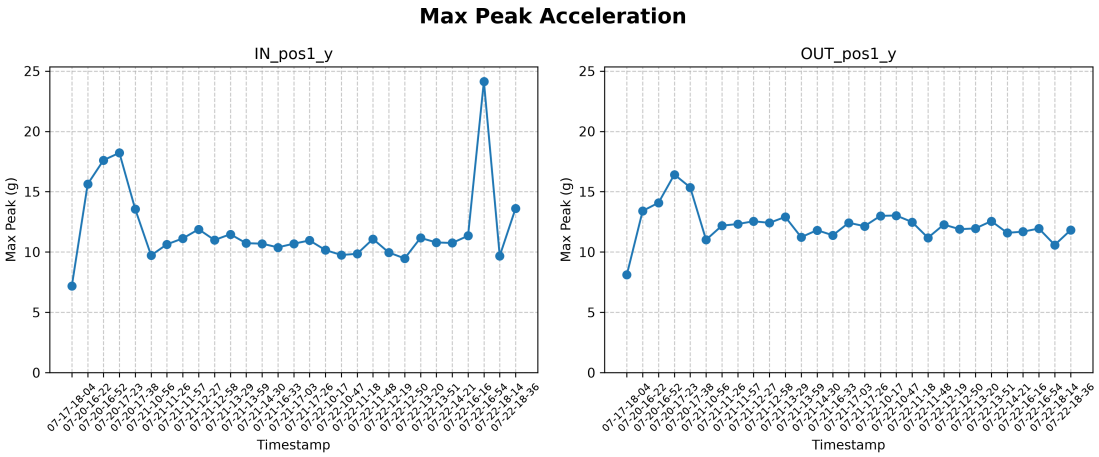


Figure 6.12: Maximum peak acceleration of the raw signal over the whole campaign.

3.3 for all 29 records, showing none of these excursions. Since the average retains only what is synchronous with the input shaft, its indifference to both events places their sources outside the shaft-synchronous domain.

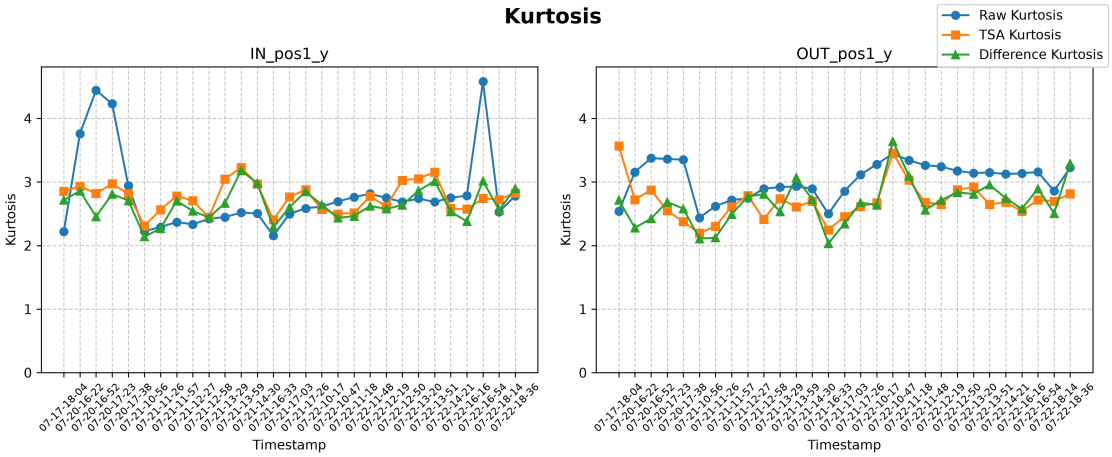


Figure 6.13: Kurtosis of the raw, TSA and difference signals over the whole campaign.

Where the two events differ is in which sensor recorded them. During the records containing the clicking both sensors respond: the maximum peak reaches 18.2 g on the input side against a baseline of 10 to 12 g, and 16.4 g on the output side against a baseline near 12 g, so the event is registered on either side of the housing. At the record preceding the coupling failure the input side reaches 24.2 g, the largest value of the campaign, while the output side records only 11.6 g, a value similar to its immediate neighbours; the raw kurtosis behaves the same way.

The two accelerometers are mounted on opposite sides of the gearbox housing, so a source has a different path to each. Vibration originating at the mesh, or from a body circulating inside the housing, reaches both sensors through comparable structural paths and appears on both. Vibration originating upstream of the gear pair reaches the input-side sensor through the input shaft support

alone, but must additionally cross the mesh and the width of the housing to reach the output side, and is attenuated in doing so. The clicking events are therefore consistent with a source at or inside the mesh, and the event preceding the failure with a source upstream of the gearbox. Viewed on the input channel alone the two events are of the same kind, both isolated transients of comparable magnitude, and nothing in the trace separates a fragment passing through the mesh from a crack opening in the drive line; it is only the comparison between the two sensors that distinguishes them, and that comparison is what localises the degraded component.

6.5.2 Indicators computed on the TSA signal

FM4 fluctuates between about 2.1 and 3.7 on both channels with no drift and no response to either event. The values sit consistently below the nominal value of 3 that a Gaussian difference signal would return, which indicates residual deterministic content in $d(n)$. The difference signal retains the mesh orders above the sixth and all sidebands beyond the first, so FM4 is describing the composition of $d(n)$ as constructed rather than strictly the condition of the gear pair.

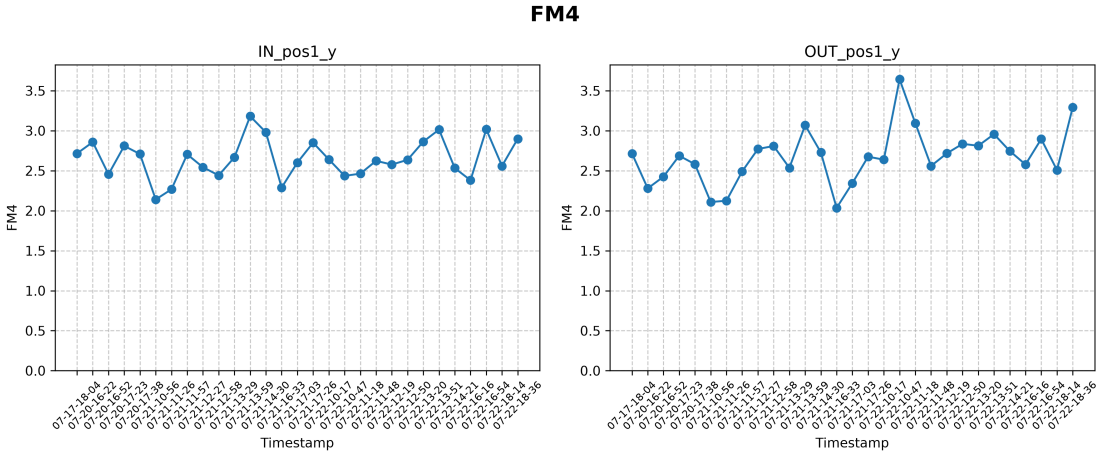


Figure 6.14: FM4 over the whole campaign.

The ER showed no apparent trend until the last day of acquisition in which it showed a sustained variation: over the last records of the campaign it declined steadily on both sensors (see Figure 6.15, reaching the lowest values registered. Because the ER is the ratio of the RMS of the difference signal by that of the regular meshing signal, a decline can be produced by a fall in the numerator or by a rise in the denominator, and these correspond to different physical changes. The final test day was therefore re-analysed at a finer resolution, processing every vibration record, and the two terms were plotted separately alongside the ratio.

The decomposition in Figures 6.16a and 6.16b shows that the two halves of the decline have different causes. Through the morning and early afternoon the RMS of the regular meshing signal holds near 0.035 g on both sensors while the RMS of the difference signal decays slowly, from about 0.12 to 0.09 g on `IN_pos1_y`, so the ratio falls because its numerator falls. In the final records the behaviour reverses. The difference signal reaches the largest value of the day, about

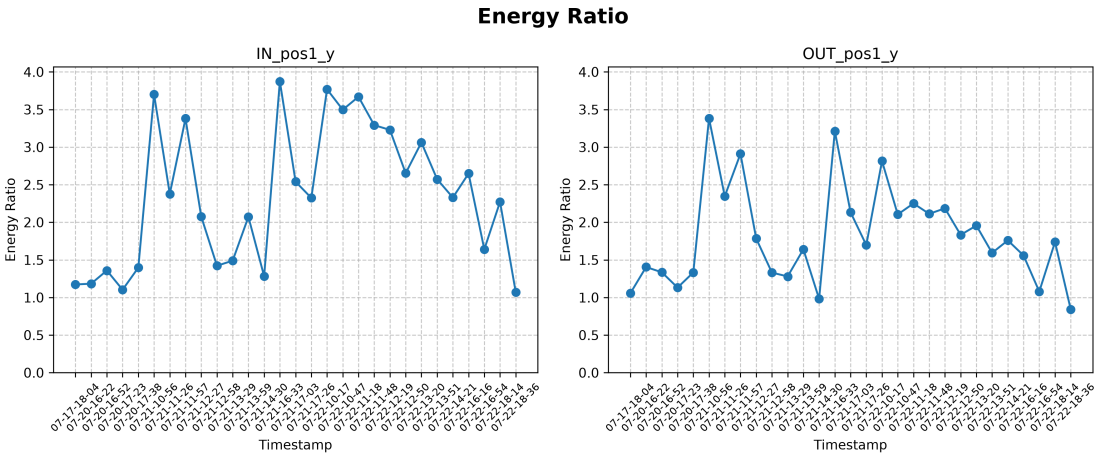


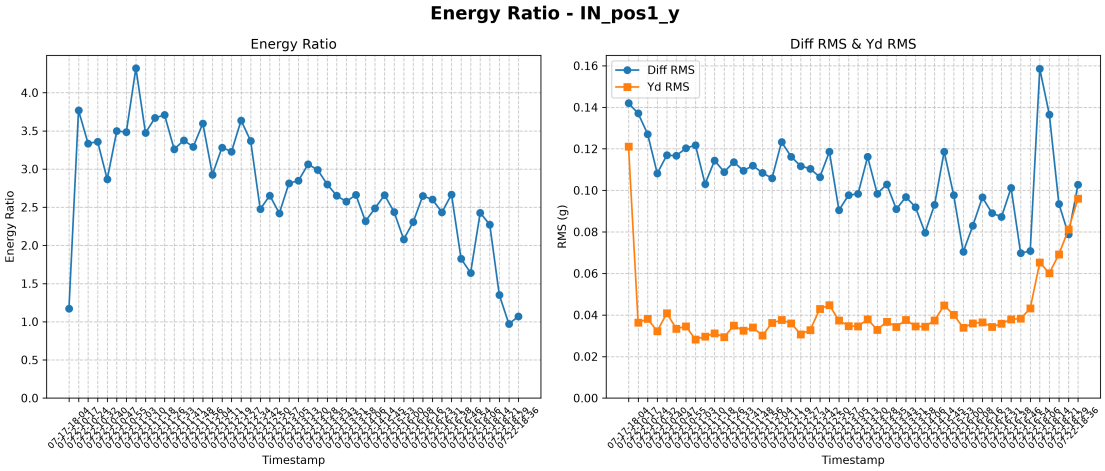
Figure 6.15: ER across the whole campaign.

0.16 g on `IN_pos1_y`, in the record containing the transient described in Section 6.4.2, and from that record onwards the RMS of the regular meshing signal rises monotonically, from about 0.043 to 0.096 g on `IN_pos1_y` and from about 0.047 to 0.108 g on `OUT_pos1_y`, roughly tripling in both cases. The collapse of the ratio below unity is therefore driven by growth in its denominator: the deterministic, shaft-synchronous content of the vibration increased sharply on both sides of the gearbox over the last hour before the coupling failed.

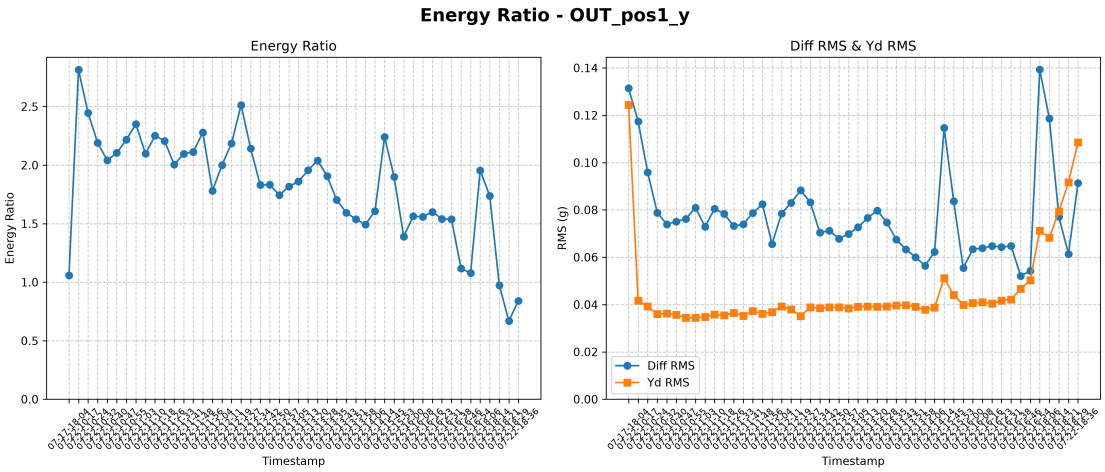
Two features of this rise argue against reading it as scatter. It is monotonic over the last six records, against a baseline that had held constant over the preceding thirty-five records of the same day, and it appears on both accelerometers with the same shape. It also begins at the record in which the transient was recorded, which is consistent with the interpretation offered in Section 6.4.2, that the crack formed at that point without immediately interrupting transmission.

The kinematics identify where the additional deterministic content may have originated. The 6:1 stage 1 reduction places the frequency of the motor shaft at order 6 of the instrumented shaft, and $y_{reg}(n)$ is reconstructed from shaft orders 1 to 6. A once-per-revolution disturbance developing on shaft I, which is where the coupling sits, is therefore synchronous with the tachometer, survives the averaging and enters $y_{reg}(n)$ directly. A coupling progressively losing concentricity due to its cracked bellows imposes exactly such a disturbance, transmitted to the gearbox as a fluctuating radial force through the stage 1 belt, whose tension fluctuates as the crack alternately aligns with and opposes it, and this is consistent with the rise appearing on both accelerometers at once rather than on the input side alone.

If that fluctuating force also modulated the mesh, the resulting sidebands would be of the 6^{th} order. These lie outside the band retained in $y_{reg}(n)$, which keeps only the first sideband of each mesh order, and would be routed into $d(n)$ instead. The difference signal does rise over the same records, which is consistent with both routes being active. One limitation should be attached to this reading: $y_{reg}(n)$ aggregates twelve orders without identifying which of them grew, so the attribution to order 6 remains an inference from the kinematics rather than an observation.



(a) `IN_pos1_y`.



(b) `OUT_pos1_y`.

Figure 6.16: ER over the final test day, with the RMS of the difference signal $d(n)$ and of the regular meshing signal $y_{reg}(n)$ from which it is computed.

6.5.3 Frequency-domain indicators

Neither of the frequency-domain indicators produced a usable trend. The bandpassed envelope kurtosis, Figure 6.17), stays below about 130 for most of the campaign and rises only at the records already identified by the raw indicators, adding nothing that Section 6.5.1 does not already establish. It shows, however, a greater sensitivity to those events, reaching 2260 on `IN_pos1_y` at the record preceding the coupling failure. This is expected, since the indicator is computed on the envelope of a signal band-passed to the frequency range where impulsiveness is most evident, so the transient is measured against a much reduced background rather than against the whole signal.

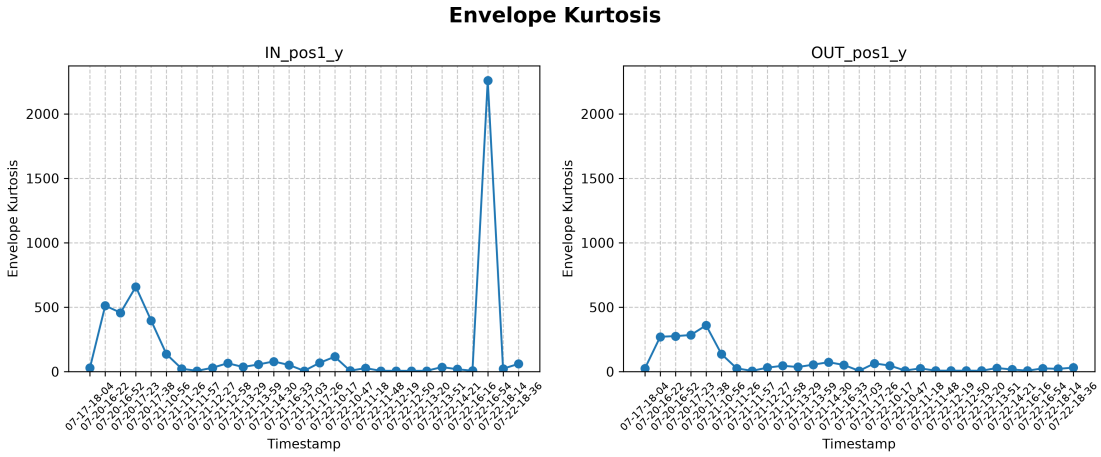


Figure 6.17: Kurtosis of the envelope obtained at the selected demodulation band, over the whole campaign.

The band is obtained from a kurtogram, as described in Section 2.4.3, which evaluates SK as a function of frequency and of the STFT window length. Both are re-selected for every record to maximise the kurtosis, so successive values are not estimates of a common quantity, which limits the meaning of the indicator, as it was used, for wear evaluation. A further consequence follows from how the width of the band is set. In the implementation used here the bandwidth is taken as f_s/N_w, the spacing of the STFT bins, so a parameter that governs how the spectrum is resolved also determines how the signal is filtered. The record of 22 July at 16:54 selected $N_w = 8192$ on `OUT_pos1_y`, giving a pass band of 0.49 Hz, and a band this narrow cannot contain sidebands at the shaft rotational frequency of 8.33 Hz. The envelope extracted from it therefore cannot represent modulation at any frequency of interest in the gearbox, so what the indicator detected was the transient itself rather than any periodic content.

The ALR, Figure 6.18, drifts upward on both channels, most clearly on `OUT_pos1_y`, from about 0.44 in the earliest records to about 2.07 in the last, with substantial scatter superimposed. The ALR measures the distance of the gear state vector from a fixed reference, so the drift indicates that the state vector moved away from the condition recorded in the initial test, though it does not identify the direction of that movement. This is the only indicator showing a rising trend, but the

scatter between consecutive records is of the same order as the total drift across the campaign, which limits what can be read into it.

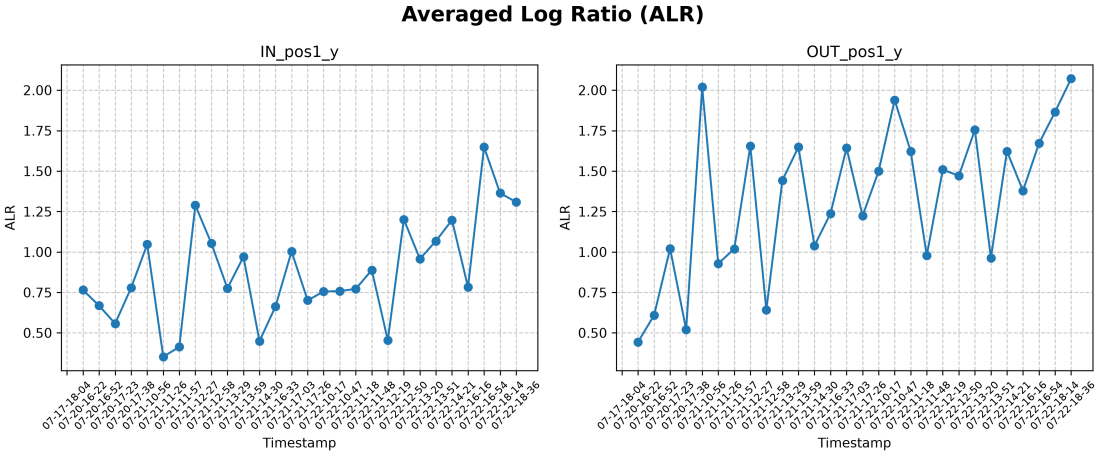


Figure 6.18: ALR against the first record of the campaign.

Chapter 7

Conclusions and Future Work

This work set out to construct a Digital Twin of a gear transmission: a numerical model kept in correspondence with the physical system through vibration measurements, capable of inferring the wear state of the gear pair and its remaining useful life. Designing and building a demonstrator in which wear can be induced in a controlled way and detected reliably from vibration proved to be the substantial part of that problem, and it absorbed the time available. The demonstrator was designed, built, instrumented and operated, and the full acquisition and processing chain was implemented and exercised on experimental data, but the rig could not be operated under load, and the degradation history it was built to observe was therefore not produced. Once that limitation was established, there was no margin left within the work to diagnose the drive chain and run a second campaign. The objective was not reached: without a wear progression there is nothing against which an indicator can be validated; without a validated indicator there is no measured wear state to update a model from; and without that exchange there is no DT.

That outcome shapes the conclusions that follow. The objectives set out in Section 1.2 were met to different degrees: the review of the state of the art and the design and construction of the rig were completed, the acquisition chain was implemented and validated, and the CIs were implemented and compared, but the comparison could not be made against a wear progression, and the wear quantification that was to follow from it was therefore not reached. What the campaign established concerns the demonstrator itself, the behaviour of the indicators in the absence of the fault they were chosen for, and the distance that remains between the rig as built and a working DT. Each is treated in turn below, followed by the prospects of future works.

7.1 The Demonstrator

The inability to apply load was the decisive limitation of the work. The motor stalled repeatedly at a small fraction of its rated current while the same drive train, brake included, could be turned by hand, which points to a limitation in the control chain rather than to the mechanical resistance of the assembly. Since wear is driven by contact pressure and sliding, the revolutions accumulated over the campaign produced no surface degradation that a vibration indicator could be expected

to follow, and no indicator reported here can be considered validated against gear wear. The comparison with published dry and lubricated gear tests in Section 6.2 shows that the campaign was not short: it ran considerably longer than a dry test in which a comparable gear pair was destroyed. The difference lies entirely in the load.

The rig also showed that the compliance of the additively manufactured parts governs its design, and it showed this twice. In the first iteration the centre distance was defined by two independent supports whose deflection allowed the teeth to skip; imposing that distance through a single printed housing removed the failure mode completely. The same compliance later ended the campaign, when the static pull of the stage 1 belt deflected the supports of shaft I beyond the misalignment the coupling was rated to tolerate, and the coupling failed by fatigue. Two design rules follow. Any dimension critical to the kinematics must be carried by a single component rather than established across an assembly of compliant parts. And the static loads imposed by the transmission elements, belt tension in particular, must be treated as design loads for the printed structure, not as incidental.

The measurement chain, by contrast, works, which was not a foregone conclusion given the printed transmission path between the mesh and the sensors. The meshing frequency appears as a discrete peak with harmonics identifiable up to the sixth order, and the shaft speed obtained from the optical tachometer agrees with the kinematic value to within a few tenths of a percent over the usable speed range, so the rig supports order tracking and time synchronous averaging. The redesign of the housing is what made this possible, since the first iteration produced spectra in which the meshing harmonics did not stand clear above the rest.

7.2 Wear Evaluation

No indicator trended over the campaign, which is the expected outcome in the absence of load and of the wear it would have produced. The campaign nonetheless produced two unintended events, the passage of coating debris through the mesh and the failure of the coupling, and the response of the indicators to them is informative in a way that a null result alone would not be.

Both events were registered by the maximum peak acceleration and by the kurtosis of the raw signal, while every indicator computed after the time synchronous average stayed within its normal band. This is the correct behaviour rather than a failure: neither source was synchronous with the instrumented shaft, and the average is designed to suppress exactly that content. The processing chain therefore discriminated between shaft-synchronous and asynchronous sources as intended, and did so on real data.

Comparing the two accelerometers separated the two events further. The debris passing through the mesh appeared on both sensors, whereas the event upstream of the gearbox appeared almost exclusively on the input side. Viewed on a single channel the two transients are indistinguishable; it is the comparison between sensor positions that identifies which part of the machine is degrading. Sensor placement is therefore not only a practical matter but a source of diagnostic information in its own right, and this is the most transferable result of the campaign.

Four observations about the indicators themselves should be carried forward, since they concern the methods rather than this particular rig.

The first is that under no load the gear mesh is not the dominant source in the measurement. The shaft-synchronous component amounted to only about a twentieth of the recorded signal in RMS, so every indicator computed after the average operated on a small residue of a much larger asynchronous background. Applying a load is therefore not only a requirement for producing wear, but also for making the mesh loud enough relative to the belt drives and bearings for a change at the mesh to be detectable at all.

The second is a mismatch between method and failure mode. Envelope analysis and the kurtogram are formulated to detect localised, repetitive impacts, which is why they are usually applied to bearing defects and to cracked or spalled teeth, the fault signature being recovered as modulation of a structural resonance at the repetition rate of the impacts. Distributed surface wear is neither localised nor impulsive, and acts instead by changing the transmission error and the sideband structure around the meshing harmonics. The null result returned by the envelope indicators is therefore a mismatch of the method to the intended failure mode rather than a failure of the method.

The third concerns the kurtogram as implemented. Because the demodulation band and the analysis window are re-selected for every record to maximise the kurtosis, successive values are not estimates of a common quantity, and the indicator is properly used as a detector of transients rather than as a measure of their severity. A further difficulty arises from tying the width of the demodulation band to the resolution of the analysis, as discussed in Section 6.5.3, since a long window then produces a pass band too narrow to contain the modulation being sought. Separating the two would remove the problem.

The fourth concerns the reference values the indicators assume. FM4 is normalised so that an undamaged gear returns three, but this presupposes a difference signal containing no deterministic content. Since the FM4 returned values often below that threshold, it is probable that, by construction, significant deterministic content was left in the difference signal either by excluding harmonics from the 7^{th} order up, or from taking only the first order side bands from each harmonic when constructing $y_{reg}(n)$. The ALR requires a comparable caution, being a distance from a fixed reference record, so that a drift away from that reference does not by itself identify what changed or in which direction.

7.3 Distance to a DT

Measured against the levels of integration described by Iliuţă et al. [3]: digital model, digital shadow, digital twin and predictive digital twin, the demonstrator delivers the acquisition of data from the physical system and part of its analysis, but not the return path from model to machine. A physical system runs under known and repeatable operating conditions, its vibration and angular position are acquired synchronously, and a processing pipeline converts those records into a set of CIs without manual intervention. That pipeline has been exercised on real data and shown to

behave correctly, including in the discrimination between synchronous and asynchronous sources described above.

What is absent is everything that follows from a validated indicator. There is no quantification of wear beyond visual inspection of the flanks, no model updated from the measurements, and consequently no estimate of RUL. The two-way exchange between model and machine that defines a DT is therefore not established, and the gap is dominated by a single item. Without the ability to impose a load, no wear progression exists to be quantified, no indicator can be validated against one, and no model can be updated from it.

7.4 Future Work

The work that follows is dictated by the limitations reported above, and it has a natural order: the rig must first be made able to load the gear pair, then made stiff enough to survive doing so for long periods, a more complete instrumentation should also be employed, and only afterwards used to produce the data on which a DT could be built.

The first priority is the drive and load unit. The spring-applied friction brake should be replaced altogether, a holding brake dissipates energy in a disc not designed for continuous slip and it offers no practical variable way of setting an arbitrary load. A braking unit intended for continuous and adjustable load should be specified instead, with the eddy current brake studied in Section 3.3 as the most immediate candidate. In parallel, the drive chain has to be characterised until the stall reported is explained and removed, by measuring the current actually delivered to the motor and confirming whether the limit lies in the driver configuration, in the power supply or in the control algorithm. Until a known torque can be imposed and held for hours at a time, none of the remaining items can be addressed.

The second priority is the redesign of the structural components in metal. The gearbox housing and the supports of the pulley shafts should be machined rather than printed, so that the concentricity of the bearings and the parallelism of the gear axes are set by manufacturing tolerances instead of by the stiffness of a polymer part. Two features should be incorporated in that redesign. The gearbox may be given an adjustable centre distance, which would allow gear pairs of different modules and tooth counts to be tested on the same rig. The mechanism would need a stiff clamping arrangement, since the bearing housings would become adjustable parts liable to shift under vibration, and the joint would sit directly in the path along which the signal travels from the mesh to the sensors. The pulley supports should include a belt tensioning mechanism, so that the tension is set to the value required by the transmitted torque rather than to whatever results from the assembly, relieving the radial load that deflected the support, resulting in the coupling failure.

The third item is the extension of the instrumentation. Accelerometers should be added at the remaining bearing positions and on the motor side, since the comparison between the two sensors used in this campaign was already sufficient to place a source upstream or downstream of the mesh, and a denser set of measurement points would extend that reasoning to individual components. The single-pulse tachometer should be replaced by incremental encoders on both gear shafts, which

would provide a reliable angular reference at any speed, including those at which the optical sensor failed, and would make the transmission error directly measurable. Transmission error is the quantity most closely related to the geometry of the tooth flanks, and its inclusion would give an independent reference against which the vibration-based indicators could be judged.

Once the rig is able to run loaded, a new experimental campaign should be carried out to the point of measurable wear, with periodic inspection and quantification of the flank surfaces, and repeated so that the dispersion between nominally identical runs is known. This last point matters for the interpretation of the present results, in which the variation between sessions was of the same order as the variation attributable to anything else. The resulting indicator trends should then be benchmarked against published results obtained on comparable gear pairs, which is what would establish the demonstrator as a valid source of wear data rather than only as a working rig. Only then does it become useful to close the remaining layers of the DT architecture, that is, to convert the indicators into a wear quantification, to update a wear model from them and to estimate the remaining useful life of the pair.

References

[1] L. Ismail, A. Abdelmoti, A. Basu, A. D. E. Berini, and M. Naouss, "A Systematic Review of Digital Twin-Driven Predictive Maintenance in Industrial Engineering: Taxonomy, Architectural Elements, and Future Research Directions," *ArXiv.org*, Sep. 2025. DOI: 10.48550/arxiv.2509.24443. [Online]. Available: http://arxiv.org/abs/2509.24443.

[2] M. Molęda, B. Małysiak-Mrozek, W. Ding, V. Sunderam, and D. Mrozek, "From corrective to predictive maintenance: A review of maintenance approaches for the power industry," *Sensors*, vol. 23, no. 13, p. 5970, 2023. DOI: 10.3390/s23135970.

[3] M.-E. Iliuţă, M.-A. Moisescu, E. Pop, A.-D. Ionita, S.-I. Caramihai, and T.-C. Mitulescu, "Digital Twin—A Review of the Evolution From Concept to Technology and Its Analytical Perspectives on Applications in Various Fields," *Applied Sciences*, vol. 14, no. 13, p. 5454, Jun. 2024. DOI: 10.3390/app14135454. [Online]. Available: https://doi.org/10.3390/app14135454.

[4] D. Zhong, Z. Xia, Y. Zhu, and J. Duan, "Overview of Predictive Maintenance Based on Digital Twin Technology," *Heliyon*, vol. 9, no. 4, e14534, Mar. 2023. DOI: 10.1016/j.heliyon.2023.e14534. [Online]. Available: https://doi.org/10.1016/j.heliyon.2023.e14534.

[5] R. Van Dinter, B. Tekinerdogan, and C. Catal, "Predictive Maintenance Using Digital Twins: A Systematic Literature Review," *Information and Software Technology*, vol. 151, p. 107 008, Jul. 2022. DOI: 10.1016/j.infsof.2022.107008. [Online]. Available: https://doi.org/10.1016/j.infsof.2022.107008.

[6] T. Zonta, C. A. da Costa, R. da Rosa Righi, M. J. de Lima, E. S. da Trindade, and G. P. Li, "Predictive maintenance in the Industry 4.0: A systematic literature review," *Computers & Industrial Engineering*, vol. 150, p. 106 889, 2020. DOI: 10.1016/j.cie.2020.106889.

[7] N. H. A. Wahab et al., "Systematic Review of Predictive Maintenance and Digital Twin Technologies Challenges, Opportunities, and Best Practices," *PeerJ Computer Science*, vol. 10, e1943, Apr. 2024. DOI: 10.7717/peerj-cs.1943. [Online]. Available: https://doi.org/10.7717/peerj-cs.1943.

[8] P. Phutane, S. Chavan, H. Pawar, S. Mane, and V. Barde, "Digital Twin Innovations for Induction Motor Monitoring and Predictive Maintenance: A 2020–2025 Review," *Next research.*, vol. 2, no. 4, p. 100 969, Oct. 2025. DOI: 10.1016/j.nexres.2025.100969. [Online]. Available: https://doi.org/10.1016/j.nexres.2025.100969.

[9] K. Feng, H. Xiao, J. Zhang, and Q. Ni, "A digital twin methodology for vibration-based monitoring and prediction of gear wear," *Wear*, vol. 571, p. 205 806, 2025. DOI: 10.1016/j.wear.2025.205806. [Online]. Available: https://doi.org/10.1016/j.wear.2025.205806.

[10] E. Rabinowicz, *Friction and Wear of Materials*. John Wiley I& Sons, Jan. 1965.

[11] I. Hutchings and P. Shipway, *Tribology*. Butterworth-Heinemann, Apr. 2017.

[12] J. T. Burwell, "Survey of Possible Wear Mechanisms," *Wear*, vol. 1, no. 2, pp. 119–141, Oct. 1957. DOI: 10.1016/0043-1648(57)90005-4. [Online]. Available: https://doi.org/10.1016/0043-1648(57)90005-4.

[13] A. P. Daga, A. Fasana, S. Marchesiello, and L. Garibaldi, "The Politecnico Di Torino Rolling Bearing Test Rig: Description and Analysis of Open Access Data," *Mechanical Systems and Signal Processing*, vol. 120, pp. 252–273, Oct. 2018. DOI: 10.1016/j.ymssp.2018.10.010. [Online]. Available: https://doi.org/10.1016/j.ymssp.2018.10.010.

[14] S. Tiwari, S. K. Kamarapu, A. M, M. K. Gupta, and G. Vashishtha, "Tool wear monitoring based on vibration signal analysis using FFT and EMD," *Proceedings of the World Congress on Mechanical, Chemical, and Material Engineering*, Aug. 2024. DOI: 10.11159/icmie24.137. [Online]. Available: https://doi.org/10.11159/icmie24.137.

[15] P. Liu, S. Yang, and Y. Liu, "Full-scale Test and Numerical Simulation of Wheelset-gear Box Vibration Excited by Wheel Polygon Wear and Track Irregularity," *Mechanical Systems and Signal Processing*, vol. 167, p. 108 515, Oct. 2021. DOI: 10.1016/j.ymssp.2021.108515. [Online]. Available: https://doi.org/10.1016/j.ymssp.2021.108515.

[16] T. Najeh, J. Lundberg, and A. Kerrouche, "Deep-Learning and Vibration-Based System for Wear Size Estimation of Railway Switches and Crossings," *Sensors*, vol. 21, no. 15, p. 5217, Jul. 2021. DOI: 10.3390/s21155217. [Online]. Available: https://doi.org/10.3390/s21155217.

[17] M. Zhang, K. Wang, D. Wei, and M. J. Zuo, "Amplitudes of Characteristic Frequencies for Fault Diagnosis of Planetary Gearbox," *Journal of Sound and Vibration*, vol. 432, pp. 119–132, Jun. 2018. DOI: 10.1016/j.jsv.2018.06.011. [Online]. Available: https://doi.org/10.1016/j.jsv.2018.06.011.

[18] Q. Miao and Q. Zhou, "Planetary Gearbox Vibration Signal Characteristics Analysis and Fault Diagnosis," *Shock and Vibration*, vol. 2015, pp. 1–8, Jan. 2015. DOI: 10.1155/2015/126489. [Online]. Available: https://doi.org/10.1155/2015/126489.

[19] C. Hu, W. A. Smith, R. B. Randall, and Z. Peng, "Development of a Gear Vibration Indicator and Its Application in Gear Wear Monitoring," *Mechanical Systems and Signal Processing*, vol. 76-77, pp. 319–336, Feb. 2016. DOI: 10.1016/j.ymssp.2016.01.018. [Online]. Available: https://doi.org/10.1016/j.ymssp.2016.01.018.

[20] Z. Y. Chin, P. Borghesani, W. A. Smith, R. B. Randall, and Z. Peng, "Monitoring Gear Wear With Transmission Error," *Wear*, vol. 523, p. 204 803, Mar. 2023. DOI: 10.1016/j.wear.2023.204803. [Online]. Available: https://doi.org/10.1016/j.wear.2023.204803.

[21] International Organization for Standardization, "Gears — wear and damage to gear teeth — part 1: Nomenclature and characteristics," ISO, Geneva, Switzerland, International Standard ISO 10825-1:2022(E), 2022. [Online]. Available: https://www.iso.org/standard/78719.html.

[22] S. Maraş, H. Arslan, and B. Birgören, "Detection of Gear Wear and Faults in Spur Gear Systems Using Statistical Parameters and Univariate Statistical Process Control Charts," *Arabian Journal for Science and Engineering*, vol. 46, no. 12, pp. 12 221–12 234, Jul. 2021. DOI: 10.1007/s13369-021-05930-y. [Online]. Available: https://doi.org/10.1007/s13369-021-05930-y.

[23] E. Bergseth, *Influence of Surface Topography and Lubricant Design in Gear Contacts*, Jan. 2009. [Online]. Available: http://urn.kb.se/resolve?urn=urn:nbn:se:kth:diva-11180.

[24] B. Errichello and J. Muller, *How to Analyze Gear Failures*, Jun. 2019. [Online]. Available: https://www.machinerylubrication.com/Read/150/gear-failures.

[25] R. Errichello, "Gear Contact Temperature and Scuffing Risk Analysis," *Encyclopedia of Tribology*, pp. 1469–1470, Jan. 2013. DOI: 10.1007/978-0-387-92897-5\{_}568. [Online]. Available: https://doi.org/10.1007/978-0-387-92897-5_568.

[26] J. C. A. J. Correa and A. A. L. Guzman, *Mechanical Vibrations and Condition Monitoring*. Academic Press, Mar. 2020.

[27] W. D. Mark, H. Lee, R. Patrick, and J. D. Coker, "A Simple Frequency-domain Algorithm for Early Detection of Damaged Gear Teeth," *Mechanical Systems and Signal Processing*, vol. 24, no. 8, pp. 2807–2823, Apr. 2010. DOI: 10.1016/j.ymssp.2010.04.004. [Online]. Available: https://doi.org/10.1016/j.ymssp.2010.04.004.

[28] J. K. Sinha, *Industrial Approaches in Vibration-based Condition Monitoring*. CRC Press, Jan. 2020.

[29] P. D. McFadden, "Detecting Fatigue Cracks in Gears by Amplitude and Phase Demodulation of the Meshing Vibration," *Journal of vibration and acoustics*, vol. 108, no. 2, pp. 165–170, Apr. 1986. DOI: 10.1115/1.3269317. [Online]. Available: https://doi.org/10.1115/1.3269317.

[30] K. Feng, J. Ji, Q. Ni, Y. Li, W. Mao, and L. Liu, "A Novel Vibration-based Prognostic Scheme for Gear Health Management in Surface Wear Progression of the Intelligent Manufacturing System," *Wear*, vol. 522, p. 204 697, Mar. 2023. DOI: 10.1016/j.wear.2023.204697. [Online]. Available: https://doi.org/10.1016/j.wear.2023.204697.

[31] R. B. Randall, *Vibration-based Condition Monitoring: Industrial, Aerospace and Automotive Applications*. John Wiley I& Sons, Feb. 2011. [Online]. Available: http://catalogimages.wiley.com/images/db/jimages/9780470747858.jpg.

[32] V. Sharma and A. Parey, "A Review of Gear Fault Diagnosis Using Various Condition Indicators," *Procedia Engineering*, vol. 144, pp. 253–263, Jan. 2016. DOI: 10.1016/j.proeng.2016.05.131. [Online]. Available: https://doi.org/10.1016/j.proeng.2016.05.131.

[33] J. Ren and H. Yuan, "A Dynamic Wear Prediction Model for Studying the Interactions Between Surface Wear and Dynamic Response of Spur Gears," *Coatings*, vol. 12, no. 9, p. 1250, Aug. 2022. DOI: 10.3390/coatings12091250. [Online]. Available: https://doi.org/10.3390/coatings12091250.

[34] K. Feng et al., "Vibration-based Updating of Wear Prediction for Spur Gears," *Wear*, vol. 426-427, pp. 1410–1415, Apr. 2019. DOI: 10.1016/j.wear.2019.01.017. [Online]. Available: https://doi.org/10.1016/j.wear.2019.01.017.

[35] X. Kong, J. Tang, Z. Hu, H. Ding, Z. Wang, and Q. Wang, "Dynamic modeling and vibration analysis of spur gear system considering thin-walled gear and hollow shaft," *Mechanism and Machine Theory*, vol. 181, p. 105 197, 2023. DOI: 10.1016/j.mechmachtheory.2022.105197. [Online]. Available: https://doi.org/10.1016/j.mechmachtheory.2022.105197.

[36] J. F. Archard, "Contact and Rubbing of Flat Surfaces," *Journal of Applied Physics*, vol. 24, no. 8, pp. 981–988, Aug. 1953. DOI: 10.1063/1.1721448. [Online]. Available: https://doi.org/10.1063/1.1721448.

[37] S. Wu, M. J. Zuo, and A. Parey, "Simulation of Spur Gear Dynamics and Estimation of Fault Growth," *Journal of Sound and Vibration*, vol. 317, no. 3-5, pp. 608–624, May 2008. DOI: 10.1016/j.jsv.2008.03.038. [Online]. Available: https://doi.org/10.1016/j.jsv.2008.03.038.

[38] O. D. Mohammed, M. Rantatalo, and J.-O. Aidanpää, "Dynamic Modelling of a One-stage Spur Gear System and Vibration-based Tooth Crack Detection Analysis," *Mechanical Systems and Signal Processing*, vol. 54-55, pp. 293–305, Sep. 2014. DOI: 10.1016/j.ymssp.2014.09.001. [Online]. Available: https://doi.org/10.1016/j.ymssp.2014.09.001.

[39] O. D. Mohammed and M. Rantatalo, "Dynamic Response and Time-frequency Analysis for Gear Tooth Crack Detection," *Mechanical Systems and Signal Processing*, vol. 66-67, pp. 612–624, Jun. 2015. DOI: 10.1016/j.ymssp.2015.05.015. [Online]. Available: https://doi.org/10.1016/j.ymssp.2015.05.015.

[40] P. D. Samuel and D. J. Pines, "A Review of Vibration-based Techniques for Helicopter Transmission Diagnostics," *Journal of Sound and Vibration*, vol. 282, no. 1-2, pp. 475–508, Oct. 2004. DOI: 10.1016/j.jsv.2004.02.058. [Online]. Available: https://doi.org/10.1016/j.jsv.2004.02.058.

[41] "Mechanical vibration — Measurement and evaluation of machine vibrationPart 9: Gear units," International Organization for Standardization, Geneva, CH, Standard, Jun. 2020. [Online]. Available: https://www.iso.org/standard/75670.html.

[42] J. Antoni, "The spectral kurtosis: a useful tool for characterising non-stationary signals," *Mechanical Systems and Signal Processing*, vol. 20, no. 2, pp. 282–307, 2006. DOI: 10.1016/j.ymssp.2004.09.001. [Online]. Available: https://doi.org/10.1016/j.ymssp.2004.09.001.

[43] M. A. Pimentel, D. A. Clifton, L. Clifton, and L. Tarassenko, "A Review of Novelty Detection," *Signal Processing*, vol. 99, pp. 215–249, Jan. 2014. DOI: 10.1016/j.sigpro.2013.12.026. [Online]. Available: https://doi.org/10.1016/j.sigpro.2013.12.026.

[44] T. Pan, T. Wang, J. Chen, J. Xie, and S. Cao, "A Global and Joint Knowledge Distillation Method With Gradient-modulated Dynamic Parameter Adaption for EMU Bogie Bearing Fault Diagnosis," *Measurement*, vol. 235, p. 114 927, May 2024. DOI: 10.1016/j.measurement.2024.114927. [Online]. Available: https://doi.org/10.1016/j.measurement.2024.114927.

[45] A. Esposito, *Fluid Power With Applications*. Prentice Hall, Jan. 2009.

[46] "Technical pdf for hydraulic gear pump group 1," Flowfit, Tech. Rep., 2026. [Online]. Available: https://www.flowfitonline.com/uploads/PDFproducts/flowfitgroup1gearpump.pdf.

[47] C. Loedolff, *Development of a Test Setup to Determine the Frictional Losses on Bicycle Drivetrains*.

[48] B. Rebbechi, F. B. Oswald, and D. P. Townsend, "Dynamic measurements of gear tooth friction and load," *Defense Technical Information Center (DTIC)*, Jan. 1991. [Online]. Available: http://oai.dtic.mil/oai/oai?&verb=getRecord&metadataPrefix=html&identifier=ADA240126.

[49] M. Gulec, M. Aydin, and P. Sergeant, "Eddy Current Brakes: A Review on Working Principles and Technology Evolution," *2022 International Conference on Electrical Machines (ICEM)*, pp. 441–447, Sep. 2022. DOI: 10.1109/icem51905.2022.9910747. [Online]. Available: https://doi.org/10.1109/icem51905.2022.9910747.

[50] W. contributors, *Eddy Current Brake*, May 2026. [Online]. Available: https://en.wikipedia.org/wiki/Eddy_current_brake.

[51] D. Schieber, "Braking Torque on Rotating Sheet in Stationary Magnetic Field," *Proceedings of the Institution of Electrical Engineers*, vol. 121, no. 2, p. 117, Jan. 1974. DOI: 10.1049/piee.1974.0021. [Online]. Available: https://doi.org/10.1049/piee.1974.0021.

[52] D. Meeker, *Finite element method magnetics, version 4.2: User's manual*, 4.2, Accessed: 2026-09-11, Oct. 2015. [Online]. Available: https://www.femm.info/wiki/Documentation/.

[53] P. H. Black and O. E. Adams, *Machine Design*. McGraw-Hill Companies, Jan. 1968.

[54] *SS steel spur gears — module 1*, Stock gears catalogue, pp. 111–113, KHK Kohara Gear Industry Co., Ltd., Kawaguchi, Japan, 2024. Accessed: Sep. 11, 2026. [Online]. Available: https://khkgears.net/pdf/ss.pdf.

[55] *Spur gear — pressure angle 20°, module 0.8, shaft bore configurable type (GEAB series)*, FA mechanical standard components catalogue, pp. 1-1501–1-1502, MISUMI Europa GmbH, 2014. Accessed: Sep. 11, 2026. [Online]. Available: https://uk.misumi-ec.com/pdf/fa/2014/P1_1501-1502_F20_EN_001.pdf.

[56] *Injection-moulded plastic spur gears, module 1.25, pressure angle 20°*, Datasheet, part no. 21480, norelem Normelemente GmbH & Co. KG, Markgröningen, Germany. Accessed: Sep. 11, 2026. [Online]. Available: https://www.norelem.com/.

[57] *Injection-moulded plastic spur gears, module 1.5, pressure angle 20°*, Datasheet, part no. 21481, norelem Normelemente GmbH & Co. KG, Markgröningen, Germany. Accessed: Sep. 11, 2026. [Online]. Available: https://www.norelem.com/.

[58] K. J. Nisbett and R. G. Budynas, *Screws, Fasteners, and the Design of Nonpermanent Joints*, 10th ed. McGraw-Hill Education, Jan. 2014.

[59] E. Oberg, F. D. Jones, H. Ryffel, and H. Horton, *Machinery's Handbook 31 Digital Edition*. Industrial Press, Mar. 2020.

[60] Gates Corporation, "Belt pull, static belt pull, shaft load, and bearing load," Gates Corporation, PA Note 17656-6, Jun. 2009, Volume 56, No. 6. Accessed 5 August 2026. [Online]. Available: https://www.gatesaustralia.com.au/~/media/files/gates/industrial/power-transmission/flyers-and-brochures/vol-56-no-6-static-belt-pull.pdf.

[61] C. R. Soderberg, "Factor of Safety and Working Stress," *Transactions of the American Society of Mechanical Engineers*, vol. 52, no. 2, pp. 13–21, Jan. 1930. DOI: 10.1115/1.4057307. [Online]. Available: https://doi.org/10.1115/1.4057307.

[62] S. Dunkerley, "On The Whirling and Vibration of Shafts," *Proceedings of the Royal Society of London*, vol. 54, no. 326-330, pp. 365–370, Dec. 1894. DOI: 10.1098/rspl.1893.0085. [Online]. Available: https://doi.org/10.1098/rspl.1893.0085.

[63] M. Ö. Öteyaka, F. H. Çakir, and M. A. Sofuoğlu, "Effect of Infill Pattern and Ratio on the Flexural and Vibration Damping Characteristics of FDM Printed PLA Specimens," *Materials Today Communications*, vol. 33, p. 104 912, Nov. 2022. DOI: 10.1016/j.mtcomm.2022.104912. [Online]. Available: https://doi.org/10.1016/j.mtcomm.2022.104912.

[64] E. Hozdić and E. Hozdić, "Influence of Infill Structure Shape and Density on theMechanical Properties of FDM 3D-Printed PETG andPETG+CF Materials," *Advanced Technologies Materials*, vol. 49, no. 2, pp. 15–27, Oct. 2024. DOI: 10.24867/atm-2024-2-002. [Online]. Available: https://doi.org/10.24867/atm-2024-2-002.

[65] R. Pianowski, R. Kamenzky, S. Wolter, Z. Song, and P. Blaschke, "Parameter Investigation of Sensor Fixation Methods Compared With High-Quality Laser Measurement Using a Scalable Automatic Modal Hammer," *Conference proceedings of the Society for Experimental Mechanics*, pp. 57–63, Sep. 2023. DOI: 10.1007/978-3-031-37007-6\{_}7. [Online]. Available: https://doi.org/10.1007/978-3-031-37007-6_7.

[66] S. Shokrollahi, F. Adel, and H. Ahmadian, "An Investigation Into the Accelerometer Mounting Effects on Signal Transmissibility in Modal Measurements," *Scientia Iranica*, vol. 0, no. 0, p. 0, Aug. 2017. DOI: 10.24200/sci.2017.4244. [Online]. Available: https://doi.org/10.24200/sci.2017.4244.

[67] M. Dumont, A. Cook, and N. Kinsley, "Acceleration Measurement Optimization: Mounting Considerations and Sensor Mass Effect," *Conference proceedings of the Society for Experimental Mechanics*, pp. 61–71, Jan. 2016. DOI: 10.1007/978-3-319-30249-2\{_}4. [Online]. Available: https://doi.org/10.1007/978-3-319-30249-2_4.